New experimental approaches to dimuon production in heavy ion collisions

Luca Casagrande

Advisor: Prof. Peter Sonderegger

Thesis prepared at:

CERN, in the framework of the NA50 and RD39 Collaborations and
Instituto Superior Técnico of Universidade Técnica de Lisboa

submitted for the degree of Doctor in Physics

December 1999

to Alfredo.
to Aurelio, Lello, Maria e Nina.

Loosely or tightly, everything fits,
even the wrists on your arm.
Grow and decay, it's only forever.

Chris Cornell

Abstract

We demonstrate that the physics scope of dimuon spectrometers can be significantly enhanced by adding a pixel vertex spectrometer. Results obtained with a test set-up show that, using a track matching procedure, we are able to identify and precisely measure the muons, which triggered the dimuon spectrometer, among all secondaries in the vertex region, even for central Pb-Pb collisions. It becomes possible to study low-mass dimuon production with good mass resolution, and to measure the production rate of charmed mesons, by selecting muon tracks with a certain offset relative to the interaction point.

The existing pixel detectors would not survive the radiation doses expected for the study of the rare dimuon events. We have therefore investigated how to improve the radiation tolerance of both pixel sensor and readout electronics. I was involved in the discovery of the *Lazarus effect*; namely the experimental observation that irradiated silicon detectors, no longer functional at room temperature, resuscitate when operated around 130 K.

We also present results on irradiation tests performed on prototype pixel chips. The radiation tolerance of a chip manufactured in 0.25 μm CMOS technology was measured to be 1000 times higher than the previous generation chip.

Key words:

Quark-Gluon Plasma; Heavy ion collisions; Dimuon production; Silicon pixel detectors; Radiation damage; Lazarus effect.

Resumo

Neste trabalho mostramos que é possível melhorar significativamente espectrómetros de dimuões adicionando-lhes um espectrómetro de vertice realisado com detectores de pixeis de silício. Os resultados obtidos com um detector de teste mostram claramente que a identificação e medição das propriedades dos muões na zona do alvo melhora significativamente a precisão das medidas. Para além da melhoria da qualidade das medidas de dimuões de baixa massa, este novo detector poderá medir a taxa de produção de mesões D, seleccionando os traços de muões com uma distância mínima em relação ao ponto de interacção.

Os detectores de pixeis existentes não possuíam a tolerância à radiação que nós precisávamos para estudar processos raros. Daí que tenhamos estado activamente envolvidos nos esforços de melhoria da tolerância às radiações dos detectores de pixel, quer no que respeita ao sensor quer no que diz respeito à electrónica de leitura.

Estive pessoalmente envolvido na primeira observação do efeito de Lazarus, i.e. detectores fortemente irradiados podem ressuscitar quando operados a temperaturas próximas de 130 K.

Também apresentamos resultados de testes de irradiação realisados em protótipos de chips de leitura. Em particular, mostramos que um chip realisado usando tecnologia 0.25 μm CMOS pode sobreviver após uma irradiação 1000 vezes superior às versões anteriores.

Palavras chave:

Quark-Gluon Plasma; Colisões de iões pesados; Produção de dimuões; Detectores de silício; Degradação por radiação; Efeito de Lazarus.

Acknowledgements

It is a great pleasure for me to thank the many people who contributed, in a way or the other, to the preparation of this work.

I am extremely grateful to Peter Sonderegger, who despite being my advisor, is also one of my best friends. He always allowed me to work on my own ideas, still providing me with his valuable guidance. I am forever indebted with Carlos Lourenço, always available to help and support me throughout these years. I profited a lot from his knowledge and patience. I would like to thank Ruben Shahoian, for the innumerable useful discussions and for having shared with me the (few) good and the (many) bad times... Working with them was an unforgettable experience.

A special thanks goes to Vittorio Palmieri. I will never forget when he woke me up on an early Sunday morning to share with me his crazy ideas about cryogenic silicon detectors... This was the start of an incredible adventure, carried out with passion and fun, as only friends are able to do.

I am especially grateful to Gaspar Barreira and Mario Pimenta, for having always supported me throughout these years. Tapio Niinikoski and Klaus Pretzl are warmly acknowledged for their constant encouraging support and for their sincere friendship. I would like to thank Erik Heijne for having introduced me to the fine art of pixel detectors, and Eugenio Cantatore, Michael Campbell, and Walter Snoeys for their precious advises on electronics and detectors. It was a pleasure to share the work and the responsibility for the test pixel spectrometer with Iztok Ropotar.

It is impossible to list all the people from the NA50, RD39, ALICE, RD19, and COMPASS collaborations with which I had the privilege and the pleasure to work: I thank them all. I would like to acknowledge the full secretariat crew of LIP, who has always been very friendly and helpful.

During these years I could always feel, despite 1150 km, the warm support of all my family. They always believed in me and were a constant source of encouragement. There are no words to thank Barbara, who took care of me beyond any natural limit. Finally, a big thanks to the unforgettable members of the mercenary troop: Antonello, Cinzia, Gennaro, Francesco, Steven, Ruth and Valeria.

The financial support of European Community (TMR Program, contract n. ERBFMBICT961204), and LIP (Laboratório de Instrumentação e Física Experimental de Partículas) is gratefully acknowledged (what can you do without money...).

Table of contents

Introduction

The Quark-Gluon Plasma (QGP), a deconfined phase of quark and gluons, is predicted by QCD, the theory that describes strong interactions, to be created when nuclear matter is heated or compressed beyond certain limits. Collisions of heavy ions provide the only available way to form a QGP in the laboratory. The heavy ion program at the CERN-SPS, started in 1986, has reached a promising stage. Thanks to the important developments provided by the Pb beam, the present collection of experimental results provides strong support for the expectation that matter with a structure radically different from nuclear or hadronic matter is created in Pb-Pb collisions.

The most striking experimental observation concerns the anomalous suppression of J/ψ production (by NA50). Then follow the excess emission of lepton pairs in the mass range below the ρ resonance (by CERES), the enhanced production of multi-strange hadrons (by NA57), and a certain increase in entropy and strangeness production (by NA49). Furthermore, several experiments (NA38, Helios-3 and NA50) have observed an enhanced production of dimuons with mass between 1.2 and 2.5 GeV, which may be an indication for charm enhancement or for the production of thermal dimuons.

The subject of this thesis is the conception of an experiment to perform an accurate study of dimuon production in heavy ion collisions. Dimuon spectrometers rely on a *hadron absorber*, which absorbs all emitted particles except muons, and separates the target area, where the interaction rate is high, from the downstream region, where the muons are identified and measured. Such an apparatus provides a highly selective *dimuon trigger* that allows the study of *very low cross section processes*.

So far it was not possible to measure the muons in the high multiplicity region before they enter the absorber, where they suffer multiple scattering, and this resulted in limited measurement accuracy. A drastic improvement of the performance of dimuon spectrometers can be achieved by inserting in the target region a vertex spectrometer equipped with *pixel detectors*, which is a matrix of finely segmented silicon sensors (~4000 cells/cm^2). Each pixel is directly connected to a readout cell of the same size, containing miniaturized readout electronics. This high granularity detector is able to distinguish and measure the hundreds of charged particles created in heavy ion collisions right after the target, and even at high interaction rates.

This thesis covers the work needed to go from the idea of a new detector concept to its implementation. The idea consists in combining the dimuon spectrometer presently used by the NA50 experiment with a pixel vertex spectrometer. Using a *track-matching* procedure based on the comparison of the momenta and angles as measured before and after the hadron absorber, it is possible to identify among all tracks reconstructed in the vertex spectrometer the muons that gave the trigger.

By precisely measuring the muon angles in the vertex spectrometer, before they suffer multiple scattering in the absorber, a substantial improvement of the dimuon mass resolution can be obtained. Furthermore, the main source of background, which consists of the random muon pairs generated by the copious π and K decays, is considerably reduced as the parent meson seldom satisfies the matching criteria. Thanks to the improved measurement accuracy it becomes possible to study separately the production of the ω and ρ mesons. Moreover, one can extrapolate the tracks to the interaction point and measure their *offset*, i.e. the distance (in the transverse plane) between the interaction point and the track extrapolation. Selecting tracks in a determined offset range, it is possible to define an event sample highly enriched of semi-leptonic decays of pairs of charmed mesons ($D\overline{D}$). The vertex spectrometer would allow clarifying whether the observed dimuon excess in the mass window from 1.2 to 2.5 GeV is due to prompt dimuons or to muon pairs generated by charm decays.

We have built a low-budget *test pixel telescope* using the available Ω3/LHC1 pixel detector, developed by the CERN-RD19 collaboration. The telescope was installed inside a dipole magnet upstream of the NA50 dimuon spectrometer, and exposed to proton and Pb beams. Due to the limited pixel chips availability, the vertex tracking detector covered only half of the angular acceptance of the muon spectrometer. Despite the low statistics that we collected, due to the limited geometrical coverage and beam time, and to the low detector efficiency, caused by radiation damage, we obtained rather promising results. We have indeed demonstrated the expected improvement in mass resolution (20 MeV at the mass of the ω) in p-Be collisions. Moreover, the track matching procedure was shown to work up to head-on Pb-Pb collisions.

Radiation damage is a concern for detectors exposed to Pb-Pb collisions, especially if one looks for rare processes as charm decays, when high statistics is needed. Particles traversing a silicon detector may dislodge an atom from its position in the lattice. If the kinetic energy of the recoil atom is sufficiently high, this can in turn displace other atoms, eventually generating a cascade. The number of primary defects induced in the silicon bulk depends on the type of particle and its energy. If the number of these radiation-induced defects is high enough (larger than the *doping* concentration before irradiation), the detector performance is seriously deteriorated.

Radiation also induces damage in electronics circuitry. In the case of CMOS devices (which is the technology used for the pixel detectors discussed in this thesis), the damage is created by ionizing particles, which generate charge in the insulating oxides. The accumulated charge can cause the increase of leakage current in the integrated circuit, and shift in the operating point of the transistors. These effects lead to the mal-functioning of the irradiated device, eventually becoming no longer operational.

The Ω3/LHC1 pixel readout chip fulfilled our requirements in terms of spatial (pixel size $50 \times 500\ \mu m^2$) and time resolution. However it could not stand, as mentioned before, even the radiation dose (~30 krad) accumulated during the short tests. For this reason, we decided to investigate the development of a new chip, suitable for the intended experiment.

We tested two pixel readout chip prototypes, manufactured in commercial 0.5 μm and 0.25 μm CMOS technologies. Both prototypes were designed using a special radiation-hard transistor layout (*enclosed layout*). The first prototype chip was found to stand up to ~1 Mrad, but the component density allowed by the 0.5 μm technology was not enough to fit all the circuitry in the wanted pixel size ($50 \times 300\ \mu m^2$). The 0.25 μm technology, used to produce the second prototype chip, was instead found to be dense enough for our applications. Furthermore, this chip was measured to be functional up to ~30 Mrad, when irradiated both with X-rays and protons.

We have also investigated the problem of radiation tolerance of silicon detectors. I participated in the discovery of the *Lazarus effect*, namely the experimental observation that heavily irradiated silicon detectors, no longer functional at room temperature, "resuscitate" when operated at T ~ 130 K. We have shown that at cryogenic temperatures the radiation induced defects becomes electrically inactive, extending by more than one order of magnitude the lifetime of standard silicon detectors.

The results achieved with cryogenic silicon detectors in terms of radiation tolerance have opened new perspectives in the field of detector technologies. In particular, we will add to the pixel vertex spectrometer a new beam-tagging detector (named "beam-scope"), made of silicon microstrips operated near 100 K, to measure the transverse coordinates of each incoming ion. The beam-scope will provide a strict constraint in the determination of the interaction point, relative to which the offset of the muon tracks will be determined.

The thesis is organized in the following way. It starts with an overview of QGP and dimuon physics in Chapter 1, where I also briefly discuss the results obtained by the experiments which studies heavy ion collisions at the CERN-SPS. After a description of the NA50 experimental set-up (Chapter 2), I will introduce the silicon detectors and then describe in detail the Ω3/LHC1 pixel detector (Chapter 3), which we have used to build the test vertex spectrometer. The problem of radiation damage in silicon detectors and readout electronics is discussed in Chapters 4 and 5, respectively. Here I present the extraordinary results we obtained on the radiation tolerance of Si detectors operated at cryogenic temperatures and on prototype pixel chips manufactured in standard sub-micron CMOS technology. In Chapter 6, I present the results of the simulation of the physics performance of a dimuon experiment (named NA6i), which makes use of the detector technologies discussed in the previous chapters. Finally, I will present the results obtained with the test pixel vertex spectrometer (Chapter 7), which validate the new detector concept.

Chapter 1

Physics overview

1.1 Introduction to the Quark-Gluon Plasma

Strongly interacting matter is understood at the fundamental level through the interactions of quarks mediated by the exchange of gluons, as described by the Quantum-Chromo Dynamics (QCD) theory. A remarkable feature of the theory is that at short distances (or large momenta), the effective coupling constant α_s decreases logarithmically, i.e. quarks and gluons appear to be weakly coupled. On the contrary, at large distances (or small momenta) the effective coupling has a steep growth, which results in the phenomenon of *colour confinement.*

At sufficiently high temperatures, the binding QCD potential becomes screened, in analogy to the Debye charge screening of QED. In a dense medium, the Coulomb potential between two electric charges becomes screened by the presence of a high charge density ρ:

$$V(r) = \frac{e}{r} \rightarrow \frac{e}{r}\exp\left(-\frac{r}{r_d}\right) \tag{1-1}$$

where $r_d \propto 1/\rho$ is the Debye radius. In a similar way, the colour potential will experience screening in a medium characterised by a high density of colour charges:

$$V(r) = \sigma r - \frac{\alpha_s}{r} \rightarrow \sigma r_c(T) \cdot \left[1 - \exp\left(-\frac{r}{r_c(T)}\right)\right] - \frac{\alpha_s}{r}\exp\left(-\frac{r}{r_c(T)}\right) \tag{1-2}$$

where $r_c(T)$ is the colour screening radius, which is a function of the temperature. When r_c becomes very small, the potential goes to zero causing the hadron to dissolve. In other words, when the temperature increases above a certain threshold, quarks and gluons are not anymore confined inside hadrons. This new phase of QCD is called the *quark-gluon plasma* (QGP). Therefore, a phase transition should exist between a hadron gas, at low temperature, and a QGP, at high temperature.

Quarks confined in hadrons have a non-zero mass, dynamically generated by the interaction with the other quarks and gluons, which give rise to the *chiral symmetry breaking*. The QCD Langrangian has in fact a (chirally symmetric) interaction term plus a term proportional to the mass of the quarks ($<\psi\overline{\psi}>$), which is not invariant to left-right operations. When quarks become free (above the critical temperature T_c) their mass drops to small values (for u and d) and the chiral symmetry is *restored.* It is not uncommon in nature that spontaneously broken symmetries are restored at high temperature through phase transitions. Well-known examples are ferromagnetism, superconductivity, and the transition from solid to liquid and liquid to gas.

Figure 1-1 shows the results of numerical calculations on the behaviour of the *order parameter* $<\psi\bar{\psi}>$, as a function of the temperature of the system. It is also shown the expected behaviour of the *Polyakov exponent L*, which is a parameter related to confinement. One of the most reasonable scenarios is in fact that chiral symmetry is restored at the same critical temperature T_c when deconfinement occurs.

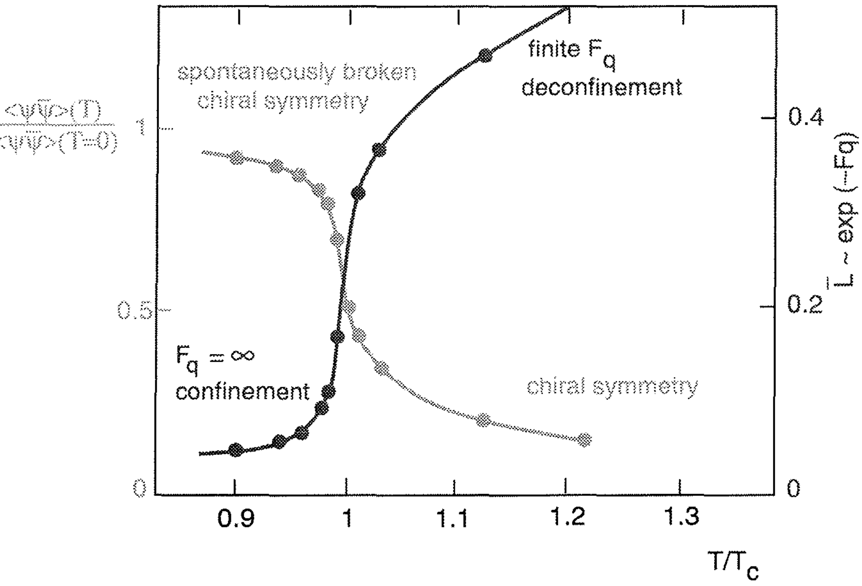

Figure 1-1: Result from lattice QCD calculations showing that the chiral symmetry is restored at the same T_c as the deconfinement phase transition.

Perturbative QCD can only be applied for small values of the coupling constant α_s. When studying nuclear matter under extreme temperature and/or density conditions, the perturbative approach has to be replaced by *lattice QCD* [1]. Numerical lattice QCD simulations have computed the phase transition temperature to be in the range 150-200 MeV. It is worth mentioning that, according to standard cosmological models, the temperature of the cosmic background radiation exceeded 200 MeV during the first 10 μs after the Big Bang. The early universe was then in a quark-gluon plasma state, rather than composed by hadrons.

Let us consider a system consisting of hadrons in the vacuum and compress it. As the density increases, the hadrons start overlapping among themselves. Since the QCD binding potential becomes screened, the quarks would freely move over distances much larger than those available inside the hadrons in which they were confined.

Figure 1-2 shows the phase diagram of temperature versus baryon chemical potential μ_B [2] showing the phase boundary $T_c(\mu_B)$. For $T < T_c(\mu_B)$ the strongly interacting matter is composed by hadrons, whereas for $T > T_c(\mu_B)$ we have the transition to a the plasma of free quarks and gluons. In the figure are also shown the experimentally measured temperatures reached at several accelerator facilities. There is a clear indication that the phase transition is within reach already at the CERN-SPS.

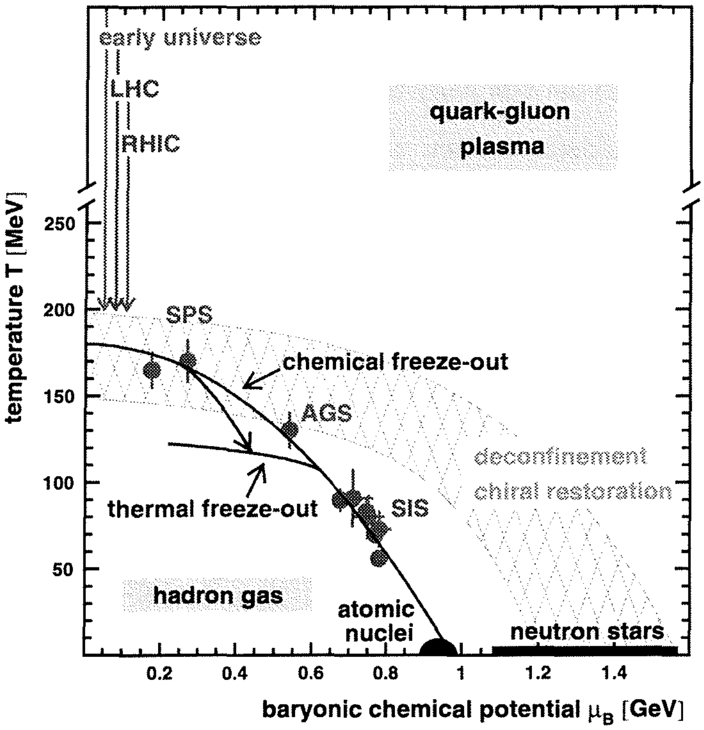

Figure 1-2: Phase diagram showing the phase transition between a hadron gas and a quark-gluon plasma. The temperatures reached at SPS are close to T_C.

Relativistic heavy ion collisions are the only available tool for creating a quark-gluon plasma in the laboratory. In these collisions a complicated mixture of compression and heating of the hadronic matter is created, which may lead to a phase transition. Unlike other phase transitions in physics, in the case of QGP there can not be a direct measurement of the hot phase, because of confinement.

In the following of this chapter, I will briefly overview the variables related to the characteristics of the collision and the signals, which are supposed to be correlated to the existence of deconfined matter.

1.2 Global observables

This category of variables characterising the collision includes the temperature, entropy, energy density, impact parameter, number of participant nucleons, etc. These variables can be derived from measured quantities, in a way that is usually model-dependent.

The energy density reached during the collision can be determined measuring the charged multiplicity or the transverse energy of the collision. The transverse energy of a system with N particles is defined like

$$E_T = \sum_{k=1}^{N} E_k \sin(\theta_k) \cong \sum_{k=1}^{N} m_T{}^k \tag{1-3}$$

where E_K is the energy of the *k-th* particle and θ_k its angle with respect to the beam axis. The transverse mass m_T is defined as $m_T = \sqrt{p_T^2 + m^2}$.

The energy density can be estimated using Bjorken's formula:

$$\varepsilon_{Bj} = \frac{\left.\frac{dN}{dy}\right|_{y=0} \cdot \langle m_T \rangle}{A_T \cdot c\tau} \cong \frac{\left.\frac{dE_T}{dy}\right|_{y=0}}{A_T \cdot c\tau} \qquad (1\text{-}4)$$

where τ is the formation time (~1 fm/*c*) of the equilibrated system; A_T is the transverse cross section of the collision, computed as $A_T \approx \pi r_0^2 A^{2/3}$, with r_0 ~ 1 fm; thus $A_T \cdot c\tau$ is the effective volume of the interaction.

The variable *y* is the rapidity, defined as:

$$y = \frac{1}{2} \ln \frac{E + p_L}{E - p_L} = \ln \frac{E + p_L}{m_T} \qquad (1\text{-}5)$$

For $p \gg m$, the rapidity can be expanded to obtain:

$$y \approx \frac{1}{2} \ln \frac{\cos^2(\theta/2)}{\sin^2(\theta/2)} = -\ln \tan(\theta/2) \equiv \eta \qquad (1\text{-}6)$$

where $cos\theta = p_L/p$. The pseudo-rapidity η can be measured when the mass and momentum of the particle is unknown.

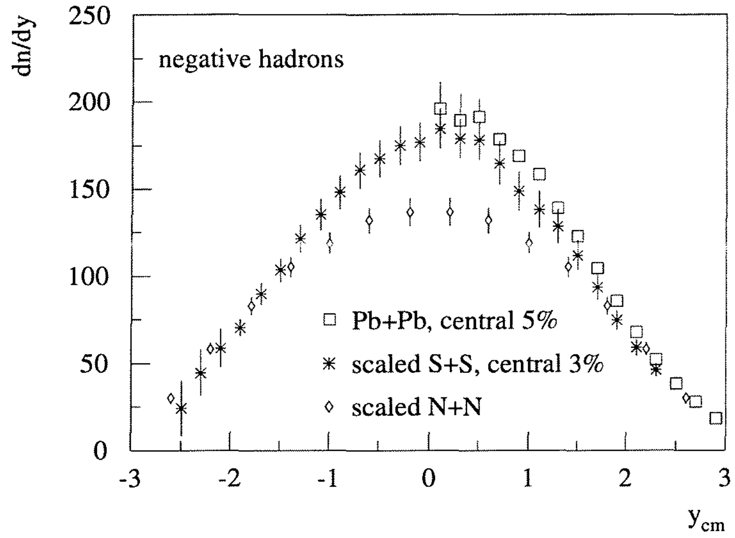

Figure 1-3: Rapidity distribution of negative charged hadrons as measured by NA35 and NA49 [3]. The N+N and S+S data are scaled with the number of participant nucleons (as determined by the ZDC measurement).

$(dN/dy)|_{y=0}$ is the multiplicity per unit of rapidity at mid-rapidity. $(dE_T/dy)|_{y=0}$ is the transverse energy per unit of rapidity at mid-rapidity. In symmetric collision systems, as p-p, S-S or Pb-Pb, the rapidity distributions are symmetric and peak at y = 0, in the centre of mass reference system. An example is given in Figure 1-3. The rapidity distributions are approximately Gaussian. In the case of the pions, the width of the distribution (r.m.s.) has been seen to agree well with Landau's prediction, $\sigma_y = \sqrt{\ln \gamma}$, with $\gamma = (1-\beta^2)^{-1/2}$ of the projectile.

The transverse and forward energy distributions are strongly correlated, according to relatively simple geometrical models, to the impact parameter, the number of participant nucleons and the number of nucleon-nucleon collisions.

The temperature of the system can be estimated from the transverse momentum distribution of the produced particles. In first approximation, the heavy ion collision dynamics can be expressed in terms of a collective longitudinal flow and a transverse thermal spectrum. The production cross section of a particle with transverse mass m_T, is always Boltzman-like:

$$\frac{1}{p_T}\frac{d\sigma}{dp_T} = \frac{1}{m_T}\frac{d\sigma}{dm_T} \propto m_T^{\alpha}\, e^{-m_T/T} \qquad (1\text{-}7)$$

where $\alpha = 0$ or $1/2$ if the distribution is differential or integrated over rapidity.

For p-p scattering, Hagedorn has shown [4] that T is a temperature which tends at higher energies towards a limiting value $T_H \cong 160$ MeV. This is due to the exponential hadronic mass sepctrum, $dN/dm \propto exp(m/T)$, and not to thermalization of the final state particles.

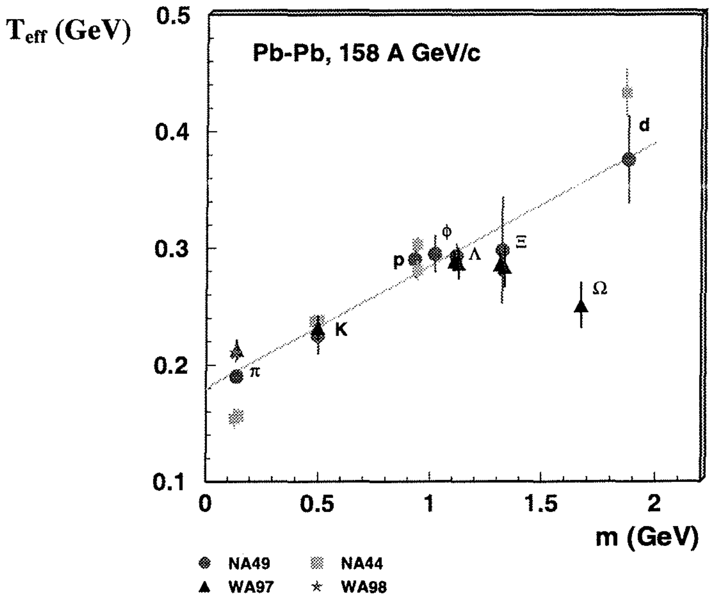

Figure 1-4 Extracted T_{eff} values versus mass m of the particle in Pb-Pb [5].

Thermalization has been demonstrated for S-S and Pb-Pb collisions by the fact that the inverse slope parameter T_{eff} of Figure 1-4 contains a collective flow contribution, which is proportional both to the produced particles' mass m and to the atomic number A of the colliding ions. In more practical terms, one can extract the value of the temperature of the system from the measured p_T spectra. However, one needs to take into account the collective transverse flow contribution, which depends on the size of the colliding nuclei and on the energy of the collision, and affects in the same way all produced particle.

Finally the dimension of the system produced in the collision can be determined via Handbury-Brown-Twiss (HBT) interferometry. This method was originally used to measure the dimension of the stars, but it can be applied to any thermalised incoherent source of bosons. Identical particle interferometry, for instance via π–π, K-K or N-N correlations, yields information on the reaction geometry and provides information about the space-time dynamics of the collisions. By studying the two-particle correlation, it is possible to obtain measurements of the transverse and longitudinal sizes, and of the lifetime, of the hadronic fireball when it breaks up into separate hadrons.

1.3 Plasma signatures

It is possible to schematise the time evolution of nucleus-nucleus collisions as follows. There should be an initial stage in which there are many collisions at the parton level, with a large number of energetic partons formed, and a large amount of entropy created. A thermalised stage is then reached via the numerous scatterings among partons. If the temperature is high enough, the system is a quark-gluon plasma. As the temperature goes through its critical value, some part of the plasma hadronises, giving life to a mixed phase. Finally, the thermalised dense hadron gas decouples, and its debris reaches the detector.

Different experimental *probes* bring information about different stages of the space-time evolution of the system. Several effects have been proposed in particular as possible ways to experimentally detect the formation of QGP.

It is clear that the final state hadrons, after the hadronization and freeze out stages, provide only indirect information on the characteristics of the very early stages of the collision, when a quark gluon plasma phase may have formed. In contrast to the hadrons, thermal photons and lepton pairs provide information about the earlier phases, from which they can easily escape, since they do not undergo strong interactions with the surrounding hadronic matter. However, the photons and lepton pairs thermally produced in the interior of the QGP have rather small yields and hidden under the large backgrounds from Drell-Yan and electromagnetic hadron decays.

An important signal of the presence of a deconfined state of matter is the suppression of charmonium. It was proposed by Matsui and Satz in 1986 [6], that the J/ψ vector meson should have its production strongly suppressed if a QGP was formed in nuclear collisions. This suppression can be seen as resulting from the breaking of the $c\bar{c}$ bound states by high momentum gluons. In the case of excited states of the $c\bar{c}$ system, such as the ψ' and χ_c, the binding energy of the pair of quarks is smaller than for the J/ψ. Thus they are easier to dissociate into open charm, by recombination of the c and $\bar{c}$ quarks with $\bar{u}$ or $\bar{d}$, respectively *u* or *d* quarks. They should disappear as soon as the temperature exceeds T_c, while the J/ψ dissociation requires harder gluons, only available when the collision reaches higher energy densities.

A strong enhancement of the multi-strange hyperon production yield is also considered a signal of QGP formation. The production of hadrons containing strange quarks is normally suppressed in hadronic reactions compared to the production of hadrons containing only *u* and *d* valence quarks (and/or anti-quarks). The yield of multi-strange baryons and anti-baryons is therefore expected to be strongly enhanced in the presence of a QGP.

Lepton pairs can also provide information about the in medium modifications of hadronic properties. In particular, in case of chiral symmetry restoration the spectral shapes of the ρ meson and of its chiral partner, the a_1, should become degenerate, leading to a clearly visible change of the dilepton mass spectra below 1 GeV.

1.4 Dilepton physics

In this section, I will briefly describe the different processes contributing to the lepton pair mass spectrum, in particular concentrating on the case of muon pairs.

The main feature of the dimuon mass spectrum at high masses is the exponentially decreasing continuum due to quark-antiquark annihilation (Drell-Yan mechanism):

$$q\bar{q} \to \gamma^* \to \mu^+\mu^- \qquad (1\text{-}8)$$

The electromagnetic decays of vector mesons through a virtual photon

$$V \to \gamma^* \to \mu^+\mu^- \qquad (1\text{-}9)$$

add to the global continuum a prominent structure of resonances. Therefore, we distinguish a *high mass region*, characterised by the J/ψ, ψ′ and ϒ resonances superimposed on the Drell-Yan continuum, and a *low mass region*. This part of the mass spectrum is dominated by the low mass vector mesons (ρ, ω, ϕ) standing out of a very complex structure, involving, in particular, the Dalitz decays of the ω, η and η′. The simultaneous semileptonic decays of charmed mesons ($D\bar{D}$) is important mainly in the mass region between the ϕ and the J/ψ (*intermediate mass region*).

1.4.1 Drell-Yan process

Quarks and anti-quarks that share the same flavour can annihilate with the leading order (LO) electromagnetic cross section given by QED:

$$\sigma_i(q_i\bar{q}_i \to \gamma^*) = \frac{4\pi\alpha^2}{3M^2} e_i^2 \qquad (1\text{-}10)$$

where e_i is the quark electric charge and *M* is the mass of the produced virtual photon, i.e. the invariant mass of the lepton pair to which it couples. In order to compute the Drell-Yan cross section in the collision between two hadrons, *P* (projectile) and *T* (target), we need to convolute the factor given by Equation 1-10 with the probability to find a quark q_i

and an anti-quark $\bar{q}_i$ in the hadrons, which is given by the parton distribution functions. These functions depend on the fraction x of the hadron's longitudinal momentum (which we call x_P for the projectile and x_T for the target) carried by the parton. The differential Drell-Yan cross section in LO is then:

$$\frac{d^2\sigma}{dx_P dx_T} = \frac{1}{3}\cdot\frac{4\pi\alpha^2}{3M^2}\cdot\sum_i e_i^2\left[f_i^P\left(x_P,M^2\right)\bar{f}_i^T\left(x_T,M^2\right)+\bar{f}_i^P\left(x_P,M^2\right)f_i^T\left(x_T,M^2\right)\right] \qquad (1\text{-}11)$$

where the factor 1/3 ensures that we count annihilations of a quark only with its corresponding anti-quark of same colour. This cross section under-predicts the experimentally measured values by a factor ~2, the so-called "K factor" defined as the ratio between the measured Drell-Yan cross section and the LO prediction. Nowadays it is possible to calculate the mass and rapidity distributions of Drell-Yan dileptons at the NNLO (next to next to leading order), while the p_T distributions are calculable at the NLO. Therefore, it is now possible to reproduce the measured spectra without the use of any K factor [7].

Drell-Yan is understood to be a hard (parton level) process, not being affected by the surrounding nuclear matter in a hadron-nucleus collision. This implies a linear dependence of the production cross section on the mass number of the nucleus A. The following parametrization is very often used:

$$\sigma_{pA} = \sigma_0 A^\alpha \qquad (1\text{-}12)$$

and the value of α has been experimentally measured, being consistent with unity.

The leading order cross section of Equation 1-11 depends on the charge of the interacting quarks, which can be either valence or sea quarks. Since we are considering interactions among nucleons, there are no valence anti-quarks available. Thus the Drell-Yan process involves only sea anti-quarks. High-mass dimuons require high values of x_P and x_T, where the valence quark distribution dominates. As a consequence, the high-mass Drell-Yan cross section depends on the isospin of the interacting nucleons.

This dependence has been verified in collisions with π^+ and π^- beams. Indeed, the ratio between π^+ and π^- induced collisions, tends, at high masses, towards the ratio of the valence anti-quark electric charge squared: $e_{\bar{d}}^{\,2}/e_{\bar{u}}^{\,2} = 1/4$.

A quite pertinent question concerns the lowest mass value where it is still possible to apply the Drell-Yan description used so far. The calculation of the Drell-Yan process by QCD should only be trusted for high momentum transfers, i.e. for high invariant mass values, say above 4 or 5 GeV. However, it turns out that the spectrum calculated for the lower mass regions is observed not to disagree with the available data. The clarification of this question requires appropriate calculations of the Drell-Yan contribution to the low mass and high p_T kinematics window and a good measurement of prompt dimuon production, down to the lowest possible dimuon masses and at high transverse momentum.

1.4.2 Open charm

Charmed hadrons are generated by parton interactions where $c\bar{c}$ pairs are produced, followed by hadronization in charmed baryons or mesons, mainly D and $\bar{D}$. The dominant production process at SPS energies, around 80% of the cross section, proceeds via gluon fusion $gg \rightarrow c\bar{c}$.

Figure 1-5 shows the absolute cross section of $c\bar{c}$ production as a function of the centre of mass energy, as measured by several experiments in πN and pN reactions. In all cases (except the NA50 point, for which see [8]), the total inclusive $D\bar{D}$ cross-section is obtained adding the directly measured different contributions from the single charmed mesons D^+, D^-, D^0 and $\bar{D}^0$. Starting from these data, and taking into account the estimated limit on the extra contribution from the associated $\Lambda_c\bar{D}$ and $\bar{\Lambda}_c D$ production, it is possible to extract the $c\bar{c}$ production cross-section. The curve in the figure is the result of PYTHIA [9] calculations.

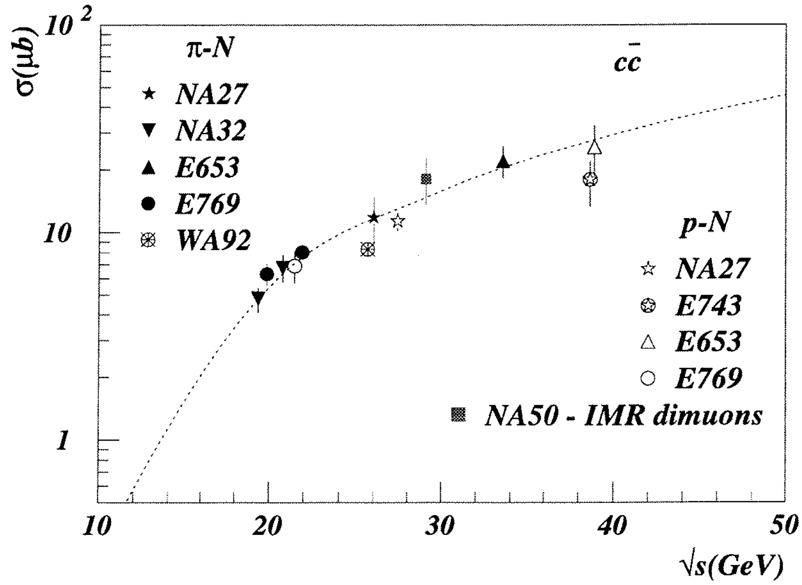

Figure 1-5: Cross section for forward ($x_F > 0$) $c\bar{c}$ production as a function of the centre of mass energy. The data are in agreement with expectations based on perturbative QCD and normalised to the data by choosing an appropriate K_c factor.

Similarly to Drell-Yan, charm production is a hard process and its cross section is expected to increase linearly with the mass number A. Furthermore, and in contrast to Drell-Yan production, the isospin effects can be neglected, since charm production is understood as being mainly produced through gluon fusion, the quark-antiquark annihilation playing a minor role. The latest experimental data gives support to these expectations. The E769 collaboration has measured the value $\alpha = 1.00 \pm 0.05 \pm 0.02$ for $D\bar{D}$ production by 250 GeV pions [10].

At SPS energies (even in Pb-Pb collisions) charm production is rare, leading to creation of at most one single pair of D mesons. When both D mesons decay semi-leptonically, through the muon channel, an opposite-sign muon pair results. It is worth stressing that, unlike the decays of pions and kaons, the simultaneous semi-leptonic decays of $D\overline{D}$ pairs cannot lead to like-sign muon pairs (which are the main source of background in dimuon experiments).

1.4.3 Resonances

Besides the 'continuous' processes, Drell-Yan and open charm decays, the dimuon mass spectrum receives considerable contributions from the Dalitz decays of the mesons η, η' and ω, and from the 2-body decays of the vector mesons ρ, ω, ϕ, J/ψ and ψ'. A detailed description of the different signals, which contribute to the low-mass dilepton spectrum is out of the scope of this thesis. The different contributions can be observed in Figure 1-6.

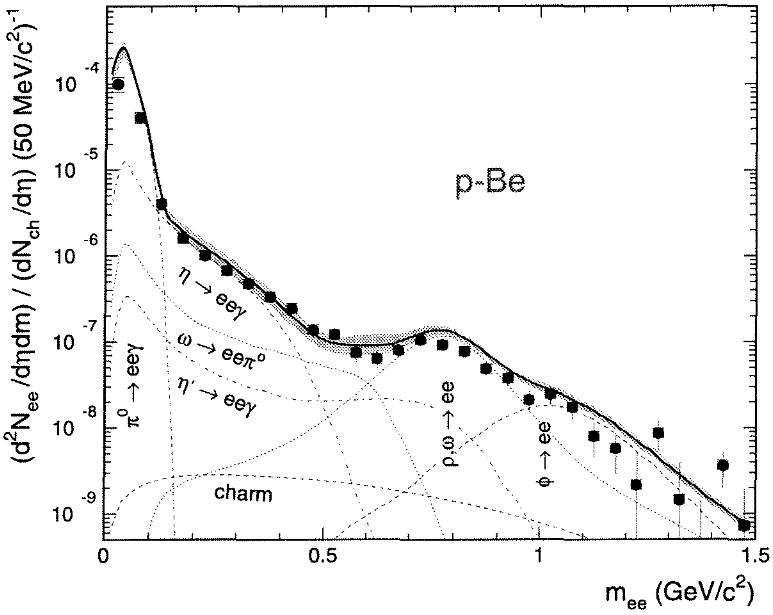

Figure 1-6: Dielectron mass spectrum as measured by the CERES collaboration in pBe collisions [11]. The experimental points are in a good agreement with the curve, which is obtained as the sum of all known signals contributing to the dilepton spectrum.

The NA51 and NA38 collaborations, which used basically the same experimental set-up, have measured the J/ψ production cross section in p-p and p-A collisions at 450 GeV/c, and p-A and nucleus-nucleus collisions at 200 GeV/c. The kinematical window was $|\cos(\theta)| < 0.5$ and $3 < y_{lab} < 4$. The measured values are plotted in Figure 1-7

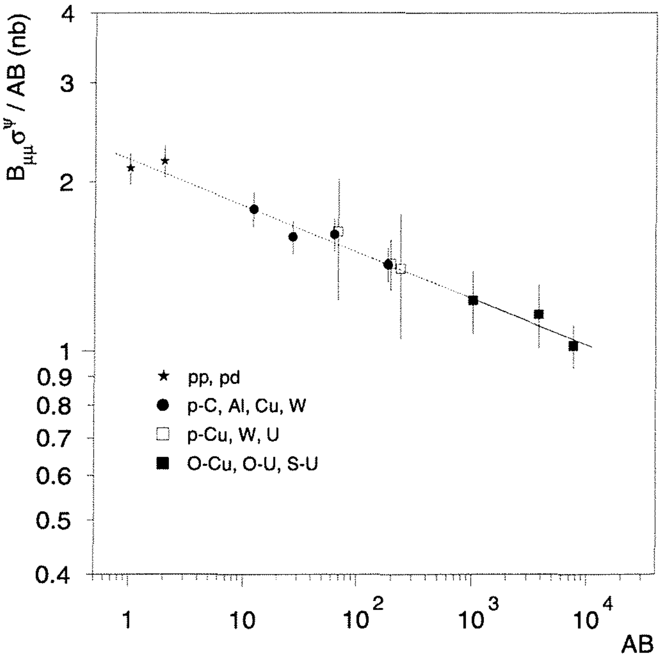

Figure 1-7: J/ψ production cross section as a function of number of participants. The extracted value for α(J/ψ) is 0.92 [12].

The values measured at 200 GeV/c have been re-scaled to 450 GeV/c according to the so-called "Schuler parametrization" [13]:

$$\frac{B\cdot\sigma(J/\psi)}{A^{0.91}} = 37\times\left(1-\frac{3.1}{\sqrt{s}}\right)^{12}(nb) \qquad (1\text{-}13)$$

The J/ψ production cross section has been also measured in Pb-Pb at 158 GeV/c per nucleon by the NA50 experiment. The results will be discussed in Section 1.5.1.

1.5 Present results

Recent experimental observations require for their description more than our present understanding of the standard model of hadronic interactions, giving strong indications that a QGP is formed in heavy-ion collisions at the CERN-SPS. In the following, I will briefly review the most important results recently obtained by the SPS experiments.

1.5.1 J/ψ suppression

The most striking result recently obtained at the CERN-SPS is the evidence provided by NA50 for an anomalous mechanism of J/ψ suppression in Pb-Pb collisions [14]. Figure 1-8 shows the J/ψ production cross-section normalised to the Drell-Yan process as a function of L, the thickness of nuclear matter crossed by the $c\bar{c}$ pair, in p-A, S-U and Pb-Pb collisions. In the last case, the J/ψ is also normalised to the minimum bias spectrum.

The results show two different absorption mechanism. The *hadronic absorption,* which is a function of the number of participants (see Figure 1-7), describes the data from p-p to central S-U collisions. In the case of Pb-Pb reactions, an extra absorption with a sharp threshold appears when going from peripheral to central collisions. The observation of a threshold behaviour in a single collision system is a clear indication for the transition to deconfined QCD matter [15]. In fact, two consecutive thresholds are expected to occur, due to the dissolution of the χ_c and J/ψ states at different energy densities. This is due to the fact that ~40% of the produced J/ψ are actually the result of χ_c production, followed by their radiative decays, $\chi_c \rightarrow J/\psi + \gamma$.

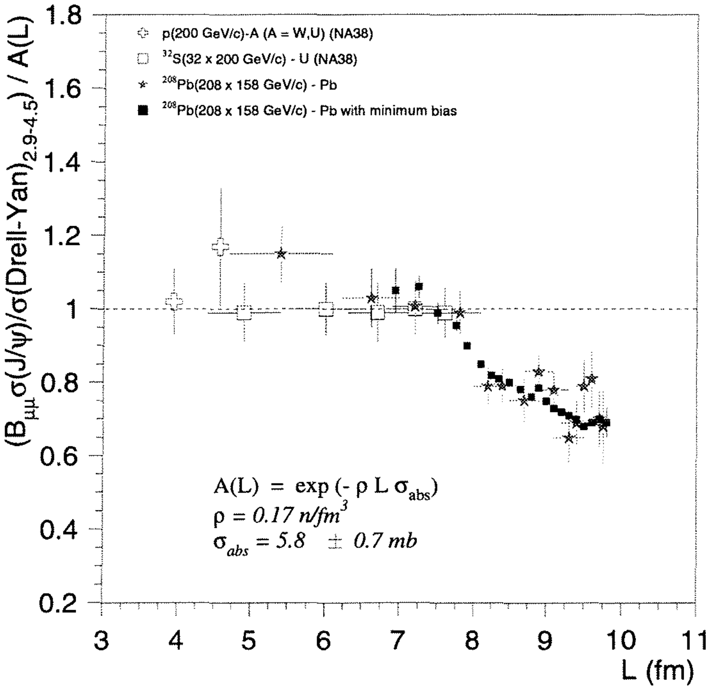

Figure 1-8: J/ψ production cross section normalised to Drell-Yan measured in several systems. In the case of Pb-Pb, the cross section has been also normalised to the minimum bias events.

However, the final interpretation of these observations would considerably benefit from direct and independent knowledge about the gluon content of the matter produced in the early stages of the heavy ion collisions. Such information could be provided by a measurement of charmed meson production (see next section). Indeed, due to the large mass of the *c* quark, charmed mesons are predominantly produced by gluon fusion in the early hard scattering processes. Besides helping to clarify the mechanisms of production and suppression of the bound $c\bar{c}$ charmonia states, a good knowledge on the gluon content is also important to the understanding of the QGP properties.

1.5.2 Charm production

The production of charm quarks leads mainly to correlated pairs of D and $\overline{D}$ mesons. Only a few percent of the charmed quark pairs end up in the bound charmonia states.

The NA38/NA50 and Helios-3 experiments have observed that the dimuon continuum between the ϕ and the J/ψ is enhanced in heavy ion collisions, with respect to the expected superposition of Drell-Yan and $D\overline{D}$ sources, which on the contrary explain well the p-A data. Figure 1-9 shows the excess measured in Pb-Pb collisions by the NA50 experiment. It has been shown [16] that an enhancement of the charm production cross-section would explain the observations, providing also a reasonable description of the mass and p_T distributions of the measured data.

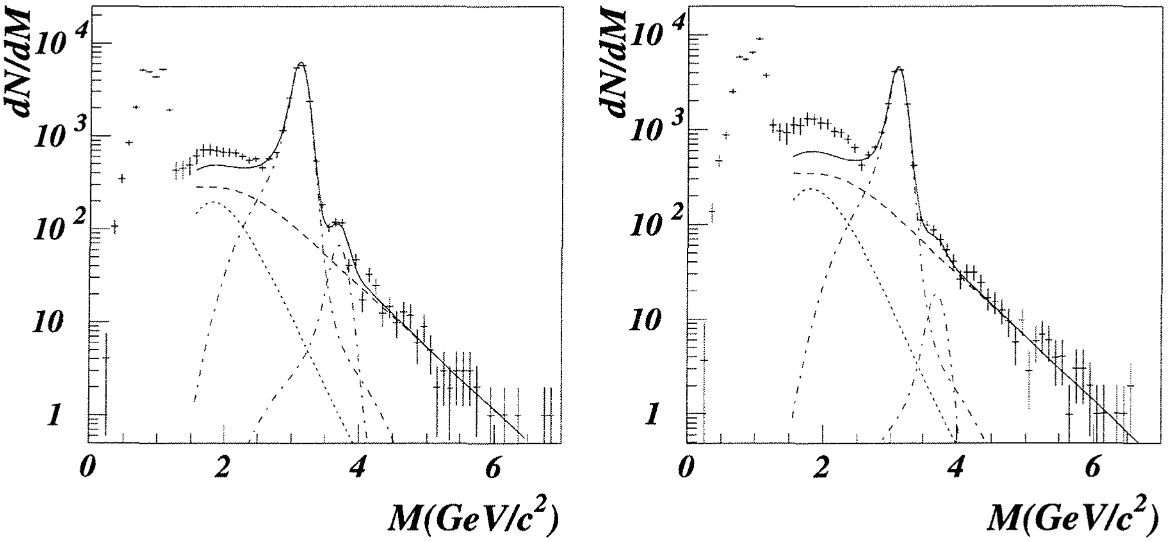

Figure 1-9: Comparison between data and the sum of expected sources (solid line) for peripheral ($<N_{part}>=110$) and a central ($<N_{part}>=381$) Pb-Pb collisions. The D-Y (dashed line), J/ψ, ψ' (dashed-dotted line) and $D\overline{D}$ (dotted line) contributions are also shown. The excess in the intermediate mass region is clearly visible.

While these observations are still the subject of debate, it is clear that an enhancement of charm production in heavy ion collisions would have direct implications on the interpretation of the charmonia data, boosting the anomaly of the measured J/ψ suppression.

The present situation reinforces the importance of having a direct measurement of open charm production in heavy ion collisions. Such a measurement requires a dedicated SPS experiment, that can cope with the high particle multiplicity reached in the most central Pb-Pb collisions (almost 400 charged particles per unit rapidity at mid-rapidity) and with the small D production cross section.

1.5.3 Low-mass lepton pairs

The CERES experiment has observed that the measured yield of low-mass e^+e^- pairs in Pb-Au collisions exceeds by a factor of 3 to 4 the expected signal from hadronic decays [17]. This is shown in Figure 1-10, where the dashed line represents the expected spectrum. The excess dileptons are concentrated at low p_T and their yield scales with the square of the charged particle multiplicity. Dileptons from $\pi^+\pi^-$ annihilations (light solid line) cannot account for the observed shape of the excess yield.

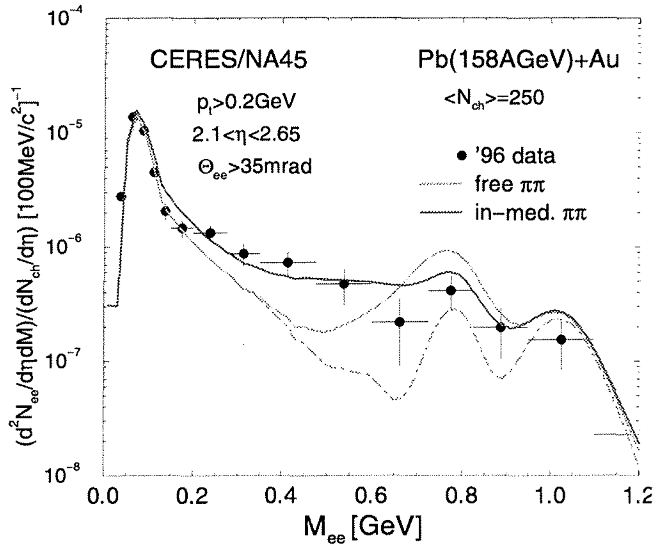

Figure 1-10: Dielectron mass spectrum as measured by Ceres in Pb-Au [17]. The data show an excess of the signal with respect to the expected contribution from known sources.

These observations are consistent with the expectation that the properties of the vector mesons should change when produced in dense matter, due to medium effects. In particular, near the phase transition to the quark-gluon phase, partial restoration of chiral symmetry should induce changes in the masses and decay widths of the mesons. The short lifetime of the ρ meson, shorter than the expected lifetime of the dense system produced in the SPS heavy ion collisions, makes it a sensitive probe of medium effects and, in particular, of chiral symmetry restoration.

Clearly, high precision data are needed to distinguish between the different theoretical models and to determine the relation between the present observations and chiral symmetry restoration. Such data should be able to separate the ω from the ρ, with a good signal to background ratio, and should have enough statistics to allow a detailed study of the observed behaviour as a function of centrality and transverse momentum.

1.5.4 Strangeness enhancement

The observation of enhanced production of strangeness in nuclear collisions is now well established, from the most common ($K^{\pm}$, measured by NA49) to the most exotic ($\overline{\Xi}, \Omega^-$ and $\overline{\Omega}^-$, measured by WA97) particle production processes. The enhancement observed by WA97 of the hyperon and anti-hyperon yields in Pb-Pb collisions [18], relative to the p-Be and p-Pb values, grows with the strangeness content, culminating in an enhancement factor of more than a factor 15 for the $\Omega^- + \overline{\Omega}^-$. The observations follow the behaviour expected if the strange quarks were equilibrated in a deconfined and chirally symmetric quark-gluon plasma. In contrast, current models for production, for example, of $\overline{\Omega}^-$ in a hadron gas, involve a long series of elementary reactions, and takes a long time, hardly compatible with the lifetime measured via HBT interferometry.

Similar enhancement has been measured for hidden strangeness, i.e. the ϕ ($\approx s\bar{s}$) meson, in particular by NA38 and NA50.

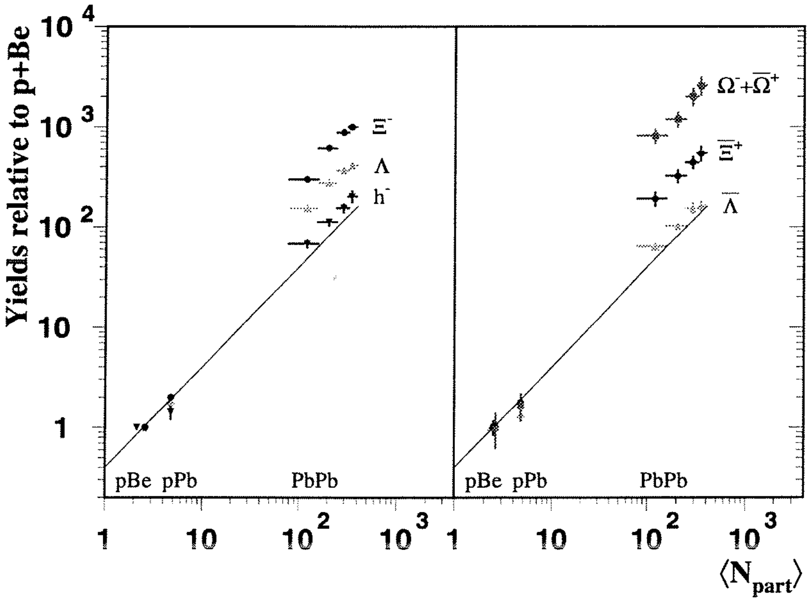

Figure 1-11: Hyperons yield versus number of participants as measured by the WA97 experiment in pBe, pPb and Pb-Pb collisions [18] for particles with (left) and without (right) quarks in common with the colliding nuclei.

References

[1] G.A. Alves et al., Phys. Rev. Lett. 77 (1996) 2388

S. Barlag et al., Phys. Lett. B247 (1990) 113

[2] U. Heinz, private communication.

[3] P. Jacobs (NA49 Coll.), private communication.

[4] R. Hagedorn, Suppl, Nuovo Cimento 3 (1965) 147

[5] R. Lietava (WA97 Coll.), private communication.

[6] T. Matsui and H. Satz, Phys. Lett. B 178 (1986) 116

[7] W.L. Neerven, Int. J. Mod. Phys. A10 (1995) 2921 and references therein.

[8] M.C. Abreu et al (NA50 Coll.), in preparation.

[9] T. Sjöstrand, Comp. Phys. Comm. 82 (1994) 74

[10] G.A. Alves et al. (E769 Coll.), Phys. Rev. Lett. 70 (1993) 722

[11] G. Agakichiev et al. (CERES Coll.), Euro. Phys. J. C4 (1998) 231.

[12] M.C. Abreu et al. (NA38 Coll.), Phys. Lett. B 466 (1999) 408

[13] G.A. Schuler, CERN-TH.7170/94

[14] M.C. Abreu et al. (NA50 Coll.), Phys. Lett. B450 (1999) 456.

[15] H. Satz, in "International School of Subnuclear Physics", A. Zichichi Ed., Erice, Italy, 1997, BI-TP-97-47, hep-ph/9711289

[16] E. Scomparin et al. (NA50 Coll.), J. Phys. G25 (1999) 235

[17] G. Agakichiev et al. (CERES Coll.), Phys. Lett. B422 (1998) 405

[18] P. Norman et al. (WA97 Coll.), XXXIV Rencontres de Moriond, Les Arcs, France, March 1999

Chapter 2

The NA50 experiment

The NA50 experiment makes use of the high intensity CERN-SPS Pb beam to study dimuon production in heavy ion collisions. The aim is to detect those signals, accessible in dimuon production, which were proposed as signatures of the formation of the Quark Gluon Plasma. The experimental apparatus is based on the muon spectrometer previously used by the NA10 and NA38 experiments.

In the original proposal, it was supposed to run with two different spectrometer configurations, optimised for the study of low and high mass dimuons, respectively. Particular attention has been given to the study of *charmonia* production. The main motivation of the experiment was in fact the expectation that the J/ψ production cross-section should be suppressed if produced in presence of deconfined matter [1]. A systematic study of J/ψ production in proton-nucleus and nucleus-nucleus collisions has been carried out and the most important results have already been reported in Section 1.5.1. The intermediate mass region was also studied in detail by NA50 and the results were presented in Section 1.5.2. Concerning the low-mass vector mesons, the dedicated runs with the optimised set-up, which would increase the acceptance for low-mass muon pairs, were never taken.

The project, which is the subject of this thesis, can be considered for many aspects as an up-grade of the NA50 experiment. For this reason, in this chapter I will give an overview of the NA50 design strategy and experimental set-up, before introducing in the final section the new detector concept.

2.1 Detector strategy

Dimuon production represents only a small fraction of the total cross section. In order to pick-up these very rare events among the orders of magnitude more numerous ordinary interactions, NA50 makes use of a dedicated muon spectrometer, originally designed and built for the NA10 experiment (and later used also by NA38). The muon spectrometer relies on a ~5 m long wall, which absorbs the hundreds of charged particles produced in a Pb-Pb collision, letting go through the muons of energy high enough to traverse the absorber. In this way, while the target region is characterised by a very high particle flux, the downstream spectrometer is practically hadron free and provides a very selective dimuon trigger.

In order to study how the signal depends on the characteristics of the collision, the dimuon kinematics must be correlated to the geometry and to the energy density, on an event by event basis. A *zero degree calorimeter* (ZDC), situated after the target on the beam axis, measures the energy not involved in the collision, providing a direct estimate of the number of projectile spectators. Measurements of the charged particle multiplicity and of the transverse energy associated with the interaction are needed to understand how the energy is dissipated in the interaction region. The first quantity is measured by a *multiplicity detector,* placed just after the target, made of silicon microstrips. The neutral transverse energy is measured by an *electromagnetic calorimeter*. Such a detailed event characterisation is important to detect possible deviations from the known correlation between multiplicity, transverse energy flow and longitudinal energy.

Two important parameters, which determine the quality of the measurement of the dimuon mass spectrum, are the mass resolution and the signal to background ratio. There are two contributions to the mass resolution: the error on the measurement of the muon momenta, and the error in the measurement of the muon angles. The first contribution is determined exclusively by the spectrometer resolution (chambers resolution and magnetic field intensity). The second one depends on the multiple scattering, which affects the tracks traversing the absorber. The main source of background consists of accidental muon pairs coming from π and K decays, which are copiously produced in a lead-lead collision.

On one hand, one aims to have the best possible mass resolution, in order to separate the different resonances: the ϕ from the ρ-ω system (and possibly the ω from the ρ), and the ψ' from the J/ψ. This implies minimising the amount of material to be traversed by the muonsr, so that they do not suffer too much multiple scattering. On the other hand, it is vital to absorb the hadrons before they decay, starting the absorber as close as possible to the target, being compatible with the rest of the set-up. The hadron absorber must also be long enough to contain completely the hadronic shower ($> 10\ \lambda_I$), otherwise the first spectrometer chambers would be full of spurious hits, the reconstruction efficiency being seriously affected. A compromise must be found. Materials with high λ_I/X_0 are preferred (graphite, BeO, Al_2O_3). A detailed description of the absorber is given in Section 1.2.3.

2.2 The present experimental set-up

An overview of the apparatus is given in Figure 2-1. We can consider the set-up being composed by two parts: the vertex region and the muon spectrometer separated by the huge hadron absorber. In the first part, we find the beam counters, the active target system, plus the multiplicity detector, the electromagnetic calorimeter and the ZDC, which measure the global variables of the interaction.

The spectrometer measures the kinematics of the dimuons. It consists of a toroidal magnet and 8 multi-wire proportional chambers (MPWC's), which measure the track trajectories before and after the bending in the magnetic field. The trigger signal is generated by the coincidence of four hodoscopes placed before and after the magnet. A coincidence in the last scintillator placed behind a 1.5 m iron wall after the last chamber (thereby not adding further smearing to the tracking) is also required to ensure muon track selection.

The non-interacting beam is dumped in a beam plug placed inside the hadron absorber, after having passed through the ZDC.

The toroidal field of the muon spectrometer allows a mass cut at the trigger level. Indeed, in the acceptance window of the spectrometer, the dimuon mass can be approximated to be $M \approx p^1_T + p^2_T$, where p^i_T is the transverse momentum of the muons. Furthermore, in a toroidal field, the deflection angle of the tracks is inversely proportional to the transverse momentum. Hence, the measurement of the displacement angles give a fast and quite reasonable estimation of the dimuon mass. This way it is possible to study the high mass region, running at high interaction rate (high beam intensity) without overloading the data acquisition system with the much more abundant low mass events.

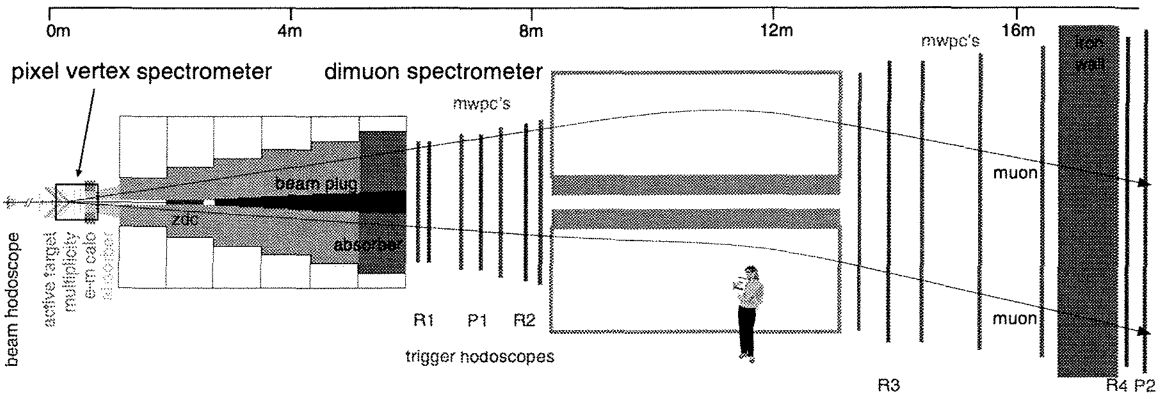

Figure 2-1: NA50 experimental set-up. The box in the vertex region represents the vertex spectrometer, which is the addition to the standard NA50 apparatus, subject of this thesis.

2.2.1 Beam and target

The Pb beam has a momentum of 158 GeV/c per nucleon (or 400 GeV/c per charged particle), gaussian distributed with a $\Delta p/p = 0.1\%$. The transverse beam profile is measured by a proportional wire chamber placed ~70 cm upstream of the target. It contains two perpendicular sets of wires, equally spaced at 0.5 mm distance. Typical values are $\sigma_x = 0.5$ mm, $\sigma_y = 0.45$ mm. The highest possible beam intensity exceeds 10^8 ions per burst of 4 seconds.

A *beam hodoscope* (BH) is used both to identify the incoming ions and provide accurate time of arrival with respect to the trigger. It is located at 33 m from the target, where the beam spot is large enough so that individual incoming ions can be tagged with a detector of reasonable granularity and physical dimensions, without dying of radiation damage. It consists of one plane of sixteen 1 mm thick quartz blades. The Čerenkov light produced by the ions in the blades is read by photo-multipliers (PMs). The analog signals are fed into fast (10 ns gate) ADC's and into TDC's, which record the time of arrival of all incident ions. This information can be used to tag beam pile-up events.

In order to cope with the low dimuon production cross section, the high intensity beam is sent to a long target. Rather than using a single target, NA50 adopts a multiple sub-target system, which allows reducing the probability of interaction of secondaries (pions). The space between sub-targets and their transverse dimensions were optimised to minimise the number of interactions from secondary particles. A monitor system is required to identify in which sub-target the interaction took place.

The NA50 target consists of 7 sub-targets of Pb. Eight pairs of quartz blades placed aside allow identifying in which sub-target the interaction took place. As stated before, the choice of a multiple active target system is due to the necessity of decreasing the re-interaction probability and of rejecting in the off-line analysis the events where a re-interaction occurred. Furthermore, knowing the sub-target, a vertex constraint can be put in the dimuon reconstruction, improving the mass resolution. Indeed, the muon tracks reconstructed in the spectrometer are extrapolated back to the vertex, but with a big uncertainty due to the multiple scattering in the absorber. Knowing the vertex improves the procedure decreasing this uncertainty.

In addition to the Pb beam, also a proton beam is available, used for reference data and calibration purposes. Both primary and secondary proton beams can be provided to the experiment. A 200 GeV/c proton beam is obtained sending the primary SPS beam on a beryllium target placed at about 1'000 m from the experiment target. This beam has a 30% contamination from positively charged pions. A secondary electron beam can be generated and used for the calibration of the electromagnetic calorimeter. The primary proton beam can reach a maximum intensity of a few 10^{10} protons per 2.5 s burst.

2.2.2 The detectors in the target region

The *multiplicity detector* measures the multiplicity and the angular distribution of the charged secondary particles produced in Pb-Pb collisions. Being located just after the target, the multiplicity counter has to cope with a high rate and a high radiation level. The required characteristics are speed, radiation tolerance and granularity.

The multiplicity detector is made up of two wheels of silicon microstrips, located at 184 mm and 316.5 mm from the first sub-target, respectively. The inner radius is 4.4 mm, while the external one is 84 mm. The planes have both azimuthal and radial segmentation, with a strip size that increases with the radius, in such a way that the average occupancy is constant. The total number of channels is 11'400, arranged in circular crowns. The readout is binary.

The *electromagnetic calorimeter* measures the transverse energy carried by (mostly neutral) secondaries and provides thus information on the centrality of the collision and on the energy density reached. It is located downstream of the multiplicity detector and just before the hadron absorber.

The 12 cm thick calorimeter consists of 0.92 mm diameter scintillating fibres embedded in Pb. The volumic ratio is 1:2. The total thickness corresponds to $L_{rad} = 9.4$ mm. The fibres run parallel to the beam. The detector is outside the spectrometer angular acceptance, covering the pseudo-rapidity range $1.5 < \eta_{lab} < 2.3$, in four roughly equal bins. Higher values of pseudo-rapidity are not covered because of the too high radiation load and also not to spoil the dimuon mass resolution. In fact, the inner hole of the calorimeter is filled with low atomic number material (BeO), in order to absorb mesons as soon as possible, without adding too much material in the dimuon acceptance window.

The ZDC is placed inside the hadron absorber (on the beam axis), before the beam dump, at 180 cm from the first sub-target. It measures the energy of that fraction of the beam, which has not interacted. The transverse size is 5×5 cm^2, with an angular acceptance of $\theta < 28$ mrad. The detector consists of quartz scintillating fibres embedded in a passive matrix of tantalum. The choice of quartz was dictated by the requirements of radiation tolerance (typically 2 Grad/month) and of speed (10 ns gate). The fibres are parallel to the beam direction; they are 65 cm long and have a diameter of 365 μm. The volumic ratio between active and passive material is 1:17. The measured energy resolution is 30% with the 200 GeV/c proton beam and 5% with the 158 GeV/c per nucleon Pb beam.

2.2.3 The dimuon spectrometer

The muon spectrometer covers the pseudo-rapidity interval $2.8 < \eta_{lab} < 4.0$. The angles and momenta of the muon tracks are measured in two sets of multi-wire proportional chambers, placed before and after an air gap toroidal magnet. The dimuon trigger is provided by coincidences among four scintillator hodoscopes.

The muon spectrometer is shielded from the high multiplicity target region by a 5.4 m long hadron absorber, made mainly of graphite. In the standard J/ψ configuration, it consists of 420 cm of carbon followed by 80 cm of iron, needed to stop the tail of the showers before they reach the first chamber of the spectrometer. The first 60 cm are made of a denser material (BeO or Al_2O_3), to absorb the pions and kaons before they decay to muons, leading to the combinatorial background of non-correlated (like-sign and opposite-sign) muon pairs, which cause most of the triggers. The muons must traverse a final 1.5 m iron wall before reaching the last trigger hodoscope, increasing to 4 GeV the minimum energy of the detected muons. The absorber has its central part (out of the dimuon acceptance) composed by high Z material (tungsten and uranium), whose aim is to stop the non-interacting beam.

The core of the spectrometer is a 480 cm long hexagonal toroidal magnet. The inner radius is 29.5 cm, while the external one is 154 cm, determining the angular and rapidity acceptance of the apparatus. A relevant fraction of the collected data (30%) has at least one muon passing through the iron of the coils. Since the mass resolution of these events is further deteriorated due to the multiple scattering of the muons, they are rejected from the off-line analysis. This means that the final acceptance is not homogenous as a function of the polar angle, but presents minima in correspondence of the edge of the sextants.

The magnetic field is given by:

$$\vec{B}(r) = \frac{B_0}{r} \cdot \vec{e}_\varphi \qquad (2\text{-}1)$$

where r is the distance from the beam axis, and $\vec{e}_\varphi$ is the axial vector. The field intensity B_0 is determined by the value of the current that flows in the coils. A field integral of 0.219 Tm is measured for a current of 4'000 A, while 0.728 Tm is reached when the current is 10'000 A.

The deflection angle for a particle of charge q and transverse momentum p_T is:

$$\Delta\theta = \frac{0.3 \cdot q \cdot B_0}{p_T \cdot \log(\frac{z_2}{z_1})} \qquad (2\text{-}2)$$

where z_1 and z_2 are the distances of the beginning and the end of the magnet relative to the target position.

The muon tracks are reconstructed by eight MWPC's. The chambers follow the hexagonal shape of the magnet. One chamber is composed by three planes of wires rotated of 60° with respect to each other. The four chambers which are upstream the magnet have smaller size (diameter from 134 to 192 cm) compared to the four downstream (306 to 394 cm). The number of wires increases accordingly to the size, from a minimum of 749 wires in the first chamber to a maximum of 1229 wires in the last one. The precision in the measurement of the track angle is of the order of 0.1 mrad. The gas mixture is argon (80%), isobutan (19.8%) and freon (0.2%), which is fluxed at a rate of half the chamber volume per day.

The trigger signal is provided by 4 hodoscopes (R1 to R4), which also have hexagonal symmetry, being divided in sextants. The scintillator slabs are parallel to the external edge of the sextant. The first two hodoscopes are located upstream of the magnet and are composed by 30 slabs per sextant, whose size increases with increasing distance from the beam axis. In order to ensure that the selected tracks point to the vertex, it is required a coincidence $V = (R1_i \times R2_i)$ or $(R1_i \times R2_{i+1})$, where $i = 1$ to 30 represents the slab number.

Since the scintillators are read by only one photo-multiplier, the time response depends on the impact point of the track in the scintillator. This would create a time jitter. In order to prevent that, the PM's of R1 and R2 are placed on opposite sides and their signal is processed by a *mean timer*, which determines the average time from the two inputs.

The hodoscopes R3 and R4 are downstream the magnet and have 24 and 32 scintillators per sextant, respectively. The coincidence of V with R3 and R4 represents the dimuon trigger, where angular selection can be applied to select mass regions. In particular, R3 is used for the angular selection, while R4 is used only to remove random events.

The hodoscopes P1 and P2, the first placed between R1 and R2 and the second located after R4, are used to monitor the trigger efficiency. Special runs have been taken to measure this efficiency, which was found to be around 90%.

2.3 Present performances and limitations

The main parameters which determine the spectrometer acceptance are the angular coverage of the magnet ($35 < \theta < 120$ mrad), the intensity of the toroidal field, and the number of interaction lengths of the hadron absorber. Figure 2-2 a) shows the acceptance as a function of the mass M and transverse momentum p_T of the dimuon. This has been determined with a simulation program, which generates $\mu^+\mu^-$ pairs, which are then tracked through the NA50 set-up. The plot represents a two-dimensional map of the accepted and reconstructed pairs. The lines in the figure represent constant values of transverse mass m_T.

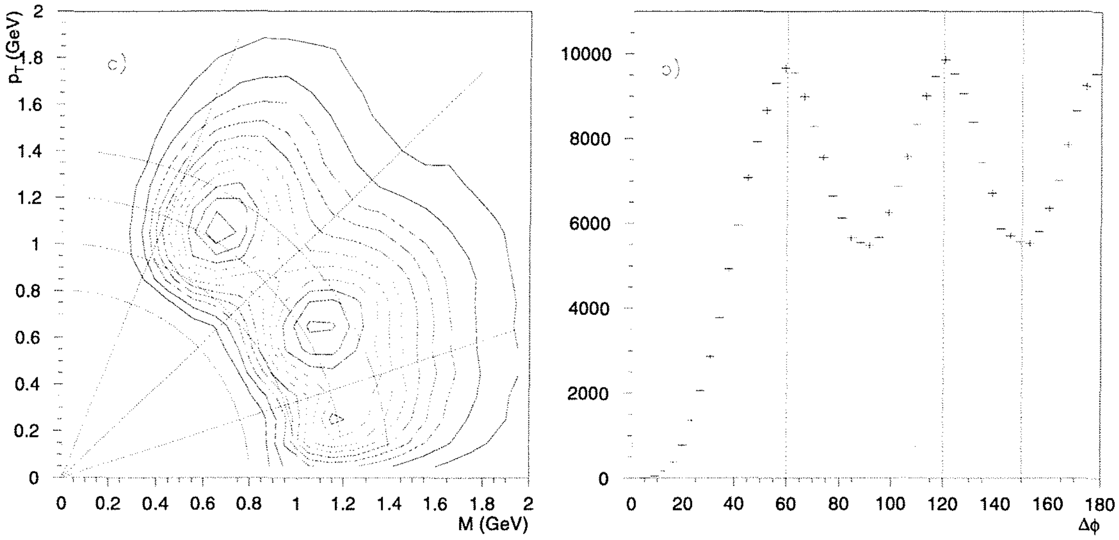

Figure 2-2: Dimuon acceptance in NA50 a) as a function of dimuon transverse momentum p_T and mass M and b) as a function of the polar angle ϕ.

It is clear from this figure that the acceptance depends on m_T and in particular, for a given value of m_T, the acceptance depends on the azimuthal angle difference $\Delta\varphi$ between the two muons. The minima in the plot b) correspond to $\Delta\varphi = 30, 90, 150$ degrees where, due to the presence of the magnet coils, about 30% of the events are rejected.

The standard configuration for the study of J/ψ production, with a current of 7000 A in the toroidal magnet and the absorber made of 420 cm of C and 80 cm of Fe, suppresses the contribution of low mass muon pairs. The corresponding mass resolution $\sigma_M(J/\psi) \approx 105$ MeV is good enough to distinguish the ψ' from the J/ψ. For high momentum muons, as the ones coming from the J/ψ decay, the contribution to the mass resolution from the track angle measurement is less important and a thick absorber can be used. Furthermore, the combinatorial background is negligible for masses above 2.5 GeV.

It is possible to optimise the present NA50 set-up to improve both acceptance and mass resolution for low mass muon pairs. A better performance can be obtained reducing the field in the dimuon spectrometer and reducing the absorber thickness. We have simulated the detector performance in Pb-Pb collisions with 4000 A in the toroidal magnet, and taking away the last 80 cm of iron from the hadron absorber. In this case, we get a reasonable acceptance down to zero p_T, while the mass resolution at the ω is $\sigma_M(\omega) \approx 80$ MeV. It is not possible to further reduce the thickness of the absorber, because that would lead to too many hits in the first chamber of the spectrometer. With such a mass resolution, it is not possible to separate the ρ-ω system, which appears as a single structure.

Also the signal to background ratio (*S/B*) is far from being ideal. In the low mass region, it is $S/B \approx 0.4$ in the peaks of the resonances, while in the intermediate mass region ($1.5 < M_{\mu\mu} < 2.5$), it is of the order of $S/B \approx 0.05$ [2].

2.4 The proposed upgrade

The present NA50 apparatus is an excellent tool for the study of J/ψ production. The high intensity ion beam, together with the very selective trigger, allows studying rare processes (such as J/ψ production) in a reasonable amount of time. The thick absorber plus the high magnetic field in the spectrometer reject most of the low mass muon pairs, enriching the collected event sample of the interesting high mass dimuons. The measurement is also precise due to a good mass resolution and to the absence of combinatorial background.

The situation is different for what concerns low-mass dimuons. The problem is two-fold: the huge combinatorial background (up to masses $M \sim 2$ GeV), and the poor mass resolution in the ρ–ω–φ region. In the case of the low-mass resonances, in fact, the average momentum of the muons is lower with respect to the J/ψ muons. For this reason, they suffer more from multiple scattering in the absorber. As a result, the contribution to the mass resolution from the error on the measurement of the muon angles becomes more important. Moreover, the contribution to the opposite-sign spectrum from meson decays is so large compared to the signal that a small uncertainty in the background subtraction could have a significant impact on the final signal spectrum.

We intend to upgrade the NA50 set-up adding a vertex spectrometer, equipped with a detector of high enough granularity such that it would be possible to measure the hundreds of charged particles produced in Pb-Pb collisions. A track-matching procedure based on the comparison of the momenta and angles as measured before and after the absorber, would allow to select and identify, among all reconstructed tracks in the vertex spectrometer, the muons that gave the trigger.

By measuring the muon tracks before they enter the hadron absorber, the vertex spectrometer enhances the physics performance of the dimuon spectrometer. Since the muon angles are measured before they get blurred by the multiple scattering in the wall, a substantial improvement of the mass resolution is obtained. Moreover, π or K mesons, which decay into muons, seldom satisfy the matching criteria. Therefore, a non-negligible fraction of the combinatorial background is automatically rejected. These features improve the measurement accuracy of dimuon production, in particular at low masses. For the first time it will be possible to study separately the production of ω and ρ mesons from proton-nucleus to Pb-Pb collisions.

Finally, if the position resolution is good enough, one can extrapolate the tracks to the interaction point and measure the track offset, i.e. the distance in the transverse plane between the interaction point and the extrapolated track. In this way, it is possible to select an event sample highly enriched by simultaneous semi-leptonic decays of charmed mesons. The vertex spectrometer would allow clarifying whether the observed excess of dimuons with mass between 1.2 and 2.5 GeV is due to prompt dimuons or to muon pairs, originated from charm decays.

Central Pb-Pb collisions are characterised by high multiplicity. At the same time, it is desirable to run at the highest possible luminosity, in order to collect enough statistics of rare events (for instance open charm decays) in a reasonable amount of time. This environment sets strict requirements on the tracking detector to be used in the vertex spectrometer (and on its data acquisition system). We have already mentioned fine granularity and enhanced spatial resolution, which are needed to separate the hits belonging to the different tracks. Moreover, due to the high event rate, the detector must also be fast in terms of readout and dead time. Finally, the high number of particles per square centimetre not only represents a challenge from the point of view of granularity and spatial resolution, but it also results in a severe radiation dose.

Nowadays a new and fashionable type of detector, the *silicon pixel detector,* is available and matches the above mentioned requirements. A pixel detector is a matrix of finely segmented silicon detectors each of them connected to a readout cell of the same size, containing miniaturised readout electronics. The Ω3/LHC1 pixel system developed by the CERN-RD19 collaboration represented already a suitable detector for our experiment in terms of spatial (pixel size $50 \times 500\ \mu m^2$) and time (minimum strobe 100 ns) resolution. However, we soon discovered that the Ω3/LHC1 readout chip did not have the needed radiation tolerance. We decided then to build a test spectrometer using the available pixel chip, while pursuing the development of a new chip, suitable for the intended experiment.

The test spectrometer was aimed at running in a low intensity beam, so as not to burn the chips, with the purpose of verifying the feasibility of the project. In particular, we wanted to show that indeed the track matching procedure is feasible also in high multiplicity Pb-Pb interactions, and to verify the results of the physics performance simulation (see Chapter 6). The results obtained with the test spectrometer are presented in Chapter 7.

References

[1] T. Matsui and H. Satz, Phys. Lett. B 178 (1986) 116

[2] M.C. Abreu et al. (NA38/NA50 collaborations), "Low mass dimuon production in proton and ion induced interactions at the SPS", Euro. Phys. J. C, in print.

Chapter 3

Silicon Pixel Detectors

3.1 Semiconductors

Semiconductors can be considered as insulators with smaller energy band gap (few eV). Only when T ~ 0 K there are no electrons in the conduction band, hence no conduction is possible. At T > 0 K, there is a finite probability that electrons can be excited into the conduction band due to the non-zero thermal energy. In fact, when an electron goes in conduction band, a hole is left which acts and contributes to the conduction as a positive charge.

Conductivity is also dependent on the impurity concentration. Impurities are called *donors* or *acceptors* if they have one valence electron more or respectively less than the semiconductor atoms. In intrinsic semiconductors, where the number of impurities is negligible compared to the number of electrons in conduction band, the density of thermally generated electrons in conduction band (n) is equal to the density of holes in valence band (p):

$$n = p = n_i \propto \exp\left(-\frac{E_g}{2kT}\right) \qquad (3\text{-}1)$$

In silicon, the intrinsic carrier density n_i is 1.45×10^{10} cm^{-3} at room temperature and the band gap energy E_g is 1.12 eV. The band gap energy varies only slightly with temperature due to thermal expansion of the periodical potential associated with the lattice. It is worth stressing that at cryogenic temperatures the number of intrinsic carriers is exponentially reduced, due to the reduced thermal energy (see Figure 3-1 left).

By introducing acceptors or donors into the lattice, additional holes or electrons are added to the intrinsic charge carriers. Today's electronics relies on well-established techniques to introduce dopant concentrations in order to change and control the device characteristics. For a higher concentration of donors N_D than acceptors N_A the semiconductor is said to be n-type, and the density of electrons n_n as majority carriers and holes p_n as minority carriers is given by:

$$n_n = \tfrac{1}{2}\left(N_D - N_A + \sqrt{(N_D - N_A)^2 + 4n_i^2}\right) \qquad (3\text{-}2)$$

$$p_n = \frac{n_i^2}{n_n} \qquad (3\text{-}3)$$

Similar equations are valid in the case of a p-type material.

When an external electric field is applied, the carriers move towards lower potential energies. As they drift, they are both accelerated and scattered, eventually reaching an average velocity according to the following relation:

$$\vec{v}_{n,p} = \mp\frac{q\tau_{n,p}}{m_{n,p}}\vec{E} = \mp\mu_{n,p}\vec{E} \tag{3-4}$$

where τ is the average time of flight between two consecutive scattering, and μ is the *mobility*. The drift of the carriers gives rise to a current with density:

$$\vec{J} = -qn\vec{v}_n + qp\vec{v}_p = qn\left(\mu_n + \mu_p\right)\vec{E} = \sigma\vec{E} \tag{3-5}$$

In doped semiconductors generally either n or p dominates by several orders of magnitude, hence the conductivity σ, or the resistivity $\rho = 1/\sigma$, can be simplified like the following for n-type (p-type) semiconductors:

$$\sigma = \frac{1}{\rho} = qn\mu_{n,p} \tag{3-6}$$

It is worth stressing that τ increases with decreasing temperature, but this effect is completely overwhelmed by the much more rapid decrease in the density of carriers, as seen from Equation 3-1. Thus, unlike metals, the electrical resistance of semiconductors increases with decreasing temperature.

At the same time, the mobility increases when going to lower temperatures, as shown in Figure 3-1 right, hence same values of the saturated drift velocity can be reached for a drastically reduced voltage compared to room temperature [1].

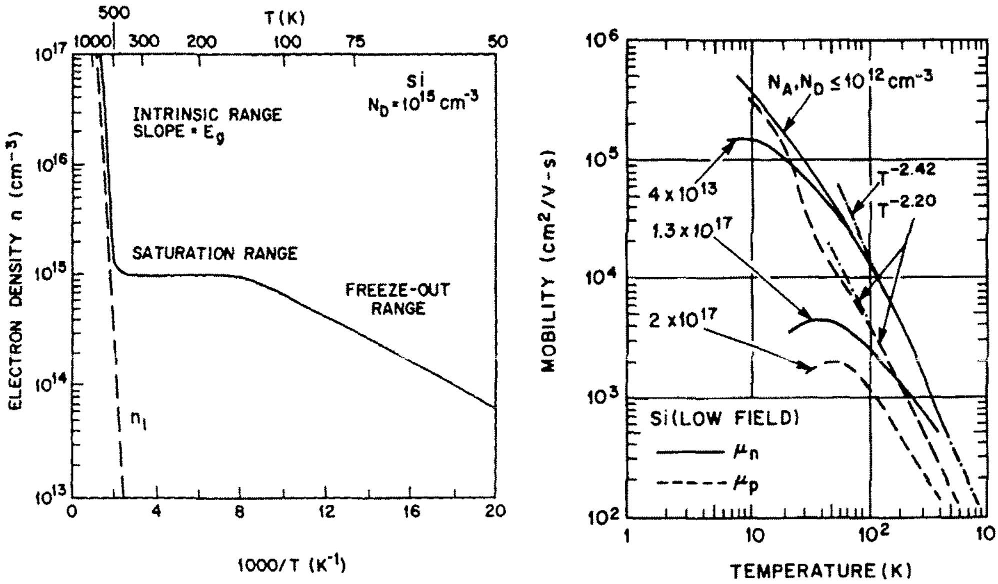

Figure 3-1: Electron density (left) and carriers mobility (right) in silicon as a function of the temperature [1].

3.2 Signal generation in silicon

When a charged particle crosses a piece of semiconductor, it generates electron-hole pairs via ionisation. The charged particle interacts electromagnetically with the lattice electrons and, as a result, electrons are excited from the valence band into the conduction band and the lattice atoms are left ionised. The energy lost by ionisation is described by the experimental formula by Bethe and Bloch [2]. The mean energy loss for particles with $\beta\gamma > 3$ can be considered as constant. Particles with this minimal mean energy loss are called minimum ionising particles (MIPs). All particles used in the experiments described in this thesis can be considered as MIPs.

In collisions in which there is a high-energy transfer, the electrons sometimes are not only excited, but they acquire enough kinetic energy to escape the considered volume. These electrons are called "knock-on electrons" or "delta rays".

A layer of thickness x, for which the mean energy loss is much smaller than the maximum kinetic energy transferred to a free electron in one interaction, is considered *thin*. In thin detectors the probability of interactions with high-energy transfer is strongly reduced. Hence the most probable energy deposition is less than the mean energy deposition and the distribution shows a long tail towards higher energies due to these rare events. Landau established a theory [3] for the energy loss in thin detectors, hence the name Landau distribution for the energy deposition in thin layers. For a 120 GeV pion impinging on silicon, a detector has to be considered as thin if its thickness is less than 12 cm. Thus all the detectors described in this thesis have to be considered as thin.

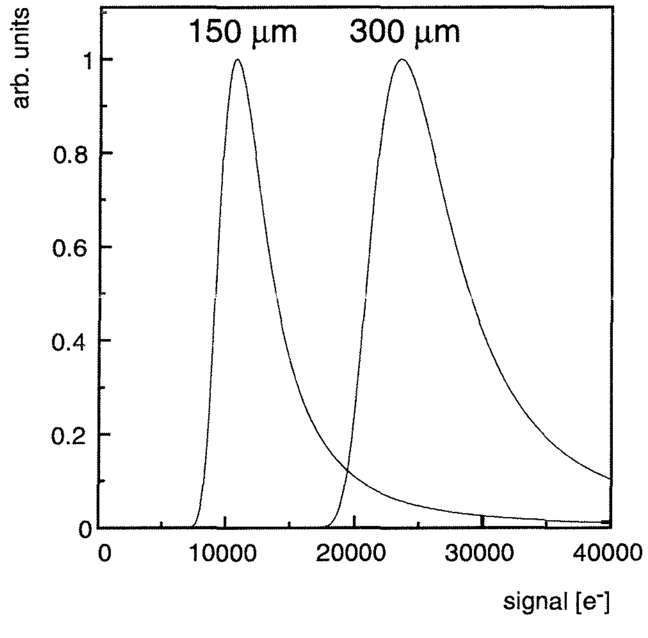

Figure 3-2: Landau distribution for a 300 µm and a 150 µm thick silicon detector.

In silicon, the average energy needed to create an electron hole pair is 3.6 eV. It is possible to compute numerically the Landau distribution for silicon, as shown in Figure

3-2. Most probable values are 11'000 and 24'000 electrons for 150 μm and 300 μm thick silicon detectors respectively.

3.3 Junctions as detectors

Applying a potential difference across a piece of semiconductor would allow collecting the signal generated by a charged particle passing through it. Unfortunately, the band gap of semiconductor like silicon or germanium is small enough that a high permanent current flow would be present. The signal to background ratio of the detector would not be acceptable. Normally a p-n junction (diode) in used instead. In fact, when the diode is operated in reverse bias, the steady state current consists of the diode leakage current, which is largely reduced compared to a homogeneous semiconductor. Furthermore, the charged carriers drift in the depleted region of the diode is fast (tens of ns) compared to diffusion (μs).

In order to compute the electric field and the geometric extension of the depletion region, the Poisson equation must be solved:

$$\vec{\nabla}\vec{E} = \frac{\rho}{\varepsilon_0 \varepsilon_s} = \frac{q}{\varepsilon_0 \varepsilon_s}\left(N_D - N_A + p - n\right) \qquad (3\text{-}7)$$

In the approximation of a one-dimensional abrupt junction, as shown in Figure 3-3, where the carrier concentration p and n are zero outside the depletion region, Equation 3-8 can be simplified like the following:

$$\frac{dE_y}{dy} = \begin{cases} -\dfrac{q}{\varepsilon_0 \varepsilon_s} N_A & -y_p \le y \le 0 \\ \dfrac{q}{\varepsilon_0 \varepsilon_s} N_D & 0 < y \le y_n \end{cases} \qquad (3\text{-}8)$$

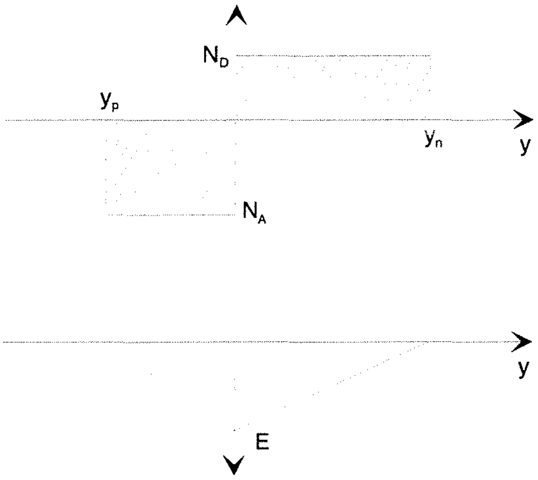

Figure 3-3: Schematic representation of an abrupt junction. The upper figure shows the impurity concentration, the lower the electric field.

The electric field is thus:

$$E_y = \begin{cases} -\dfrac{q}{\varepsilon_0\varepsilon_s} N_A(y+y_p) & -y_p \le y \le 0 \\ \dfrac{q}{\varepsilon_0\varepsilon_s} N_D(y-y_n) & 0 < y \le y_n \end{cases} \tag{3-9}$$

Integrating these expressions over the entire space charge region, and taking into account charge neutrality ($N_A y_p = N_D y_n$), one gets the potential difference across the junction:

$$V = \frac{q}{2\varepsilon_0\varepsilon_s} N_A y_p{}^2 + \frac{q}{2\varepsilon_0\varepsilon_s} N_D y_n{}^2 = \frac{q}{2\varepsilon_0\varepsilon_s} N_D y_n \left(y_p + y_n\right) \tag{3-10}$$

It is worth reminding that the charge Q collected at the junction electrodes is the image of the charge q travelling through the detector. Gatti theorem [4] states that, also in presence of a fixed space charge region, the charge Q induced by a charge q in motion between two parallel plane electrodes at a distance d from one other is:

$$Q = q\frac{\Delta x}{d} \tag{3-11}$$

where Δx is the distance travelled by q in the direction perpendicular to the electrodes.

For this reason, in detector applications, one tries to extend the depletion region over the entire device thickness, with a very small non-depleted region around the contacts. The impurity concentration on the surface region should therefore be much higher than that one in the bulk material. In standard detectors with a p-implant on n-bulk, this means $N_D >> N_A$ and therefore $y_n >> y_p$, i.e. the depletion region extends mainly into the n-region.

Defining the device thickness as d, Equation 3-11 can be simplified as the following:

$$V \approx \frac{q}{2\varepsilon_0\varepsilon_s} N_D d^2 \tag{3-12}$$

For a 300 μm thick silicon detector with an impurity concentration of 10^{12} cm^{-3}, the depletion voltage, which is the voltage at which the detector is fully depleted, is ~ 70 V (at room temperature).

3.4 Brief overview of silicon detectors

Silicon detectors generally consist of one or two-dimensional arrays of detection elements, i.e. p-n junctions. Already in the 60's, arrays of discrete silicon diodes for light detection were developed. Such arrays with individual signal processing circuits were proposed as tracking detectors, but they were abandoned as impractical in comparison with the newly developed bubble and wire chambers.

Pad detectors are a further development of that idea, in which a number of detection diodes are implemented adjacently on one common substrate. This became possible thanks to the improvements achieved in the processing of silicon for detector applications. Each diode is typically several millimetres square in size and it is connected to its individual signal processing circuit, which is outside of the detector, via metal lines deposited on top of the detector substrate (see Figure 3-4 left). The implementation of all diodes on the same substrate results in a hermetic sensitive area.

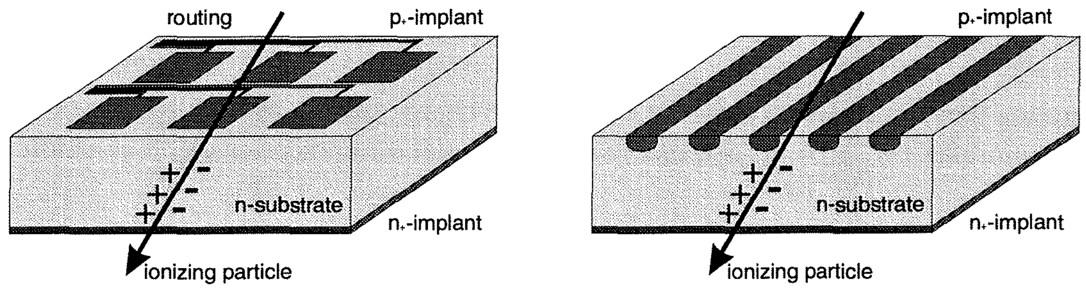

Figure 3-4: Schematic views of (left) a pad detector, and (right) a mictrostrip detector.

In microstrip detectors (Figure 3-4 right), a few tens of micron wide strips are deposited on a common substrate. These strips can be several centimetres long. Various readout schemes (analog or digital) have been successfully applied. Depending on the precise geometry of the strips and signal processing, spatial resolution as good as ~5 μm (in one dimension) can be achieved. It is possible to have two dimensional position information, simply mounting two microstrip detectors rotated 90 degrees with respect to each other. In general, only single tracks are unambiguously reconstructed. For N tracks, there are N^2 possible combinations of hits in a x-y plane. Combining several planes rotated at different angles with respect to each other, and using pattern recognition algorithms, it is possible to resolve the ambiguities up to a certain limit.

Also double-sided microstrip detectors are available. In this case, both sides of the detector bulk are segmented. Normally, n-type substrates are used, with p-strips on one side and orthogonal n^+ strips on the other. Special care has to be taken in separating the n^+ strips, in order to focalise the signal on the electrodes and obtain the wanted position resolution. The separation can be obtained using blocking p^+ electrodes in between the n^+ strips or field plates over the strips, which create a field that repels the electrons.

Silicon drift detectors are based on a different principle with respect to what has been describes so far. Parallel p^+ strips are deposited on both sides of the n-substrate, as depicted in Figure 3-5. On one side of the detector, n^+ implants act as collection electrodes. A dedicated biasing scheme of the implants on both sides creates a drift channel in the wafer, such that the negative carriers first move towards the middle of the substrate, and afterwards towards the n^+ electrodes.

This type of detector provides two-dimensional information. The first coordinate is given by the hole signal on the strips. The second is given by the time between the particle passage and the arrival of the electrons at the collection electrodes. Spatial resolution of ~5 μm can be achieved.

Since the drift velocity depends strongly on temperature, the device has to be calibrated and then operated at a constant temperature. Due to the collection time, silicon drifts are suited for applications in low-rate experiments.

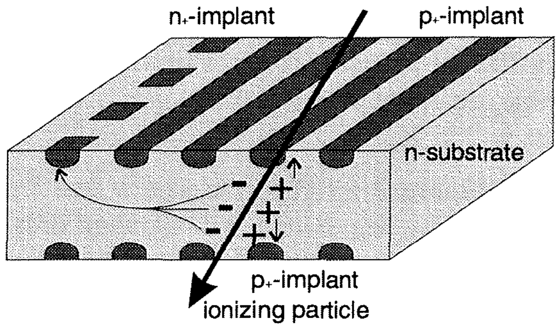

Figure 3-5: Schematic view of a drift detector.

3.5 Active pixel detectors

A pixel detector is an array of very small p-n junctions providing true bidimensional information. The size of the sensing cell varies from 50 to 500 μm. Each pixel is directly connected to its own miniaturised readout electronics and signal-processing unit. The small pixel represents a low capacitance load for the front-end readout electronics. Therefore, the noise produced by the detecting element is small compared to a microstrip detector, allowing a stable operation even with lower amplitude signals. Due to the short drift path of the carriers to the collection electrode, the system speed and timing precision is mainly limited by the readout electronics. This makes pixel detectors a useful instrument in experiments with high multiplicity and high event rate.

The array of sensors and readout cells can be processed on the same substrate (*monolithic pixel detectors*) or on different wafers, which are then connected together at a later stage (*hybrid pixel detectors*). In a monolithic pixel detector, the readout electronics is sitting in n-wells placed next to collection electrodes (see Figure 3-6 left). These wells have two purposes. First, they shield the detection volume from the readout electronics. This avoids that switching transistors induce a fake hit in the collection electrode. Moreover, the presence of the n-wells in the substrate modifies the field lines, such that the carriers generated by ionisation drift towards the collection electrodes.

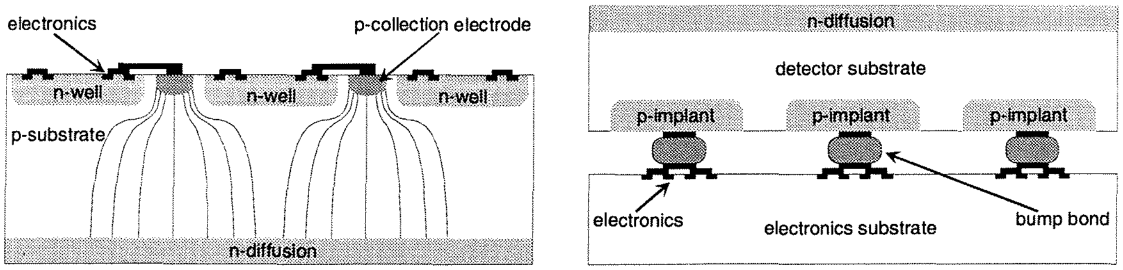

Figure 3-6: Left: cross sectional view of a monolithic pixel detector, showing the field lines that guide the carriers to the collection electrode. Right: cross sectional view of a hybrid pixel detector, showing the bump bonding between the sensor arrays (top) and the readout chip (bottom).

A fully functional monolithic pixel detector with 300 channels of size 34×125 μm^2 has been produced using only PMOS electronics [5]. Even if the detector principle has been shown to work, monolithic pixel detectors are not used, because they relies on non-conventional technologies, which lead to low production yield and high cost.

In the hybrid approach (see Figure 3-6 right), the sensor and the electronics arrays are produced independently, and they are connected together only at a later stage. This allows flexibility in the choice of material and fabrication processes for both detector components. One can use different sensing materials connected to the same readout chip, which in turn can be independently developed and optimised. The connection between the detector and the readout electronics is realised via flip-chip bonding, where small bumps of solder establish the electrical and mechanical connection between each detector pixel and its own readout cell.

3.6 The Ω3/LHC1 pixel detector

The pixel detector system used to build the test vertex spectrometer described in Chapter 7, was the Ω3/LHC1, developed by the CERN-RD19 collaboration and used in the WA97 [6] and NA57 [7] experiments. It is a hybrid pixel detector. In the following sections the readout chip and the sensor array are described in detail.

3.6.1 The readout chip

The Ω3/LHC1 readout chip is an array of 16×128 readout cells, manufactured in 1 μm commercial CMOS technology. The pixel size is 50×500 μm^2. It provides binary information. A photograph of the full chip is shown in Figure 3-7.

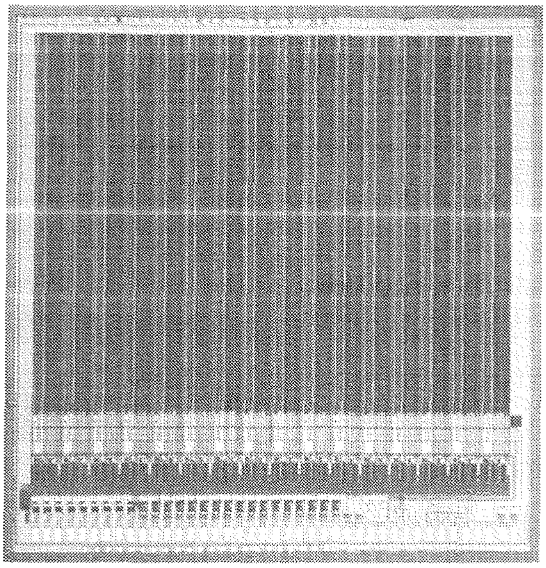

Figure 3-7: Photograph of the readout chip. At the bottom, the two rows of bonding pads for the wire bond connections of data and bias lines are visible.

Figure 3-8 shows a photograph (top) and the schematic (bottom) of a single readout cell. The signal from the detector is fed into a charge amplifier, whose gain is set externally through a bias current (I_{bias}). The signal rise-time is designed to be approximately 80 ns. It is also possible to inject a test pulse (through a test capacitor C_{test}) in order to check the performance of each pixel cell without the detector being bonded. This test signal is enabled by a *test* flip-flop. After the amplification stage, the signal goes to a comparator and, if it is higher than the externally pre-set threshold (I_{th}), to a shaper. The digitised signal travels through a delay line, before reaching the coincidence logic. A logic "one" is written into the memory flip-flop if, during the externally provided strobe, a rising edge is detected at the end of the delay line.

In each cell there is also a *mask* flip-flop after the comparator, which allows switch off the noisy channels. The comparator provides an additional *fast-OR* output. The fast-OR outputs of all pixels in the same column are connected together in a wired-OR configuration, providing a fast signal that may be used for trigger purposes. A *leakage current compensation* circuit (not shown in the figure) serves to compensate the detector leakage current, which would, if high, deteriorate the front-end performances. The level of the compensation can be adjusted externally through a bias current (I_{comp}).

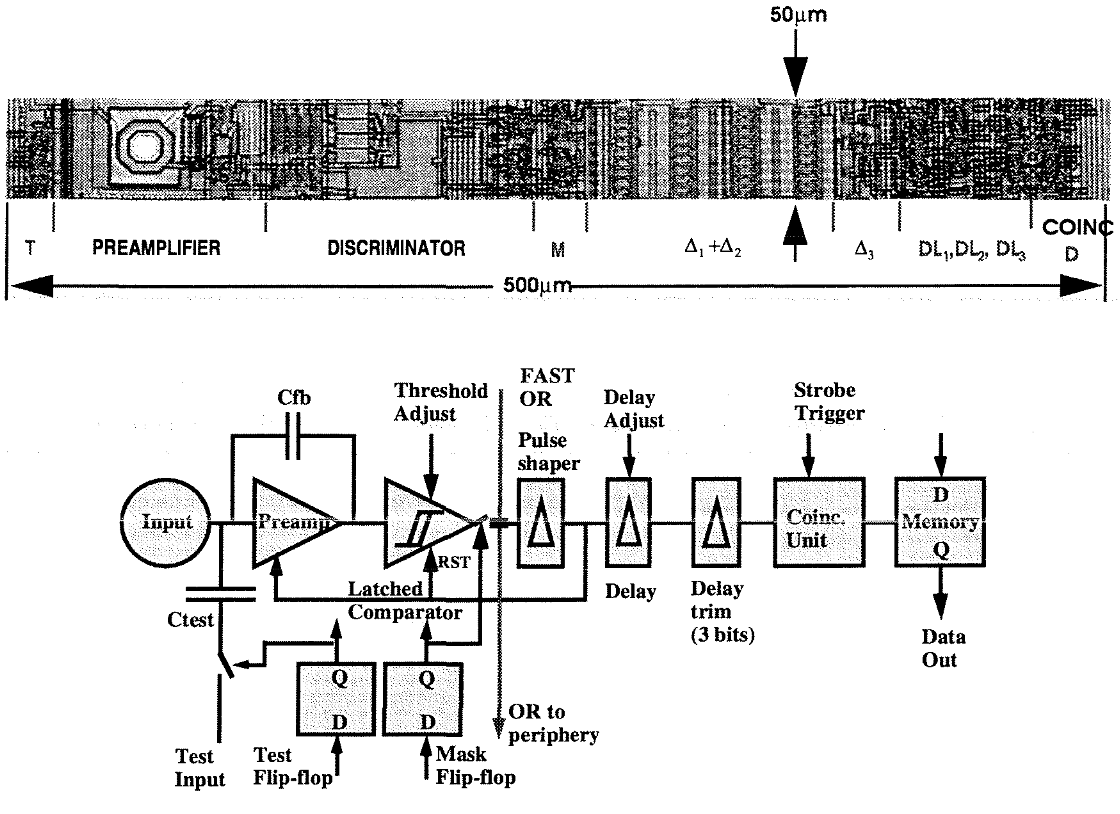

Figure 3-8: Photograph (top) and block diagram (bottom) of the signal processing chain in each pixel cell.

The delay chain, shown in Figure 3-9 left, consists of 36 stages of *current-deprived* inverters. The delay of one stage depends on the value of the externally set I_{dl}. After the fourth stage, a feed back line provides the reset to the front-end. This feature decreases the dead time of the cell to below ~250 ns, even in the case of large signal events. The reset signal can be also provided externally.

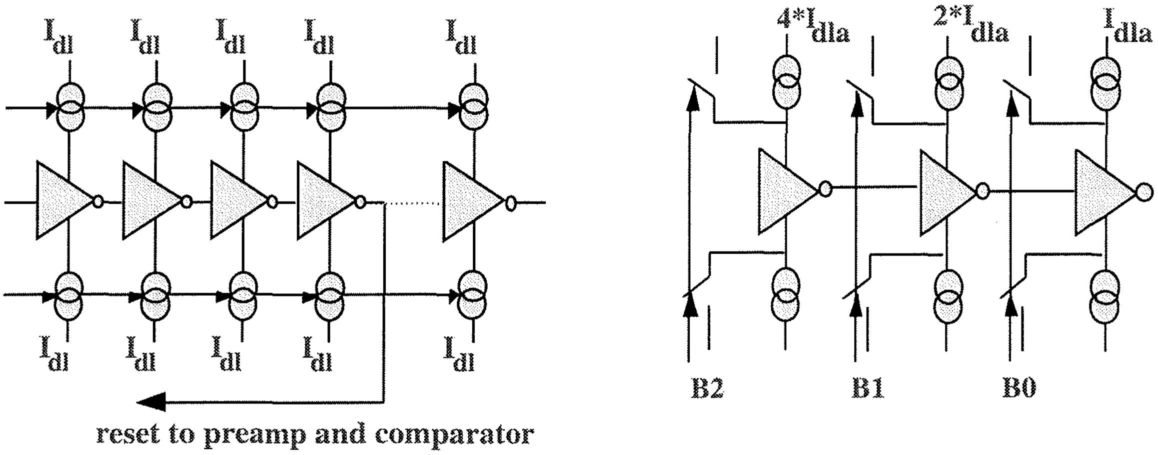

Figure 3-9: The main delay chain (left) consists of 36 inverter stages. After the fourth stage the signal is fed back to reset the preamplifier and comparator. I_{dl} determines the delay of a single stage. The 3 bit delay adjust stage (right) is based on inverters which can be made current deprived or not by a switch across the current source. I_{dla} determines the range of the adjustment.

In order to correct for the time spread from pixel to pixel, an individual 3-bit digitally controlled delay tuning has been added. This trimming delay contains 3 more inverter stages, which can be made current-deprived or not by a switch across the current source (see Figure 3-9 right). A fourth inverter is used to restore a proper edge of the signal to be feed to the subsequent coincidence logic. The quantum of delay added per bit depends on the value of I_{dla}.

The row at the top of the chip is a test row, where all the pixels are always connected to the test input. The peripheral control electronics is placed only at the bottom side of the chip allowing to put several chips side by side in ladder configuration (see Section 3.6.3). The five biases (I_{bias}, I_{th}., I_{comp}, I_{dl}., and I_{dla}.), that are common to all pixels in a chip, are regenerated here for each column.

During data taking, the strobe generated by the trigger is connected to all pixels. If a hit of sufficient amplitude has been sensed in one of the pixels within the strobe width, the data flip-flop of that pixel will be set to logic "one". The data flip-flops of all pixels in one column are configured as a shift-register. The readout requires 128 clock pulses (at ~3 MHz) to shift out the rows of data. In zero suppression mode, the 32-bits word corresponding to a row where at least one column was hit is associated to the row address.

3.6.2 The sensor

Two different types of sensor were designed: a *single-chip* sensor produced mainly for device characterisation and test purposes, and a *ladder* sensor, to be bonded to 6 readout chips for applications in experiments. The single-chip sensor is a matrix of 16×128 diodes surrounded by a guard-ring. The individual pixel measures 50×500 µm^2, matching the size of the readout cell. The guard-ring is connected to ground through the readout chip. Its total sensitive area is 8×6.4 mm^2.

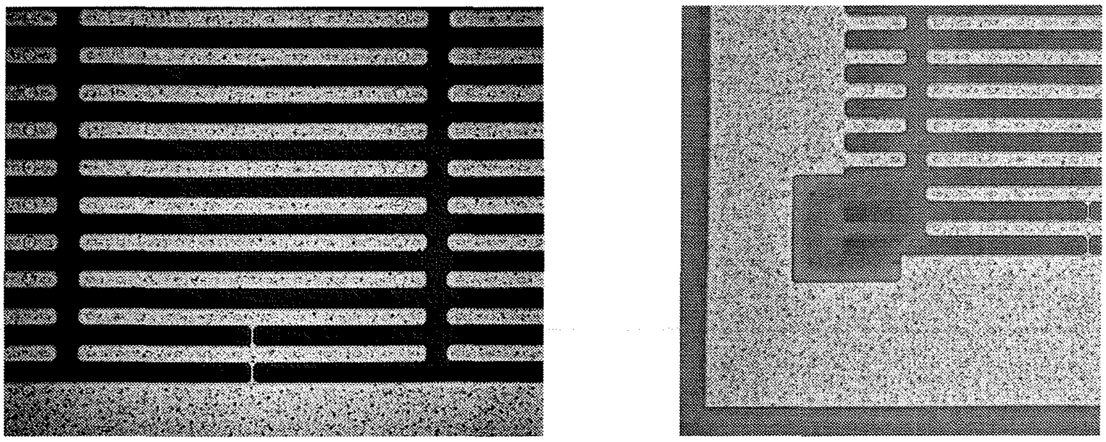

Figure 3-10 Left: photograph of the lower part of a single-chip sensor. The 2 lowermost cells are connected to the guard-ring. The opening in the passivation layer for the bump bonding connection is visible on the right side of each cell. Right: picture of the left-bottom corner of a single-chip sensor. The guard-ring on the sides resembles the actual cells to ensure a homogeneous electric field also for the outermost active cells.

Figure 3-10 left shows a photograph of a single-chip sensor. The diode implant covers a large fraction of the cell area (20×470 µm^2). The edges of the implant and of the metal layer are rounded to avoid too high electric fields at the corners. The 10 µm opening in the otherwise continuous passivation provides the contact for the solder bump. The two lowermost (as well as the two not shown uppermost) cells in a column are dummy cells connected to the guard-ring. This helps to create a homogeneous electric field along the whole sensitive area. For the same reason the guard-ring at the left and at the right also mimics the shape of the basic cell, as shown in Figure 3-10 right.

A ladder is bonded to 6 readout chips, thus comprising 128 rows and 96 columns. In order to cover the dead area existing between two adjacent readout chips, the detecting pixels in the stitching regions measure 50 × 1000 µm^2. As for the single chip, the sensitive area (53 × 6.4 mm^2) is surrounded by a guard-ring.

The sensors were produced on a 300 µm thick high resistivity (17.5 kΩ·cm) silicon substrate. The diodes are p$^+$-implants created by ion-implantation, entirely covered by a metal layer. A passivation layer covers the whole detector, except where the connection to the readout chip is foreseen. The guard-ring is a 500 µm wide diode surrounding the matrix of detecting diodes. It protects the active matrix from influences of defects (cracks) introduced when cutting the sensor chips out of the production wafer. A photograph of a sensor wafer is shown in Figure 3-11, where the single-chips and ladders can be distinguished.

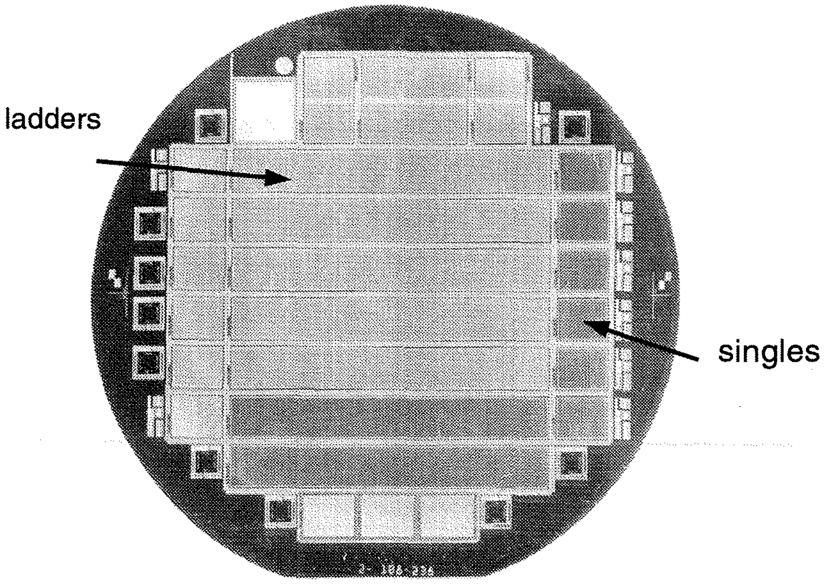

Figure 3-11: Photograph of the 4" wafer. The central region contains 7, surrounded by 6 single detectors on each side. Test structures for other projects fill the rest of the wafer.

3.6.3 Bump bonding and assembling

The electrical and mechanical connection between the detector and the readout chip is established by solder balls, in a so-called *flip-chip* solder bonding process. For the Ω3/LHC1 a fine-pitch solder bump technology developed by GEC-Marconi Ltd has been chosen [8]. The 50 μm pixel pitch constraints the bump to have a diameter ≤ 30 μm. While bumps of larger sizes are normally used in commercial applications and therefore the technology is developed and reliable, the needed process is not yet stabilised. This corresponded to periods of high production yield, alternated to periods in which the number of successfully bonded chips was low.

The various steps of the bump-bonding procedure are shown in Figure 3-12. Both the wafers of readout and sensor chips are delivered with openings in the passivation layer where a bond is foreseen (1). In the following step (2), a photo-resist layer is deposited by photolithography (on the whole wafer) according to a mask, which defines the 22 μm diameter octagonal solder pads where the wettable metal (Cr-Cu-Au alloy) should be present. In step (3), the wettable metal is deposited and then it is taken away via lift-off technique, except where no photo-resist was deposited. This represents the final step for the sensor wafers, before being diced into single-chips and ladders. Photolithography and lift-off techniques are again employed on the readout chips wafer to deposit the soldering on the solder pads (4 and 5). In step (6), the wafer is heated up in such a way that the solder retracts to the wettable metal pads, forming hemispherical bumps. Finally, the readout wafer is diced into chips, which are individually tested.

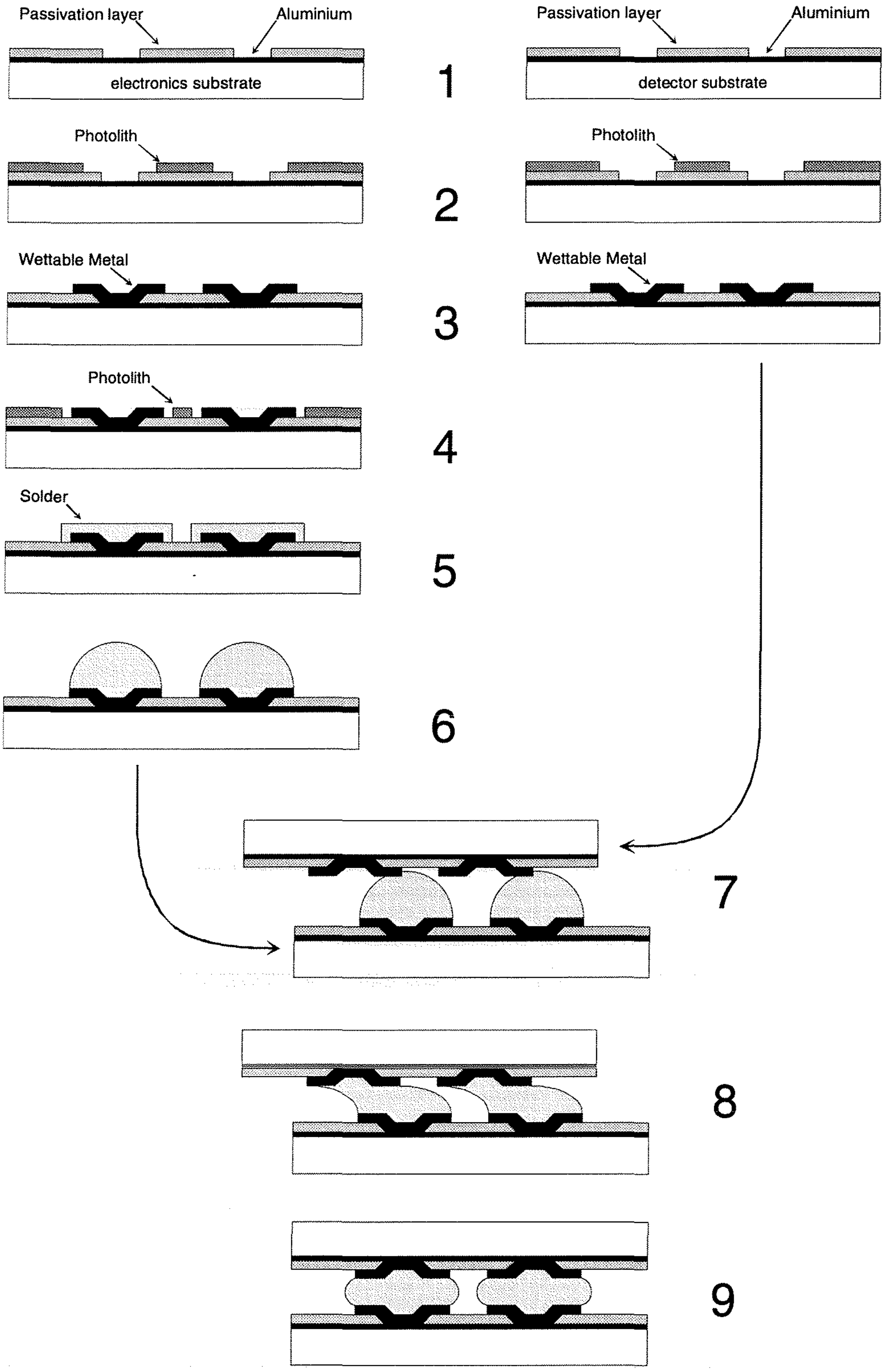

Figure 3-12: The flip-chip solder bonding process. The individual steps are described in the text.

The functioning readout chips are pre-aligned with respected to the flipped sensor (7). The assembly is then warmed up in an oven above the eutectic temperature of the solder (183°C), such that the solder fuse (8). The surface tensions pull the chips into the final aligned position (9), within a 1 μm accuracy. The bump height is ~15 μm.

The successfully bonded detectors are then selected for the assembling of the pixel planes to be used in the experiment. In the following we describe the assembling designed and optimised for the WA97 and NA57 experiments, for which Ω3/LHC1 pixel detector was initially developed. For the test pixel spectrometer that we have built, we introduced several modifications, which will be described in detail in Chapter 7.

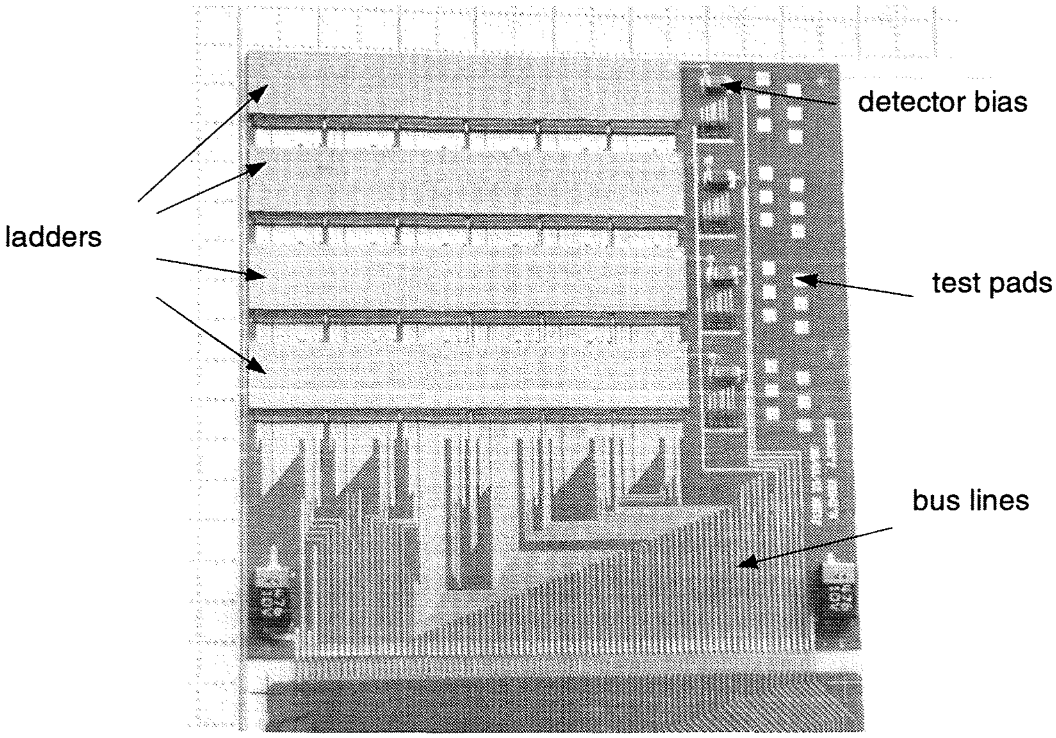

Figure 3-13: An assembled half plane consisting of 4 ladders, each of which is connected to 6 readout chips. It contains nearly 50'000 pixels. Two of such arrays, vertically staggered, cover an active area of ~5 × 5 cm^2

Four 6-chip ladders are glued onto a multi-layer ceramic support, which also contains the bus lines that connect each chip to the external readout electronics. The bulk of this ceramic is made of Al_2O_3, which has dilation coefficient close to that of silicon, and good thermal conductivity. The bus consists of the detector bias, power supplies, chip biases, data lines and readout control signals. The readout chips are connected to these lines via wire bonding. Figure 3-13 shows a photograph of such an assembly, called *array* or *half-plane*. In fact, two arrays are mounted face to face and shifted vertically of almost the size of a ladder in order to have continuous coverage of the solid angle. The small partial overlap of ladders in the two arrays forming one physical plane is needed for alignment purposes. This configuration allows to have a total hermetic sensitive area of 53×50 mm^2 with about 100'000 pixels.

Since it is not possible to mount any connector on the multi-layer ceramic, a *kapton cable* provides the interface between the array and the external readout electronics. On the kapton cable are also mounted passive components, as decoupling capacitors and the resistors that define the bias currents for the pixel chips. The connection of the bus lines from the ceramic to the kapton is realised via wire bonding. In order to ensure robustness to the full system, the multi-layer ceramic and the part of the kapton closest to it are glued onto a common *support ceramic.*

Each pixel array is read out by a VME card, to which it is connected via a (up to 60 m long) twisted pair cable. The zero suppression and address encoding are performed on an intermediate card, the *motherboard,* which is connected directly to the kapton. The motherboard also provides the power to the pixel chips and the detector bias.

3.6.4 Electrical measurements.

The individual test input, together whit the test and mask flip-flops present in each pixel, are extensively used in all the characterisation steps of the detector, and in the preparation before their use in the experiment. A detailed description of the different types of test and their procedure can be found in Section 7.1, when we will speak about the building of the test pixel vertex spectrometer. In the following, we concentrate on the results about the measured detector performance.

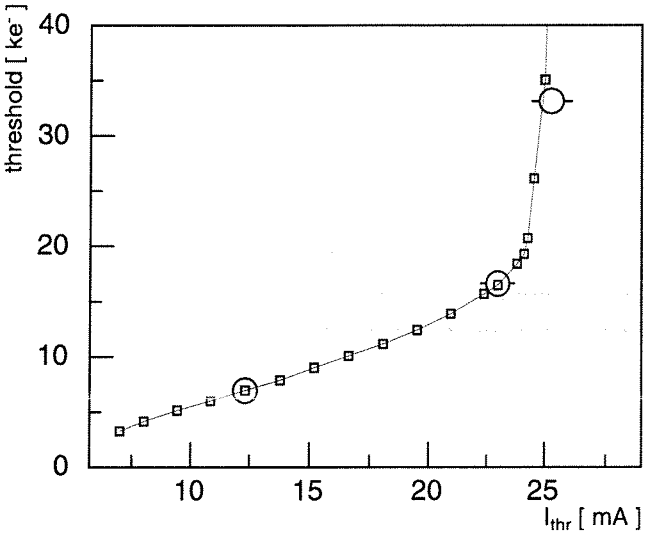

Figure 3-14: Threshold calibration performed by source (circles) and electrical measurements (squares). The threshold shows a linear dependence on the setting current up to ~15'000 electrons.

It is important to know which is the actual pixel threshold in number of electrons for a given value of the set threshold (I_{th}). This calibration is performed injecting in the pixel test input a pulse of known amplitude V_{in}. If the input capacitance is C_{in}, a charge $Q_{in} = V_{in}/C_{in}$ has been injected into the pixel front-end. For a given value of I_{th}, the input pulse is varied. The actual threshold is the charge for which the counting rate of the pixel drops to zero. This scanning procedure is repeated for the whole range of possible I_{th}, and the curve of Figure 3-14 (open squares) is obtained. The error in this measurement is dominated by the systematic uncertainty on the input capacitance, which is of the order of 10%. The open circles in the figure are measurements determined with radioactive sources (described in the next section) that confirm the results obtained with the test pulse. One clearly sees that the threshold varies linearly between 3'000 and 15'000 electrons. Beyond this value, the discriminator is still functional, but the threshold sensitivity to I_{th} increases too rapidly. We also measured the threshold uniformity along the chip. A threshold distribution with a variance of approximately 700 e^- rms for a setting of 16'500 e^- was obtained.

The global delay, common to all pixels in one array, can be adjusted via the delay control current (I_{dl}) between 1.5 and 3.3 μs (as shown in Figure 3-15), according to the trigger latency time of the experiment.

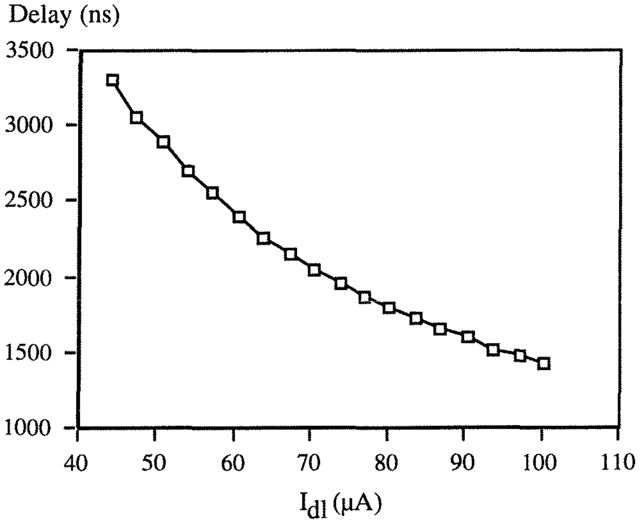

Figure 3-15: Delay of a single pixel as a function of the delay control current I_{dl}. The delay can be set between 1500 ns and 3300 ns.

The left plot of Figure 3-16 shows the internal delay of all the 2048 pixels of a readout chip as a function of the row number, before the individual delay is adjusted. These data were taken injecting a test pulse in each single pixel and measuring for which value of the strobe delay the count rate was 100%. A non-uniformity in the time response from pixel to pixel of the order of ~200 ns was measured. One can also notice that the time response depends on the position of the pixel in the chip, with a clear top-down effect. The response time can vary from pixel to pixel and from event to event because of (i) the collection time of the detector, (ii) the time-walk and (iii) the difference in the internal delay of the readout cells. The first cause is practically negligible in the case of this detector. The time-walk is discussed below. The main contribution is clearly related to the difference in the internal delay of the cells, which also causes the top-down effect, because of a gradient of the control current I_{dl} along the columns.

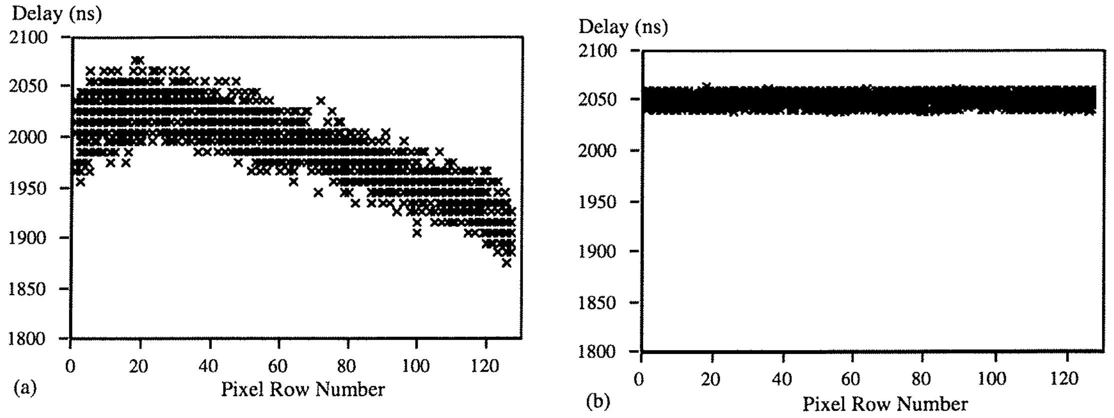

Figure 3-16: Internal delay of the 2048 pixels in one chip as a function of the row number before (left) and after (right) delay adjust. Before adjusting, not only there is a considerably larger time spread, but also a top-down effect is visible.

The non-uniformity in time response can be corrected using the individual 3-bit delay adjust present in each cell. One first measures, for all pixels in the chip, the pixels time response for the eight possible value of the delay adjust settings. For each pixel, the setting that minimises the time difference with respect to the global common delay is taken as adjust setting. The delay-adjust control current (I_{dla}) can be varied so to change the amount of delay added per bit, thus optimising the adjusting procedure. The right plot of Figure 3-16 shows the result after the adjustment. All pixels respond within a time window of 25 ns, indicating a timing precision of less than 6 ns rms.

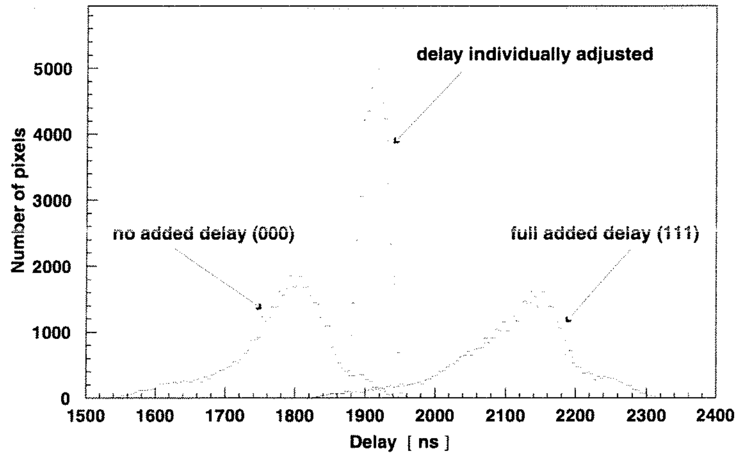

Figure 3-17: Distribution of the internal delays for 50'000 pixels of a half plane. The distributions for all adjust bits set to 0, all adjust bits set to 1 and for individually adjusted delays are shown.

The result obtained with the delay adjust procedure for a complete array of nearly 50'000 channels is shown in Figure 3-17. In this case, not only the pixel to pixel, but also the chip to chip variation has to be corrected. That is why the time spread before adjusting is of the order of 450 ns, and it reaches at the best ~70 ns after adjusting.

Another important parameter, which characterises the detector performance, is the time-walk. Signals of different amplitude generated in the detector may switch the front-end electronics at different time, depending on when the comparator threshold has been hit. This is a major concern in high event-rate experiments, where hits in different pixels but belonging to the same event have to be exactly correlated. Figure 3-18 shows the time-walk of a single cell. For input charges above 9000 electrons (which is always the case for a MIP), and a threshold of 5000 electrons, the added response time was less than 10 ns.

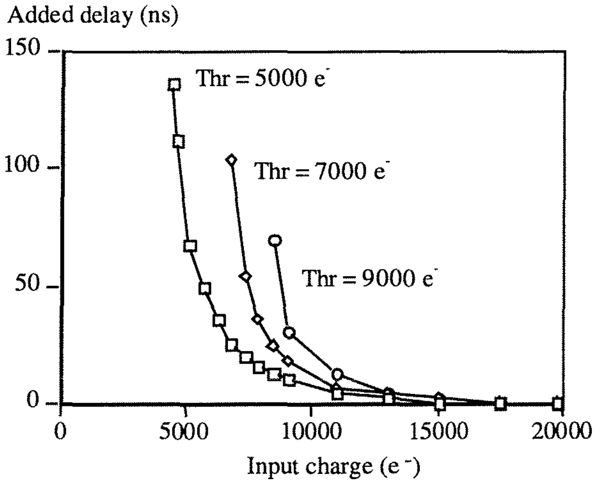

Figure 3-18: Added response time of a pixel cell due to time-walk in the discriminator for different threshold settings.

3.6.5 Measurements with radioactive source

Radioactive sources are used to calibrate the pixel threshold. This is done exposing a pixel detector (in this case a single-chip device) to radioactive sources of well-defined photon emission lines. For our calibration, we have used: ^{109}Cd (22 keV and 25 keV), ^{241}Am (60 keV) and ^{57}Co (122 keV). A threshold scan is performed varying the threshold current I_{th} of the chip and recording the number of photon counted (i.e. the number of hits registered) for every pixel. When the set threshold exceeds the characteristic photon energy, the counting rate drops dramatically to zero. This point represents a unique correspondence between the value of the threshold setting and its actual value in number of electrons. The different calibration points are superimposed to the data collected with the test pulse in Figure 3-14.

Measurements with radioactive source are also used to check the actual connection of the bump bonding between the sensor and the readout chip(s). This allows rejecting detectors with large regions of faulty bonds. For this kind of test, a beta source (^{90}Sr) is normally used to better simulate the response to minimum ionising particles. Figure 3-19 shows the response of a half plane of 50'000 channels to this source. The profile of the source, positioned left of and below the centre, is clearly visible, as well as the small fraction of faulty bonds (white pixels). Two columns were noisy and had to be masked.

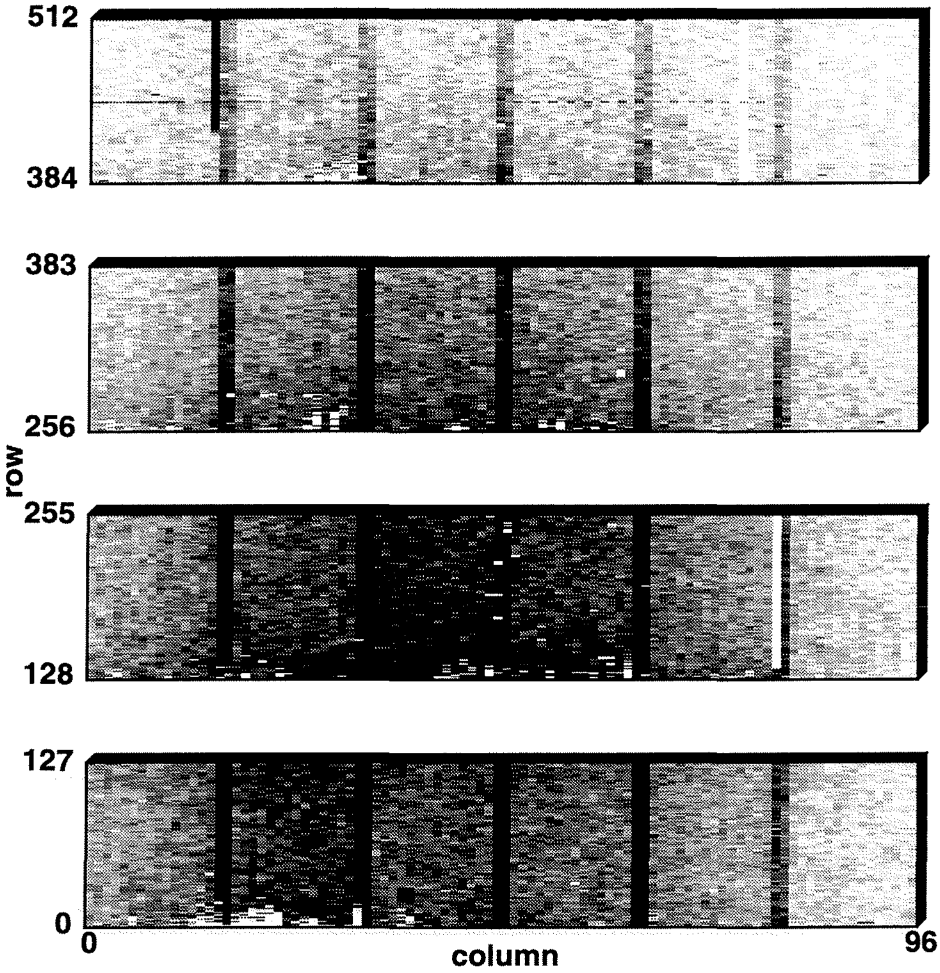

Figure 3-19: Response of an array (~50'000 pixels) exposed to a ^{90}*Sr source. The histogram is grey scale coded, with white bins having no entries and black bins having about 30 entries. The columns with nearly twice as many entries as their neighbours are the columns with larger size pixels in the stitching regions between two readout chips.*

3.6.6 Measurements with beam particles

Both single-chip detectors and half planes were tested in the CERN-SPS 120 GeV pion beam. The aim was to measure the detector performances in terms of absolute efficiency, position resolution and timing in a real environment. A silicon microstrip telescope was used to reconstruct the tracks. The pixel detector to be investigated was placed in the middle of the telescope in order to have the best possible position resolution from the track extrapolation. The trigger signal was provided by two scintillators placed one upstream and the other downstream of the telescope. A third small scintillator (2×1 mm^2) was used to select tracks passing through specific regions of the pixel detector that was tested.

Figure 3-20 shows the diagrams concerning the strobe timing in measurements with beam particles. The top diagram represents the signals of the hit pixels spread over a time interval that depends on the delay adjust. The readout is started by the strobe signal (second top diagram), which has a certain delay with respect to the physics trigger and a certain width. Full efficiency is reached when the strobe delay is perfectly timed with the pixel response and when its width comprises all the hit pixel signals. This is not the case when the strobe delay is too early or too late (diagrams 3 and 4 from the top).

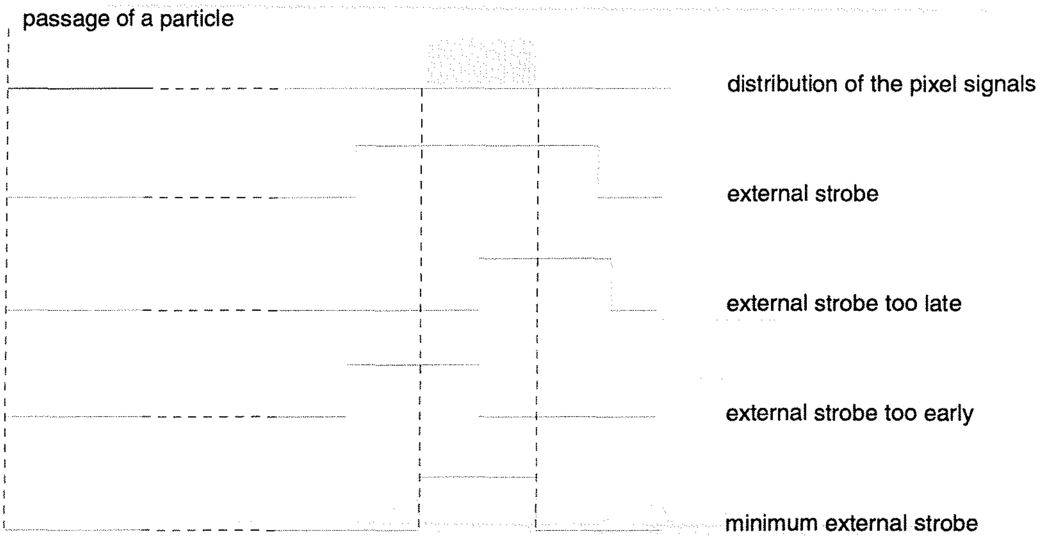

Figure 3-20: Timing diagram for measurements with beam particles.

In order to minimise pile-up one should apply the minimum possible strobe width, which contains all the hit pixels. This width can be determined via the following procedure. First, a reasonable large strobe width is set and a delay scan is performed, till the efficiency plateau is found. Since the strobe width is large, it is sure that all the hit pixels are read out and the efficiency shall reach 100%. The event rate, and therefore the beam intensity, must be such that pile-up is negligible. The delay scan is then repeated with narrower strobe widths, till the smallest value for which 100% efficiency can be reached is found. This procedure can be speed-up considerably if a careful delay adjust is performed in the laboratory with a test pulse. In this case, the minimum possible strobe width is already known and only the relative delay with respect to the trigger must be determined.

Figure 3-21 shows the delay scan of a single-chip detector obtained with a strobe width of 45 ns. The two curves represents the same detector, with and without loading the 3-bit delay adjust in the pixels as determined via the measurement with the test pulse. As long as the strobe arrives earlier or later with respect to the pixel response, only a fraction of the hits is recorded (rising and falling edges of the curves, respectively). When the strobe is in time with the pixel signals, and the delay registers are loaded with the appropriate bit pattern, the full efficiency plateau is reached. The long tail towards later delays is due to hits in which the charge is shared among several pixels and the lower amplitude signals are switching the comparator at a later time.

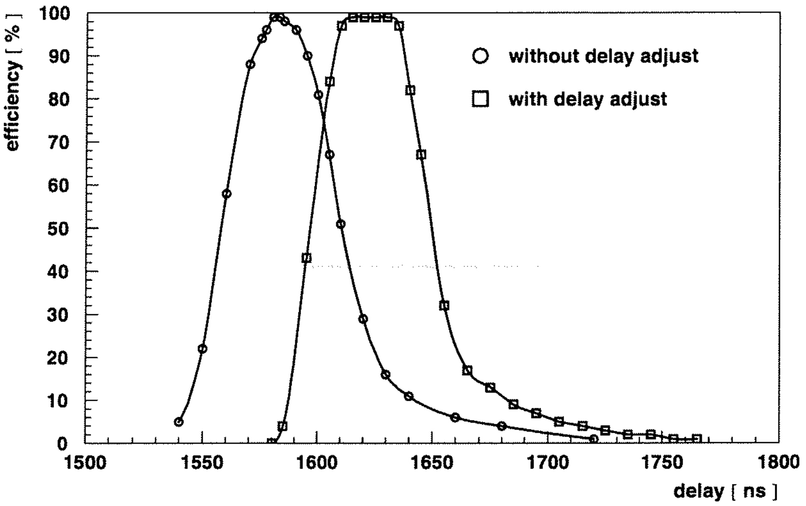

Figure 3-21: Efficiency as a function of the strobe delay for a strobe width of 45 ns, with and without delay adjust. The threshold was set to ~5000 e⁻.

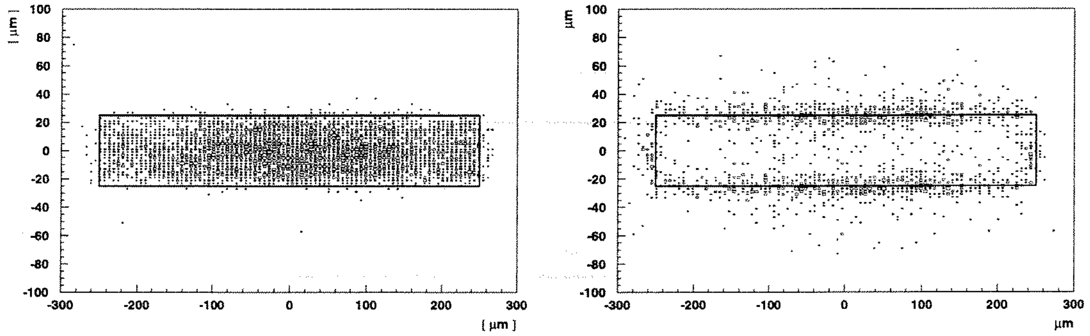

Figure 3-22: Position of tracks producing (left) single hits and (right) double hits within a pixel, the dimensions of which are indicated by the large box. The histogram is box coded, with the size of the box proportional to the number of entries. The plot is not to scale.

The position resolution was determined as the residual of the pixel hit coordinates from the extrapolation of the tracks reconstructed in the microstrip telescope. The strip resolution was so good (a few micron) that we could investigate the response of different regions inside a single pixel. Figure 3-22 shows the position of the tracks producing (top) *single hit* and (bottom) *double hits* in the pixel detector, projected in one single pixel. It is clear that double hits are mostly generated by tracks passing at the edge of the pixels. The corresponding position resolution for single hit events, double hits events, and average resolution are shown in Figure 3-23. The resolution in the case of single hit is 15 µm rms, corresponding to the expected value. In the case of double hits, where the position is given by the cluster coordinates, the resolution is improved to 6.6 µm rms. This yields to an average resolution of 10.8 µm rms.

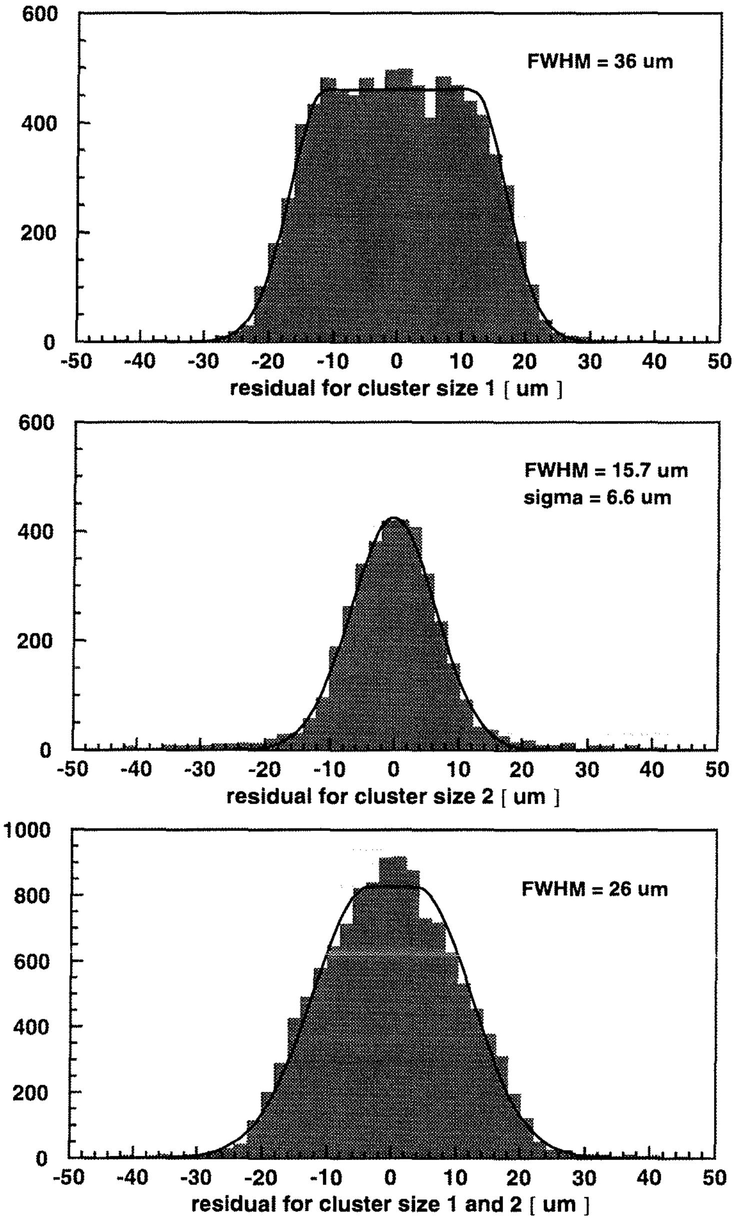

Figure 3-23: Position resolution for single hits (top), double hits (middle) and average position resolution (bottom) along the smaller dimension of the pixel.

References

[1] G. Ottaviani et al., Phys. Rev. B 12 (1975) 3318

C. Canali et al., Phys. Rev. B 12 (1975) 2265

[2] For more details on energy loss by ionisation and Bethe and Bloch formula see: W. Leo, "Techniques for nuclear and particle physics experiments: an how to approach", Berlinn Springler Ed., 1994

[3] L. Landau, J. Phys. (USSR), 8 (1944) 201

[4] G. Cavalleri et al., Nucl. Instr. and Meth. in Phys. Res. A 21 (1963) 177

[5] C. Kenney et al., Nucl. Phys. B 32 (1993) 460

[6] N. Armenise et al. (WA97 collaboration), "Study of baryon and anitibaryon spectra in Pb-Pb interactions at 160 GeV/c per nucleon", CERN-SPSLC/91-92, SPSLC/P263

[7] R. Calindro et al. (NA57 collaboration), "Study of stange and multistrange particles in ultrarelativistic nucleus-nucleus collisions", CERN-SPSLC/96-40, SPSLC/P300

[8] GEC Marconi Materials Technology Limited, Caswell, Towcester, Northamptonshire, NN12 8EQ, England.

Chapter 4

Radiation damage in silicon detectors: the *Lazarus effect*

Radiation damage in silicon detectors has been the subject of intensive studies in recent years in view of their use in future high-energy physics experiments, for instance at the CERN-LHC [1]. Several groups have followed different approaches to improve the radiation tolerance of silicon concentrating on material technology (*defect engineering*) and special detector designs.

In March 1998, I took part in the experiment in which for the first time the *Lazarus effect* was observed [2]. We discovered that heavily irradiated silicon detectors no longer operational at room temperature, because of the extremely high leakage current and the poor charge collection efficiency, *resuscitate* when operated at cryogenic temperatures. Since then, we re-started the CERN-RD39 Collaboration with a new program aimed at studying silicon detectors operated at cryogenic temperatures. We have carried out systematic studies on irradiated silicon diodes and microstrip detectors. The results show that cryogenic operation is indeed a new reliable way to increase the radiation hardness of silicon detectors.

In this chapter, I will briefly review the effect of radiation in silicon detectors, and then I will discuss the experimental results and the present understanding of the Lazarus effect.

4.1 Radiation damage in silicon

The performance of a silicon detector is predominantly determined by the bulk properties, and therefore suffers from the radiation-induced displacement of silicon atoms from their position in the lattice. Displacement damage occurs if the interaction of an impinging particle transfers sufficient kinetic energy to a silicon atom so that it is removed from its site. This atom is called *primary knock-on atom* (PKA). The threshold displacement energy is approximately $E_{disp} = 25$ eV. The maximum energy that a particle of mass m and energy E can transfer by elastic scattering to the PKA is:

$$E_{PKA}^{\max} = 4\frac{m \cdot M_{Si}}{(m+M_{Si})}E \qquad (4\text{-}1)$$

For neutrons and protons, this equation can be approximated by $E_{PKA}^{\max} \approx 4E(m/M_{Si})$, which sets to only ~175 eV the minimum energy for creating a displacement. In the case of electrons, the approximate relativistic relation $E_{PKA}^{\max} \approx 2E(E+2mc^2)/(M_{Si}c^2)$ must be used, which requires the electron energy to be larger than 260 keV to dislodge one host atom. In high-energy physics experiments, particles have energies that are orders of magnitude above the threshold energy E_{disp}. Therefore any particle traversing a silicon detector is causing a certain damage.

According to the *NIEL hypothesis*, a particle of a given energy induces a damage in the material that it crosses which is proportional to its non-ionising energy loss. Basically this means that the damage caused by different types of radiation or by the same particle at different energies only differs by a known constant factor. In order to simplify the comparison of the results obtained by different groups, generally all doses are re-normalised to the equivalent fluence of 1 MeV neutron per square centimetre. For sake of simplicity, in this thesis we will use the notation n/cm^2 to refer to these units.

The primary defects generated by displacement are *Frenkel pairs*, a lattice vacancy plus a silicon interstitial atom. In the case of electron or photon irradiation, the vacancies and the interstitials migrate through the crystal, eventually being trapped at capture sites. Conversely, heavy particles generally displace an atom giving it a high recoil energy, which generates a cascade with many interactions, some of them producing energetic secondary recoils. Each branch of the cascade finally terminates into a cluster, which contains a high density of Frenkel pairs. Vacancies and interstitials are mobile. A large fraction of them recombine on a very short time-scale, while others may diffuse out of the cluster. Here they interact with bulk impurities (oxygen and carbon) and produce stable defects, which result in a number of energy levels within the forbidden energy band-gap. Defects continue to interact during and after irradiation due to their thermal energy. In this process it is then possible that some of them are annihilated (a mechanism called *beneficial annealing*) or start to form higher order complexes, which further deteriorates the detector performance (*reverse annealing*).

The basic action of the radiation-induced defects in a silicon detector can be summarised as follows.

a) Free carriers are trapped into deep levels and cannot participate in the conduction process anymore. This effect of carrier removal, also known as *compensation* of shallow doping impurities, makes the resistance of a partially depleted detector increase.

b) Deep levels can act as *recombination* centre for electron-hole pairs. This process is not detrimental to the operation of a silicon detector.

c) In a reverse biased diode, deep levels close to mid-gap can generate excessive leakage current, which leads to noise and to an increase of power dissipation. Furthermore, the defects may become charged in the depleted region and therefore contribute to the effective doping concentration N_{eff}. In the case of n-bulk detectors, as the dose increases N_{eff} first becomes zero and then change polarity, i.e. the bulk becomes p-type (*type inversion*). It is worth reminding that before type inversion, the depleted region develops from (i.e. the electric field is maximum at) the p-side, while after type inversion it develops from the n-side. Equation 3-13, in the case of an irradiated detector, gives: $V \propto |N_{eff}|$. If the dose further increases, the overall electrical charge becomes progressively negative so that the bias voltage eventually does not deplete the detector or would have to be set so high that the excessive breakdown currents would prevent a reliable operation.

d) The charged carriers generated by ionisation can get trapped at the defect levels. Although the trapped carrier would be released later, if the average de-trapping time were comparable with the readout time, a certain fraction of the signal is lost.

A parameter that gives a good indication of the quality of a detector is the charge collection efficiency (CCE), defined as the ratio of the measured to the generated charge.

A fully depleted non-irradiated detector has 100% CCE, while for an irradiated detector the CCE decreases with the increasing dose. In order to have a more qualitative explanation of why that happens, let us recall some basic properties of irradiated detectors.

In the case of a MIP, it was already mentioned (see Section 3.3) that the signal charge Q induced on the electrodes of a detector of thickness d and depleted region W is proportional to W/d. In heavily irradiated silicon detectors, the conductivity is related to the deep-level defects, rather than to the shallow-level dopants of the non-irradiated material [3]. As a result, after that the material has undergone type inversion, the non-depleted region of a diode has a resistivity close to that of an insulator, and acts as a capacitive divider, which reduces the signal collected at the electrodes. The signal measured in thus proportional to $Q \times (W/d)$ [4]. Therefore, the charge collection efficiency of a partially depleted heavily irradiated silicon detector behaves as $(W/d)^2$.

Moreover, if the electrons and holes generated by ionisation are trapped during their drift, some fraction of the signal is lost and the CCE is less than 100% even for a fully depleted detector. Consequently the CCE can be (qualitatively) expressed as:

$$CCE \propto \left(\frac{W}{d}\right)^2 \exp\left(-\frac{t_{drift}}{\tau_{trap}}\right) \tag{4-2}$$

where t_{drift} is the drift time of the excited carriers, and τ_{trap} is the trapping time constant related to the radiation-induced deep levels.

A possible way to prolong the detector lifetime consists in fixing the working temperature of silicon detectors slightly below 0°C [5]. Moderate cooling is in fact applied to lower the detector leakage current and to inhibit reverse annealing. However, low temperature does not prevent the dramatic changes in depletion voltage that we have discussed. Sophisticated multi-guardring designs can be used to increase the maximum bias voltage that can be applied to a detector. Nevertheless, when the radiation fluence approaches 10^{15} n/cm^2, which is the anticipated irradiation of the innermost trackers after 10 years of LHC operation [6], the detectors become unusable. It is worth mentioning that the detectors must be always operated at low temperature, because even a rather short warm-up at room temperature would degrade considerably the detector performance, due to annealing effects.

Lately it has been observed [7] that oxygen enriched silicon detectors show a smaller increase of the depletion voltage when irradiated with charged particles. Unfortunately, these results have not been confirmed when the detectors were irradiated with neutrons (which is also in contrast with the NIEL hypothesis).

4.2 The Lazarus effect

The active thickness W of an under-depleted detector depends on the applied bias voltage V and on the space charge density N_{eff} according to the relation (from Equation 3-13):

$$W = \sqrt{\frac{2\varepsilon\varepsilon_0 V}{e|N_{eff}|}} \tag{4-3}$$

For detectors irradiated beyond type inversion, N_{eff} at room temperature is negative. When the temperature decreases, the emission process is drastically suppressed due to the exponential dependence of the de-trapping time τ_d from the temperature:

$$\frac{1}{\tau_d} \propto \exp\left(-\frac{E_t}{kT}\right) \qquad (4\text{-}4)$$

where E_t is the trap energy and k the Boltzman constant. It is worth mentioning that this effect is important only for the radiation-induced traps, which are deep in the silicon band gap (E_t ~0.5 eV), while it is much less pronounced for shallow defects.

As a result, at cryogenic temperatures a substantial fraction of the radiation-induced traps is filled and then inactive. Because of the exclusion principle, in fact, the charge carriers created by ionisation cannot be trapped into a filled trap and no signal is lost. Similar properties have been observed in the case of diamond detectors, in which the as-grown material already contains very deep traps. In this case, even at room temperature, neutralisation of deep traps is normally achieved by optical or electrical filling [8].

The filled traps become charged and affect the space charge region density N_{eff}. It has been shown [9] that as the temperature goes down, N_{eff} decreases in absolute value, reaching a minimum around 130 K and then slightly increasing again. This implies that, for the same applied bias voltage, the active thickness and then the collected charge of the detector increases with decreasing temperatures.

The operation at cryogenic temperatures has thus a beneficial effect in both the geometrical and trapping term of Equation (4-2). The CCE recovery of heavily irradiated silicon detectors when operated at cryogenic temperatures is referred to as the *Lazarus effect.*

4.3 Results on diodes

4.3.1 Samples and experimental set-up

The devices investigated are Al/p$^+$/n/n$^+$/Al silicon diodes. The n^+ implant covers homogeneously the backside of the wafer from which the diodes are fabricated. These structures have a sensitive area of 5×5 mm^2 surrounded by a guard-ring. Before irradiation, full depletion is achieved at room temperature with voltages between 50 and 80 V. The diodes were irradiated with neutrons at room temperature. The properties of the investigated detectors are summarized in Table 4-1.

Diode	Fluence (n/cm^2)	Thickness (μm)	Resistivity (kΩ cm)
#1	$1{\cdot}10^{14}$	350	1.8
#2	$5{\cdot}10^{14}$	400	4
#3	$1{\cdot}10^{15}$	400	4
#4	$2{\cdot}10^{15}$	300	2.7

Table 4-1: Parameters of the investigated diodes. The resistivity values are those before irradiation.

The minimum fluence value of 10^{14} n/cm^2 exceeds already the value for bulk type inversion. The detectors #1, #2 and #4 were kept at room temperature and were eventually heated to reach the annealing state corresponding to about one year of room temperature storage. The sample #3 was kept at –18°C soon after irradiation. It was then heated to reach the same annealing state as the other samples only after a first complete series of measurements. This procedure allowed us to investigate the sample in both annealed and not-annealed state, in order to verify the importance of the reverse annealing process for operation at cryogenic temperatures.

The measurements were performed in a cryostat consisting of a dewar vessel and an insert. The insert is a vacuum-tight stainless steel tube in which the detector, the trigger diode and the radioactive source are mounted. The tube is inserted into a transport dewar containing liquid nitrogen. The tube walls are in direct contact with the liquid nitrogen around the sample area and are therefore thermalized at 77 K. The sample under investigation is cooled by means of helium exchange gas at 100 mbar pressure. The temperature was monitored using a silicon diode thermometer glued on a copper support structure onto which the detector and trigger printed circuit boards (PCBs) are fixed by screws. The experimental configuration is shown schematically in Figure 4-1.

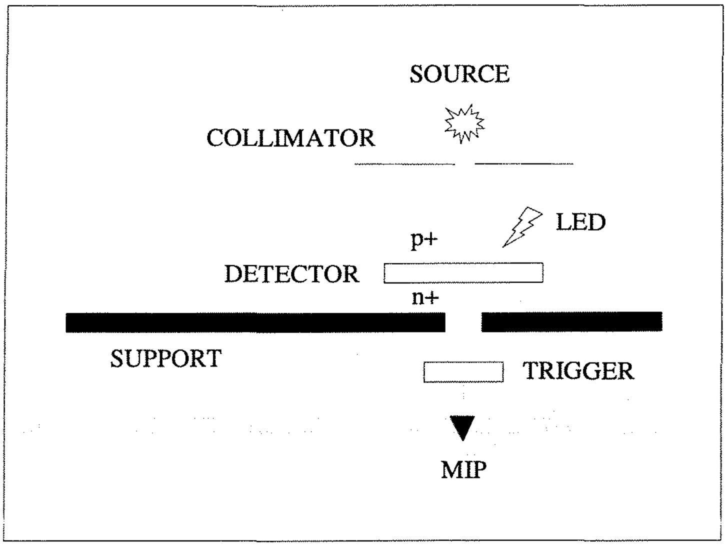

Figure 4-1: Schematic of the experimental configuration.

The samples were exposed (from the p^+ side) to electrons from a ^{90}Sr β-source. A second silicon detector placed behind the detector under study was used as a trigger to select minimum ionizing particles (MIP). LEDs of different wavelength were used for a series of special measurements, described in Section 4.3.6. The detector signal was read (from the n^+ side) by means of a GaAs FET mounted on the copper support structure. This FET acts as the front-end of a charge amplifier, whose subsequent stages are at room temperature. The noise of the amplifier is completely dominated by the long cable between the FET and the amplifier, and was measured to be about 1500 electrons FWH. The charge signal was then shaped (1 μs shaping time) and sent to a multi channel analyzer for recording the charge distribution.

The most probable value of the collected charge in the diode was determined by fitting the charge spectrum by a Landau distribution function, and subtracting the pedestal fitted by a Gaussian function. The CCE of the irradiated samples was then determined normalizing to the calibration value, obtained from the charge spectrum of a non-irradiated detector of the same thickness operated above full depletion. The statistical error from the fit was added linearly to the systematic uncertainty on the detector thickness.

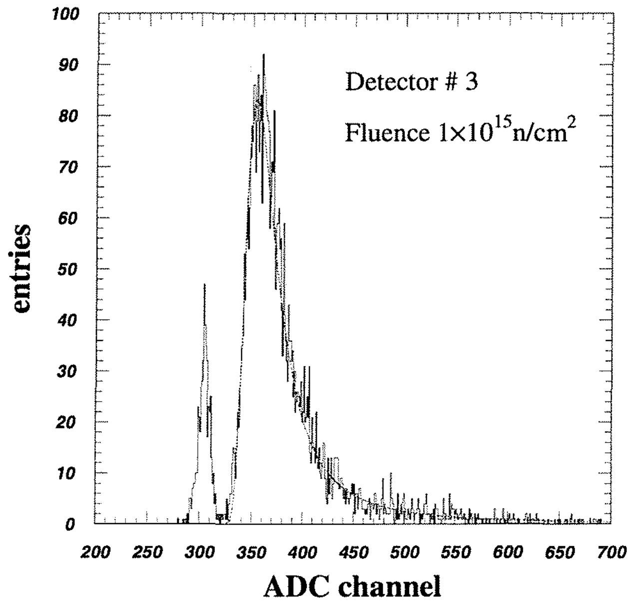

Figure 4-2: Charge spectrum obtained from detector #3 at 77 K with 250 V reverse bias.

Figure 4-2 shows the charge spectrum obtained with sample #3 at 77 K and 250 V bias voltage. The corresponding CCE was ~20%. It is worth stressing that the noise pedestal is completely separated from the signal, which ensures the possibility of having a 100% efficient binary readout system.

4.3.2 Current-Voltage characteristics

For the measurement of the current-voltage (I-V) characteristics, the samples were cooled to 77 K by direct immersion into a liquid nitrogen bath. The maximum detector bias that could be applied was 250 V and was limited by the electric isolation on the sample PCB. The sensitivity of the current measurement was limited to about 1 nA due to the leakage in the capacitors used for filtering the bias voltage.

Figure 4-3 shows the I-V characteristics at room temperature for samples #1, #2 and #3. In reverse bias, the expected increase of the current with fluence is observed. In forward bias, detector #1 features an exponential rise of the current, whereas at higher fluences (detectors #2 and #3) the I-V curves are almost linear, close to ohmic characteristics. At 77 K, the currents in both reverse and forward polarity are all compatible with zero within the resolution of the measurements, except for detector #1 which has a breakdown at –30 V. In the case of samples #2 and #3, the bulk material behaves as a resistor of very high value. This effectively limits the current also in the forward direction of the applied voltage up to –250 V.

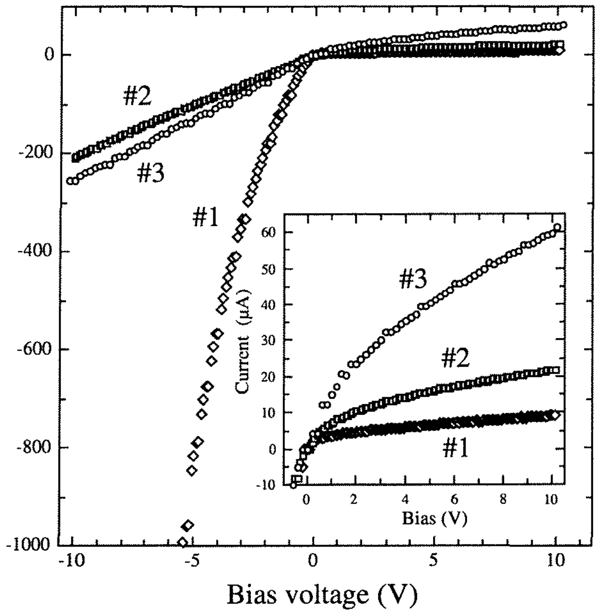

Figure 4-3: Current-voltage characteristics measured at 300 K at both bias voltage polarities, for detectors #1, #2 and #3. In the insert, the reverse current is shown on a blown-up scale.

4.3.3 Temperature dependence of the CCE

The temperature scan of the CCE is performed according to the following procedure. The sample is mounted and the insert is evacuated until the pressure is reduced to ~100 mbar. After that, the tube is immersed into liquid nitrogen. From this moment onwards, the sample starts to cool due to thermal radiation and to the small amount of residual gas, which creates a weak thermal link with the tube wall at 77 K. The bias value chosen for the temperature scan is applied and the leakage current is monitored together with the temperature. As soon as the leakage current is reduced to such a value that the noise does not exceed 2000 electrons FWHM, the measurements of the CCE is started. The cooling was slow enough that the temperature changed by less than 1 K during the 20 s interval needed for recording the spectrum from which the CCE was determined.

The temperature dependence of CCE for detectors #1, #2 and #3 is shown inFigure 4-4. The sample #4 has a temperature dependence similar to that of detector #3 and is therefore omitted in the figure for clarity. The three detectors were biased with a voltage such that at high temperature they are certainly not fully depleted (100 V for sample #1 and 250 V for samples #2 and #3). All detectors show very low CCE values in the high temperature range. The CCE shows a substantial rise below ~180 K and reaches its maximum value at a temperature of about 130 K for all samples, before slightly decreasing at lower temperatures. Figure 4-4 also shows sample #1 biased at 250 V. In this case, the detector becomes fully depleted for T < 130 K, and the CCE stays at ~100% also for lower values of T. These results seem to confirm the expectation (see Section 4.2) that the recovery of the CCE at cryogenic temperatures is due to an increase of the depletion region, for a given value of the applied bias voltage.

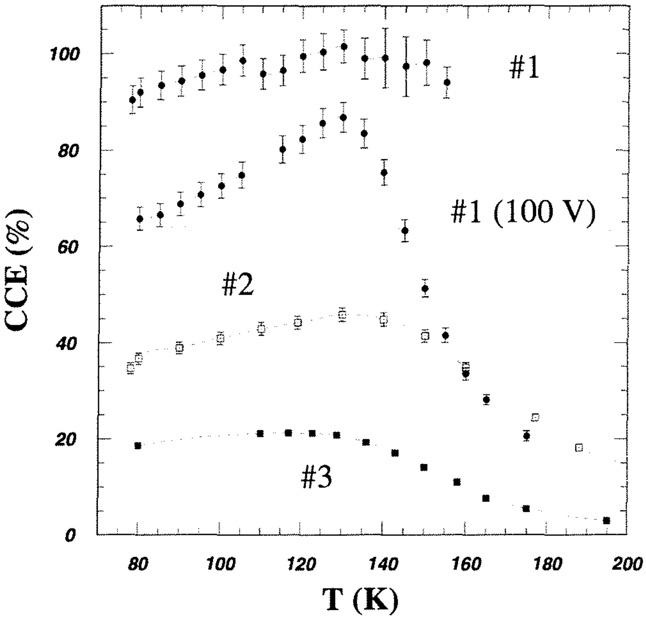

Figure 4-4: CCE versus temperature for detectors #1, #2 and #3. The three detectors have been measured at 250 V reverse bias voltage. The detector #1 has been measured also at 100 V reverse bias voltage.

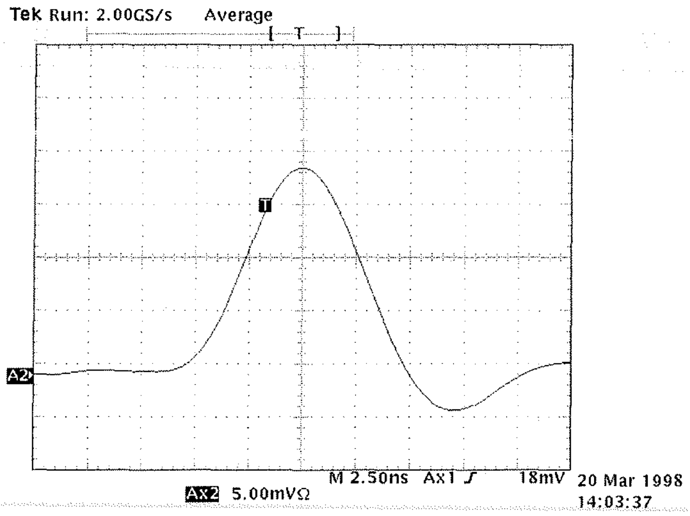

Figure 4-5: Current signal from sample #4 at 77 K. The detector bias voltage was 250 V.

In order to check the signal timing, we have measured the current pulse of sample #4 operated at 77 K and with 250 V bias. The detector signal was amplified with a fast (5 ns rise time) low noise (5 μV rms) voltage amplifier and acquired by a digital oscilloscope in averaging mode. As shown in Figure 4-5, the detector pulse is fully contained in the ~15 ns. We can therefore say that the results obtained with 1 μs shaping time can be extrapolated also to applications where shorter integration times are required.

4.3.4 Bias voltage dependence of the CCE

We have investigated the dependence of the CCE on the bias voltage. In this section, we concentrate on the conventional reverse bias operation. For each bias voltage, the CCE measurements were also repeated at various time intervals after bias turn-on, in order to check for any dependence with time.

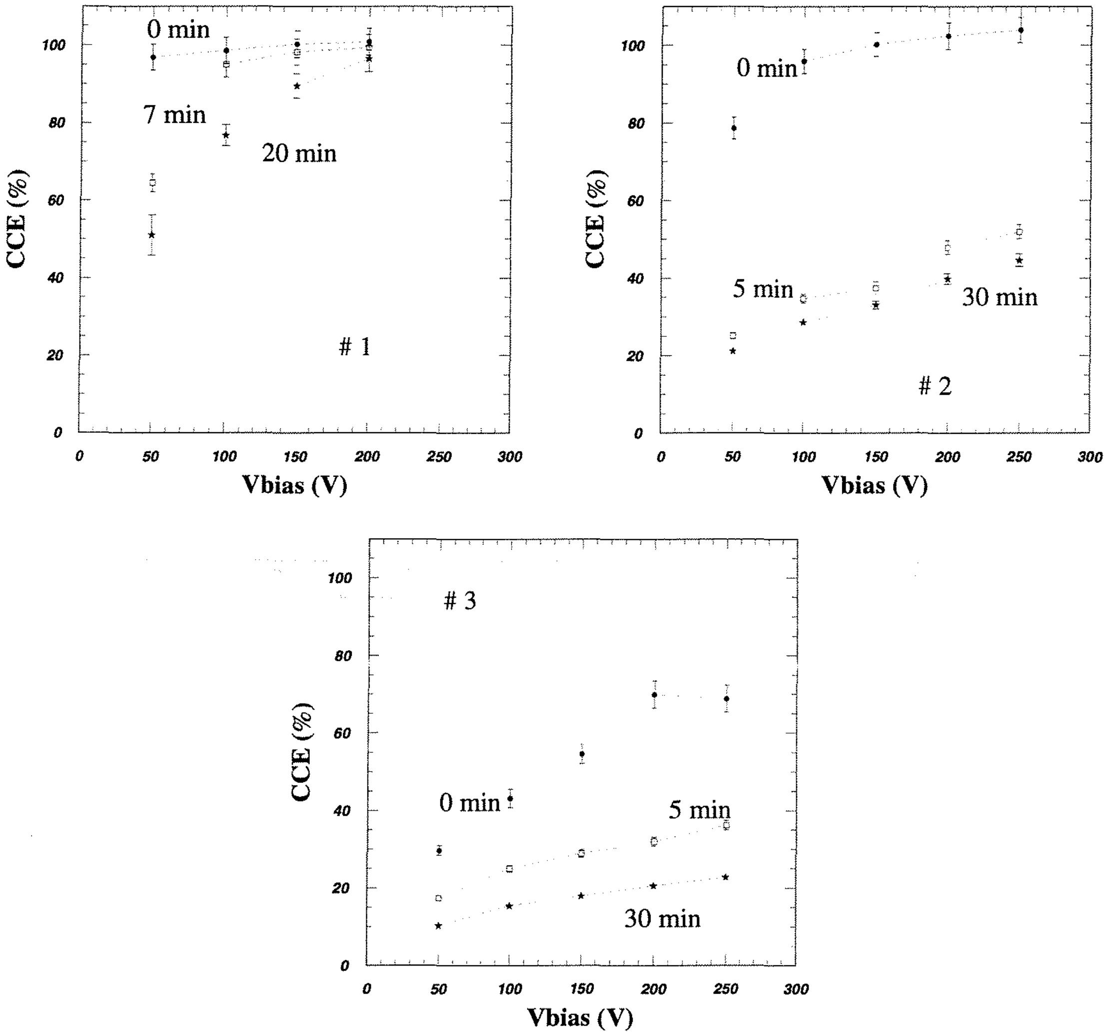

Figure 4-6: Voltage dependence of the CCE at 77 K for detectors #1-3 measured after different time intervals from detector bias turn-on.

Before applying the desired bias voltage, the detector was kept unbiased (0 V) for ~15 minutes in order to achieve stable conditions for the filling of the traps. It is known that in materials rich in deep-level traps, the history of the bias voltage plays a crucial role for the time evolution of the amplitude of the signal at cryogenic temperatures. In particular, reversing the bias polarity generates a transient situation in the bulk during which the radiation-induced electrical pulses are gradually reduced in amplitude, and change sign only after a few minutes. This process, called *detector polarisation*, was originally observed for germanium detectors [10]. It is therefore very important to prepare the detector always in stable conditions before applying the desired bias voltage.

The voltage dependence of the CCE for the samples #1, #2 and #3 at 77 K is shown in Figure 4-6. The most striking feature is that in all cases the CCE decreases with time. We have verified that the CCE value registered after 30 minutes is always compatible within the experimental errors with the stable value that is obtained after 24 hours. It should be noticed that the values shown in Figure 4-4 are the stable values. It is also clear that the CCE increases with the applied bias voltage, and eventually reaches 100% at 250 V for detectors #1. In the case of samples #2 and #3, the stable CCE does not seem to reach a plateau, indicating that improved values could be obtained at higher bias voltage.

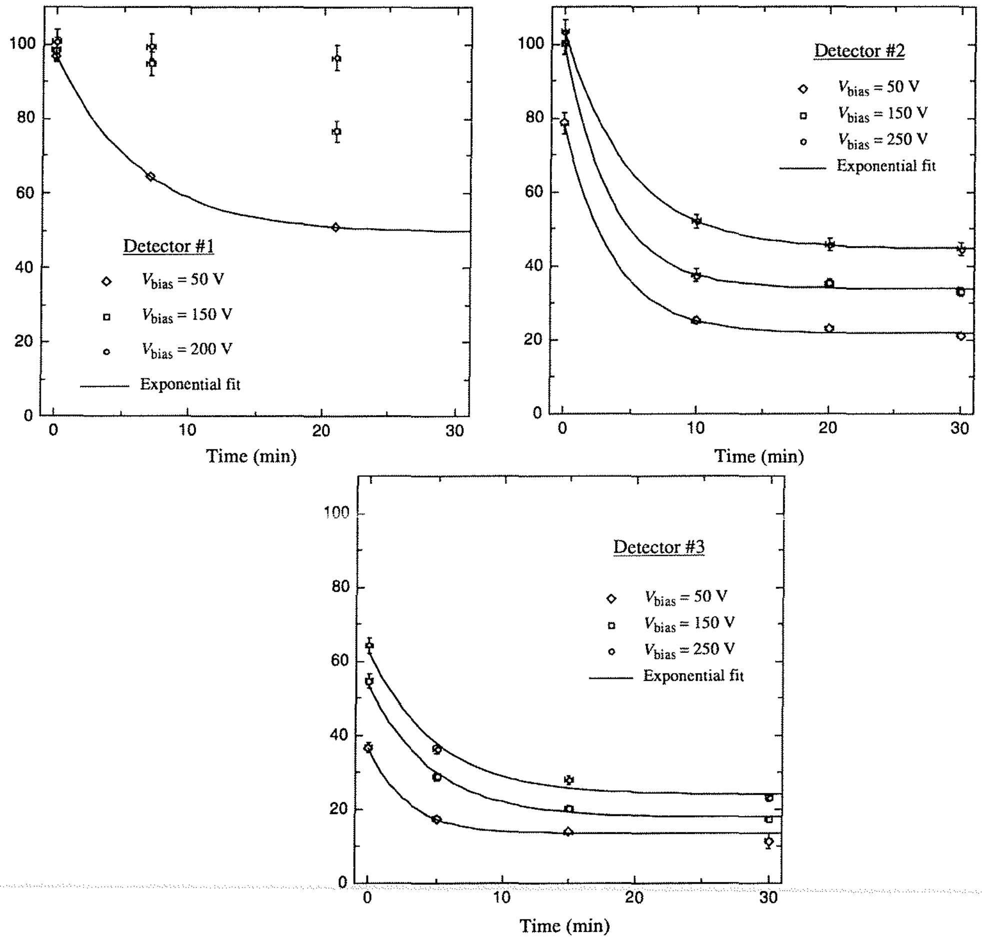

Figure 4-7: Time dependence of the CCE at 77 K for detectors #1, #2 and #3.

In order to understand better the important phenomenon of the time dependence of the CCE, the data of Figure 4-6 are plotted as a function of time in Figure 4-7. The time constants from the exponential fits to the curves are given in Table 4-2.

Detector	Bias voltage (V)	Time constant (min)
#1	50	6.1 ± 2.0
#2	50	3.6 ± 0.4
#2	150	3.5 ± 0.6
#2	250	4.8 ± 0.8
#3	50	2.9 ± 0.4
#3	150	4.6 ± 0.5
#3	250	4.9 ± 0.6

Table 4-2: Time constants of the exponential decay of the CCE, obtained from the fit of the data of Figure 4-7. Only statistical errors are listed.

It is clear that the larger the applied bias voltage, the higher is the initial CCE value, and the slower is its decrease with time. In the case of the two most irradiated samples, most of the CCE loss takes place in the first five minutes after the bias is applied. It is also important to note that in the case of detector #1 it is possible to completely suppress the time dependence of the CCE by means of a fairly large bias voltage, which corresponds to an over-depletion condition.

4.3.5 Forward bias operation

Special measurements were performed with the detectors operating in non-conventional modes: under forward bias and in presence of light. In forward bias, the electric field is expected to be nearly uniform along the detector bulk, which is thus almost fully sensitive to MIPs [11]. Furthermore, the larger current with respect to reverse bias may help in filling a larger fraction of radiation-induced traps [12]. Another method of trap filling that was also suggested some time ago is operation in presence of light [13]. Forward bias operation was investigated on irradiated silicon detectors cooled between 250 and 270 K [14], while we are not aware of data collected on diodes operated in presence of light. Unfortunately, in the case of moderate cooling, the high currents (~10 μA/mm^2) limit the application to small-area sensitive elements, such as pixel detectors.

It is worth reminding that in the case of operation at 77 K, the steady state current was measured to be less than 1 nA per 5x5 mm^2 up to 250 V of both bias voltage polarities. The temperature dependence of the CCE for detectors #2, #3 and #4 in forward bias operation is shown in Figure 4-8. As in the case of reverse bias, the CCE starts to increase at T~180 K and saturates around 130 K for all detectors. The values measured are about three times higher than those observed under reverse bias. Moreover, as long as the forward current is small enough to allow performing a measurement, good values of CCE are recorded also at relatively high temperatures, in good agreement with what has been observed before [14].

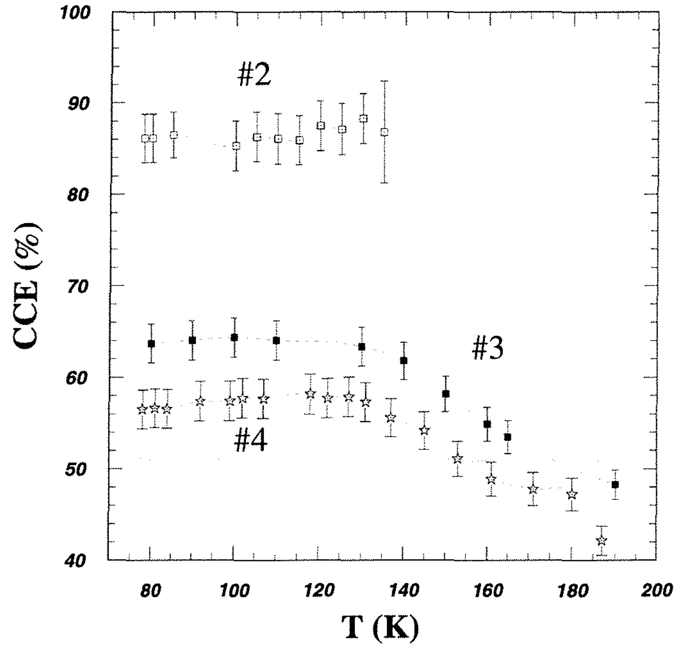

Figure 4-8: CCE versus temperature for detectors #2, #3 and #4 at 250 V forward bias.

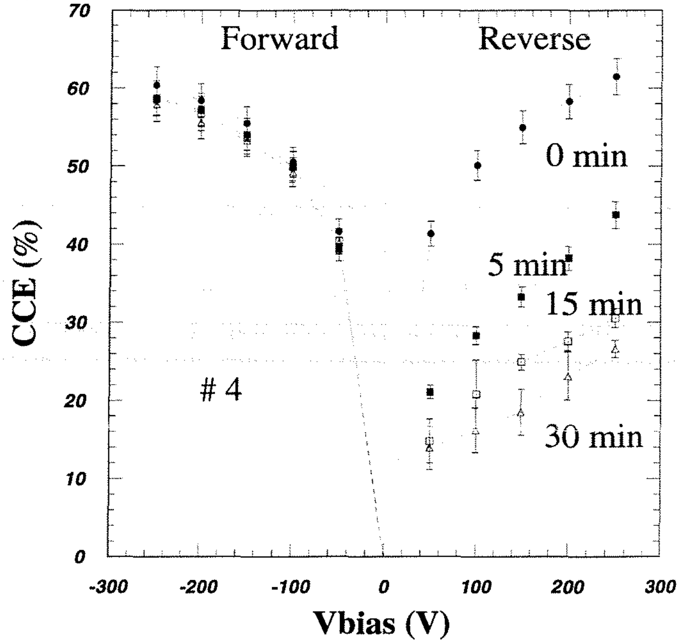

Figure 4-9: Voltage dependence of the CCE of detector #4. Different measurements at various time intervals after bias turn-on are also shown.

Figure 4-9 shows the CCE of the detector #4 (irradiated to the highest fluence) measured at 77 K over the full range of available bias voltages. Similar results were observed for detectors #2 and #3. The most important feature is that the CCE in forward bias does not decay in time. Moreover, the CCE values obtained in forward bias are similar to those observed under reverse bias immediately after switching on the bias. However, it is worth stressing that the maximum value does not reach 100% at 250 V.

4.3.6 Light illumination

We have investigated the CCE of sample #4 when illuminated on the front side (p^+) with light of different wavelengths. The colors of the light-emitting sources (LED) we used were: near infrared 850 nm (IR), red (R), yellow (Y) and green (G). The intensity of the emitted light could be adjusted by varying the current in the LED and by observing the corresponding increase in the detector bias current. The illumination was maintained constant during the CCE measurements.

The intensity of the applied light was adjusted so that the leakage current was about 5 nA, which did not add a significant contribution to the overall noise of our measurement system. Figure 4-10 shows the CCE of detector #4 as a function of the bias voltage for the different light sources. The main effect of the light illumination is that no time dependence of CCE is observed also in reverse bias. The measured CCE, however, depends on the light wavelength and on the applied bias polarity.

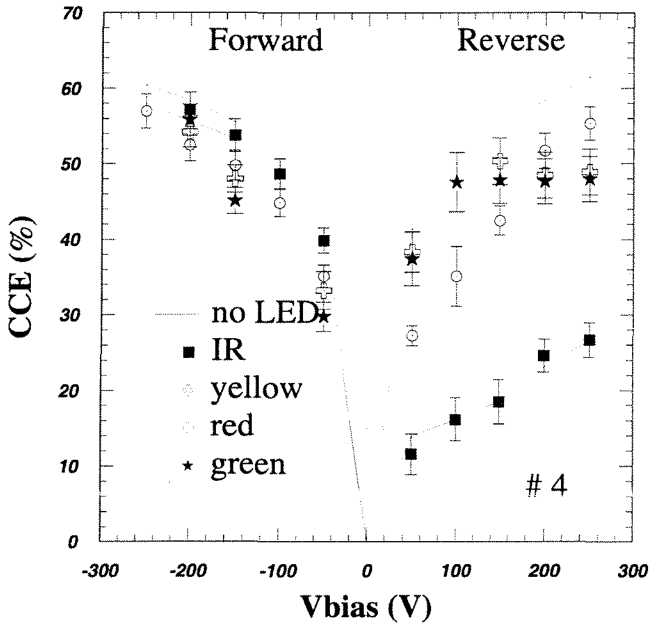

Figure 4-10: Effect of light illumination on the voltage dependence of the CCE over the entire allowed range for detector #4. The solid lines are the values obtained without light soon after the bias turn-on and after 30 minutes.

In the case of reverse bias operation and illumination with short wavelength light (Y, G) the good values obtained immediately after switching on the HV are maintained. Under this bias condition, also the IR light has the effect of stabilizing the CCE, but yields values comparable to the saturated ones in the absence of light. Red light produces an intermediate effect. Despite good noise performance in reverse bias operation, the quality of the fits to the Landau distribution was slightly deteriorated, as reflected in the error bars. This effect could be due to the non-uniformity of the illumination of the sensitive area of the diode. Under forward bias, the CCE in the presence of light is compatible, within the experimental errors, with the CCE without light.

4.3.7 Annealing effects

The possible effects of the reverse annealing process on the CCE recovery were investigated on sample #3 (fluence 1 10^{15} n/cm^2), as discussed in Section 4.3.1. The CCE was measured before (NRA) and after (RA) annealing over the full allowed bias range, as shown in Figure 4-11. No significant difference is found between these two sets of measurements. This suggests that the deep defects, which can be deactivated by means of operation at cryogenic temperatures, are formed during (or soon after) irradiation at room temperature, and are not seriously affected by the reverse annealing process

It is important to stress that these results show that devices need to be cooled only during operation and otherwise can be stored at room temperature.

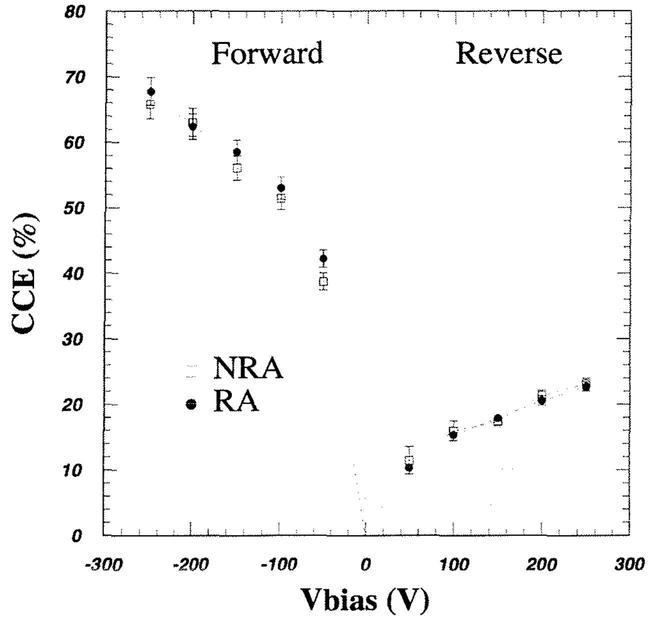

Figure 4-11: Effect of reverse annealing on the voltage dependence of the CCE for detector #3. In reverse bias the stable saturated values are plotted

4.4 Results on microstrips

The data presented on single diodes show that the CCE of heavily irradiated silicon detectors recovers if the device is operated around 130 K. The recovery is three times higher if an appropriate manipulation of the bulk current is carried out, for instance via forward bias or light illumination. In order to check whether the cryogenic operation of silicon detectors represents indeed a valid technique for application in high-energy physics experiment, we needed to verify that the recovered charge stays also focused.

For this purpose, we have investigated the performance of a microstrip detector, irradiated with 3.5×10^{14} protons/cm^2, and operated at cryogenic temperatures in a test beam. After having described the detector and the experimental set-up, I will discuss the results obtained on the CCE and on the position resolution.

4.4.1 Experimental set-up

The investigated detector was a DELPHI module [15], which is illustrated schematically in Figure 4-12. It consists of two *plaquettes* daisy chained together and wire-bonded to a double-sided ceramic support, where the readout chips are glued. Each plaquette is a 310 μm thick AC coupled double sided microstrip detector with a sensitive area of 3.2×5.4 cm^2. The *p*-side of the plaquette has 1280 strips with a pitch of 25 μm, with every second strip being read-out. The *n*-side has 1280 strips with a 42 μm pitch, which run perpendicular to the *p*-side strips.

The n^+ strips are separated from each other via p^+ blocking electrodes. On the *n*-side of the plaquette closest to the ceramic, neighbouring strips are connected together giving an effective 84 μm readout pitch, which leads to a two-fold ambiguity in the position determination.

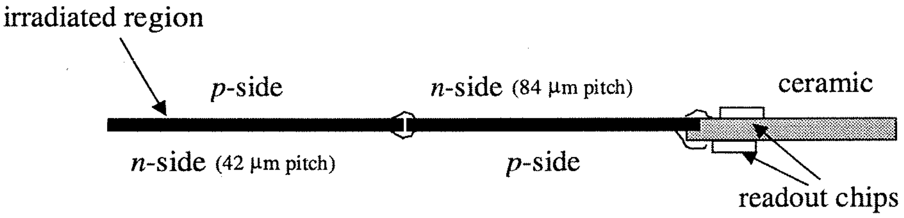

Figure 4-12: Schematic of the DELPHI module.

Since the readout lines of both sides of the detectors are at the same potential (due to the AC coupling), the daisy chaining connects the readout lines of the *p*-strips of one plaquette to those of the *n*-strips of the second plaquette. This technique allows equalising the noise on the two sides of the module. Furthermore, the polarity of the signal tags in which of the two plaquettes there was a hit. This feature helps in removing ambiguities in the cluster reconstruction, at the expense of having a bipolar front-end readout electronics. The maximum depletion voltage that can be applied to the strips is around 90 V to avoid breakdown of the coupling capacitors between the strip implants and the readout lines. The ceramic is equipped with 10 MX6 CMOS chips (manufactured in 3 μm technology), 5 per side, each of them reading out 128 strips.

The plaquette furthest away from the ceramic was irradiated at room temperature with 24 GeV protons. The average dose on a 1 cm^2 region was determined by measuring the activation of a piece of aluminium to be 3.5×10^{14} protons/cm^2, which corresponds to about 2×10^{14} 1 MeV neutrons/cm^2. The irradiation was inhomogeneous, reflecting the proton beam profile, with the nominal maximum intensity centred on the detector at approximately 1 cm away from the edge. After irradiation, the detector drew a total current of 1 mA when biased with 65 V at room temperature, preventing a reliable operation.

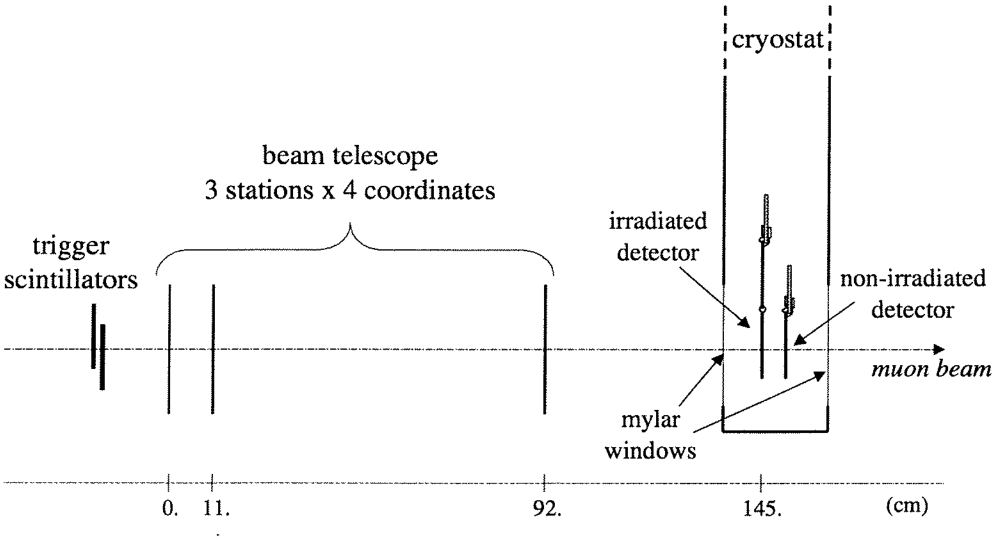

Figure 4-13: Schematic of the beam test set-up.

The irradiated detector was tested in a 100 GeV/c muon beam at CERN. The experimental set-up is depicted in Figure 4-13. Tracks were reconstructed using a beam telescope consisting of 3 stations of silicon single-sided microstrip detectors, each measuring four coordinates (x, y, +45° and -45°). The trigger was provided by the coincidence of two scintillators placed upstream of the telescope. The irradiated detector was housed in a cryostat placed half a meter downstream the telescope, together with a non-irradiated module used as reference. This reference module is similar to the irradiated one, but consists of one plaquette only. The coordinate system is defined such that the x coordinate is measured by the p-side strips, and the y coordinate by the n-side strips.

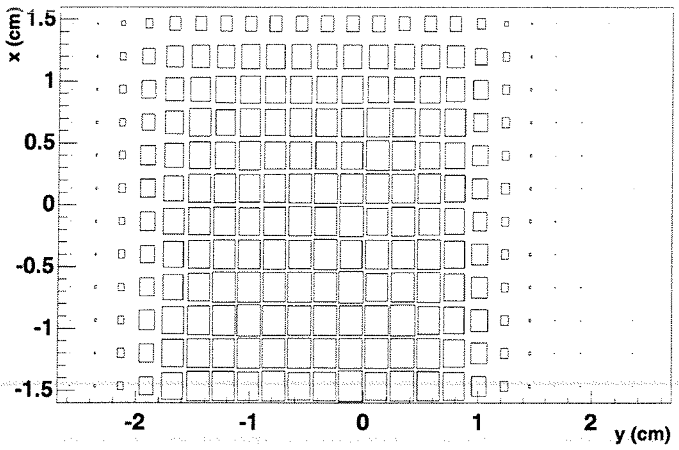

Figure 4-14: Beam profile as seen on the surface of the non-irradiated detector.

The muons traversed two 100 μm thick aluminised mylar windows passing through the cryostat. The beam defined by the trigger scintillators was not illuminating the whole surface of the irradiated detector, as shown in Figure 4-14.

The temperature was continuously monitored by PT100 resistors placed in the detector chamber and on the two module ceramics. After the beam test, another PT100 probe was glued directly on the irradiated detector, and it was found that its temperature was about 5 to 10 degrees below the temperature of the ceramic. All temperatures quoted in the following sections refer to the temperature as measured on the ceramic of the irradiated detector.

The data were collected in a series of ~15 minutes runs. Table 4-3 summarises the relevant parameters for each run. In a first period (runs 560-569), the reference module was switched off. From run 570 onwards, the reference module was switched on, and the average operating temperature increased due to the higher power dissipation and insufficient cooling power of the cryostat. All runs could be used to measure the charge collection efficiency, whereas the resolution studies are based only on the data where both modules were switched on.

Run number	Bias voltage (V)	Current (μA)	Temperature (K)
560	10	< 0.1	116
561	30	< 0.1	117
562	50	< 0.1	118
563	70	0.6	118
564	90	1.3	118
565	90	1.3	118
566	70	0.6	118
567	50	0.1	118
568	30	< 0.1	118
569	13	- 1.3	118
570	12	- 1.1	119
571	30	< 0.1	123
572	50	0.1	124
573	70	0.9	126
574	90	1.9	126
575	70	1.1	127
576	50	0.1	128
577	30	< 0.1	129
578	14	- 1.1	129
579	14	- 1.3	144
581	50	0.1	150
582	70	1.8	150
588 to 597	90	1.2	135

Table 4-3: Run list with the relevant parameters.

The first step of the analysis was to reconstruct the muon tracks in the beam telescope. A total of about 20'000 tracks were successfully reconstructed and extrapolated into the DELPHI modules with an accuracy of approximately 17 μm in both coordinates.

The temperature variations from one run to the other were reflected in vertical movement (of the order of 100-200 μm) of the two DELPHI modules relative to the telescope. This was due to the fact that the DELPHI modules were fixed to a copper finger inside the cryostat insert. As a consequence, the DELPHI detectors had to be aligned with respect to the beam telescope for each run or each series of consecutive runs taken at a certain temperature.

4.4.2 Cluster shape model

As discussed in Section 4.1, in a heavily irradiated detector, which has undergone type inversion, the depletion region grows with the applied voltage from the *n* side. Moreover, the CCE for a MIP of a detector of thickness *d* is expected to scale with $(W/d)^2$, where *W* is the thickness of the depleted region. We have developed a simple geometrical model, which attempts to predict the resolution of a double-sided microstrip detector, given the amount of charge collected by the strips.

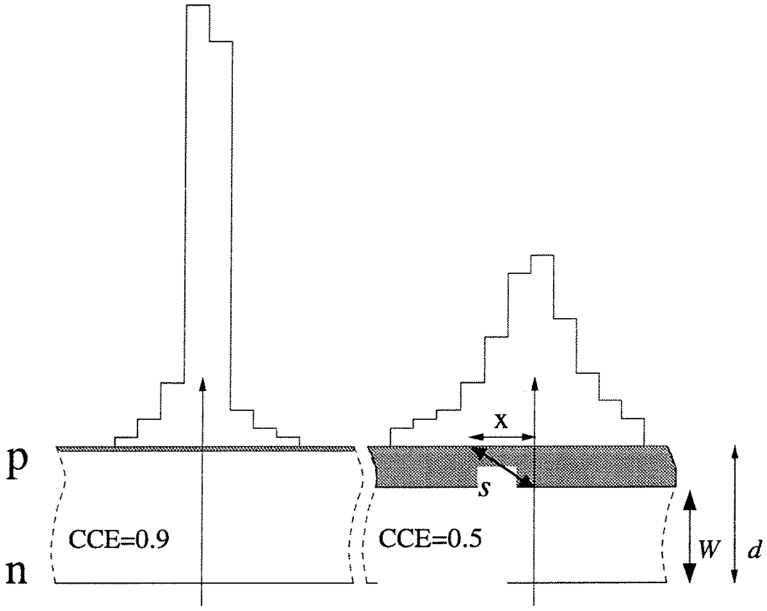

Figure 4-15: Sketch of the charge distribution on the p-side of the detector according to Equation (4-5) for two depletion depths.

The electrons and holes released by the passage of a MIP drift along the electric field lines in a direction perpendicular to the detector plane. In the irradiated plaquette (which has undergone type inversion) the field lines always reaches the implants on the *n*-side. Therefore the cluster shape on the *n*-side is expected to be similar to that of a non-irradiated detector. The holes drifting towards the *p*-side stop drifting when they reach the non-depleted region. Let us define *s* the distance between the p^+ implant and the point at the edge of the non-depleted region where the track passed through (see Figure 4-15). We postulate that the charge seen on each strip is proportional to $1/s^2$. If the strip pitch is sufficiently fine with respect to the width of the non depleted region, this results in a significant spread of the resulting cluster. In Figure 4-15, we have $s^2 = x^2 + (d - W)^2$.

The left figure shows the case when the CCE is ~90%, with a cluster shape close to normal also on the p-side. The right figure shows the contrasting situation when 25% of the detector thickness is non-depleted, corresponding to a CCE of 50% and to a much wider cluster.

According to this model, the fraction of charge collected by the i-th strip separated by a distance x_i from the traversing particle is equal to:

$$q(x_i) = \left(\frac{1}{s_i^2}\right) \Bigg/ \left(\sum_k \frac{1}{s_k^2}\right) = \left(\frac{1}{x_i^2 + (d-W)^2}\right) \Bigg/ \left(\sum_k \frac{1}{x_k^2 + (d-W)^2}\right) \qquad (4\text{-}5)$$

Fitting this expression to the measured cluster shape gives the values of W, the thickness of the depleted region. This procedure can be used to verify whether the charge collection inefficiency is due only to the fact that the detector is partially depleted, or there is also a fraction of the signal lost due to trapping. In fact, if all the charge loss can be attributed to incomplete depletion, the measured CCE on the n-side of the detector will be equal the $(W/d)^2$, with W being the result of the fit to the cluster shape on the p-side.

Once we will have verified that the model gives a good description of the CCE results, we will use it to predict the position resolution on the p-side given the amount of charge collected on the n-side strips.

4.4.3 Results on the CCE

The gain of the readout chips was calibrated using tracks passing through the region that had suffered the least radiation. The most probable energy loss of a MIP as measured by each chip is shown in Figure 4-16.

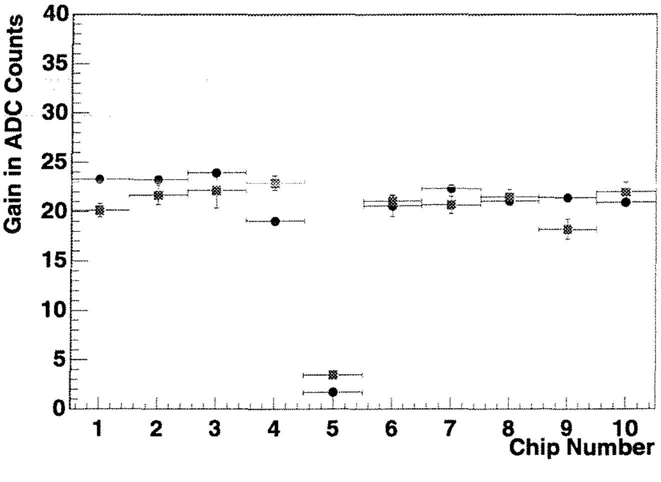

Figure 4-16: Chips gain on the p-side (chips 1-5) and on the n-side (chips 6-10) for the reference (circles) and irradiated (squares) detectors.

Since the DELPHI modules were not designed for cryogenic operation, it was not surprising that the operating voltages were not supplied uniformly to the readout chips. This resulted in one malfunctioning chip on the reference detector and one chip with low

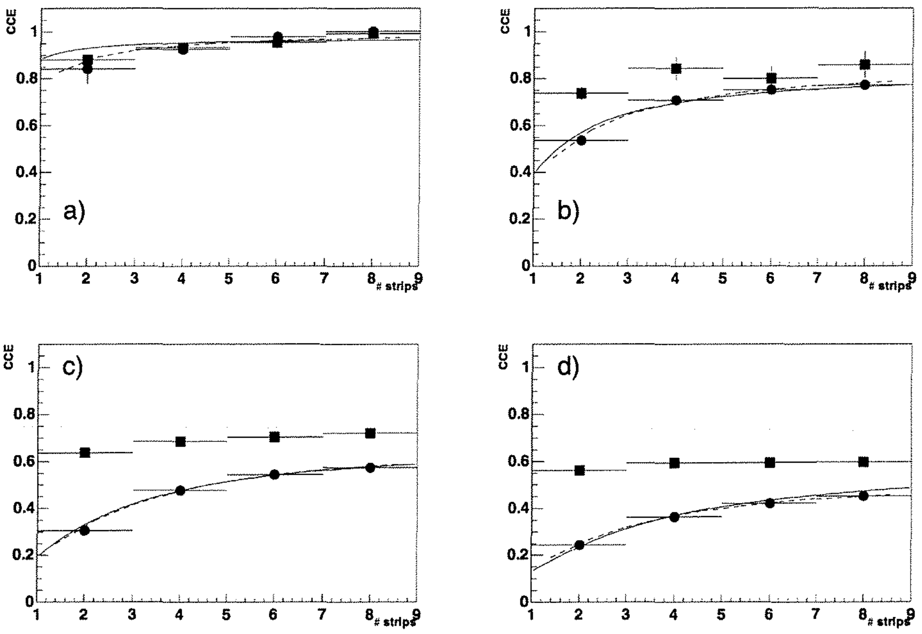

Figure 4-17: CCE as a function of the cluster size, for the n-side (squares) and p-side (circles) in four different regions of the irradiated plaquette. The curves show the results of the one-parameter (solid) and two-parameters (dashed) fit to Equation (4-5).

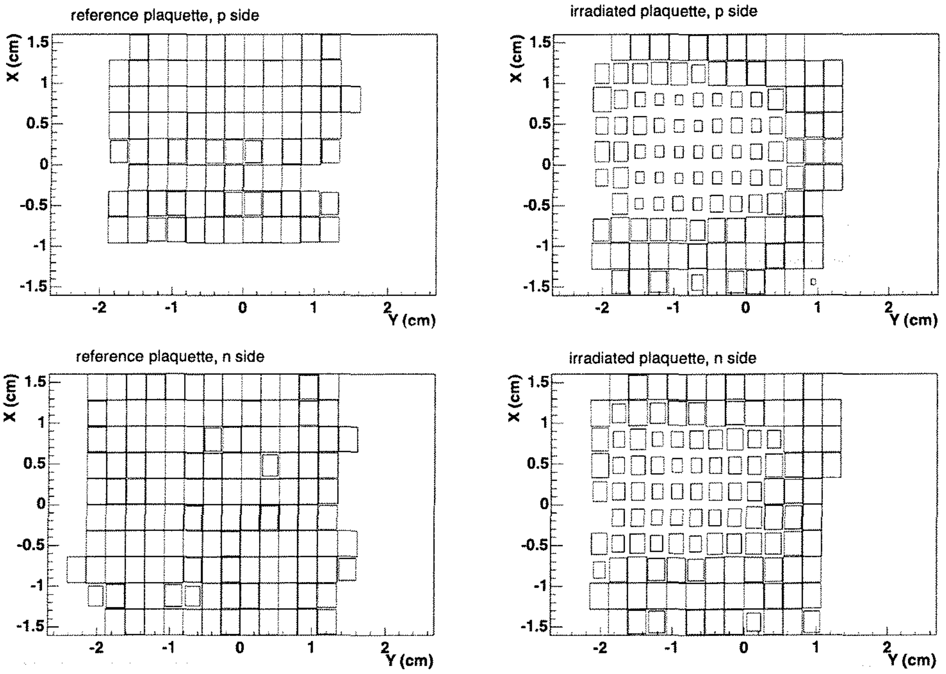

Figure 4-18: CCE for runs 590-597. A full square indicates 100% CCE. The absence of a square indicates insufficient statistics to perform a measurement. The empty band on the p-side of the reference plaquette corresponds to the region of the dead chip.

gain on the irradiated detector. The 18 other readout chips functioned normally, with a gain variation around 10%, slightly higher than at room temperature. The low gain chip was excluded from the analysis. These fitted gains have been used to normalise the measured charge collection efficiency.

Figure 4-17 shows the CCE (runs 590 to 597) associated to a cluster of two, four, six or eight strips around the impact point of the track for four different regions of the irradiated detector, corresponding to different radiation doses. On the *n*-side (squares) the charge is always focused on a small number of strips, even when the CCE decreases going from the least (a) to the most (d) irradiated region. This is not the case for the *p*-side. As the CCE decreases, the more the charge is spread over many strips and even the 8-strip cluster does not contain it all. The solid line is the one-parameter fit to Equation (4-5) assuming $CCE = (W/d)^2$. The dashed line shows the result of a two parameters fit, where the depletion depth W and the absolute CCE were allowed to vary independently. The results of the two fitting procedures are very similar and indicate that the model provides a very good description of the data points.

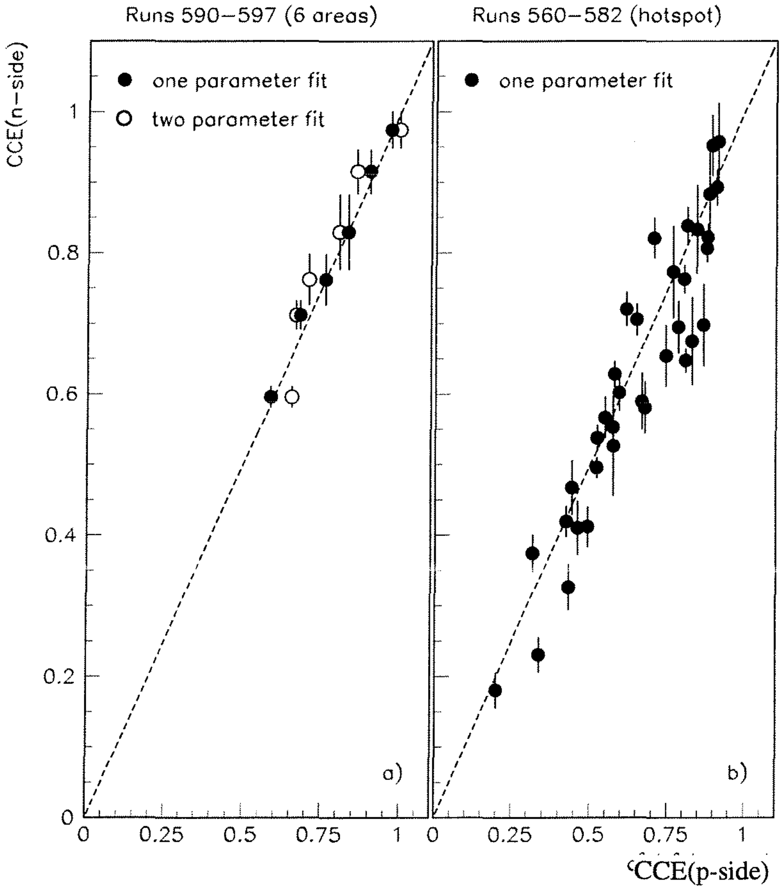

Figure 4-19: CCE measured on the n-side versus CCE determined from the cluster shape on the p-side. The results illustrated in these plots are explained in the text.

In the following of this chapter, the measured CCE will be always intended as determined adding the charge collected in eight-strip clusters. Figure 4-18 shows the normalised CCE of the two DELPHI detectors for runs 590 to 597. Each box in the plot correspond to a section 2.5 mm^2 of the plaquettes. The reference plaquette was found to be fully efficient in all regions, showing that the analysis method is reliable. The irradiated plaquette shows an area of reduced CCE, centred close to the nominal maximum position of the irradiation.

Figure 4-19 shows the CCE measured on the n-side as a function of the CCE determined from the fit to the cluster shape on the p-side. The left plot was obtained from runs 590 to 597 and dividing the irradiated detector in 6 regions of different accumulated radiation dose. The full circles are the results of the one-parameter fit, while the open circles are obtained from the two-parameter fit procedure. The right plot shows only the one-parameter fit results for the most irradiated region of the detector in runs 560-568, 571-577, 581 and 582. Since the CCE changed with time during these runs (see below), the fitting procedure was repeated separately for each half of the run. All data are distributed along the dashed line, indicating that indeed the charge collection inefficiency is only due to partial depletion.
As observed with single diodes, also in the case of microstrip detectors the CCE shows a time dependence.

Figure 4-20 shows the measured CCE on the n-side (full) most irradiated region as a function of time. The CCE on the p-side (dashed) as determined from the model is also shown. These results clearly indicates that the time evolution of the CCE is related to a time evolution of the depletion layer (and therefore of the space-charge density) in the detector.

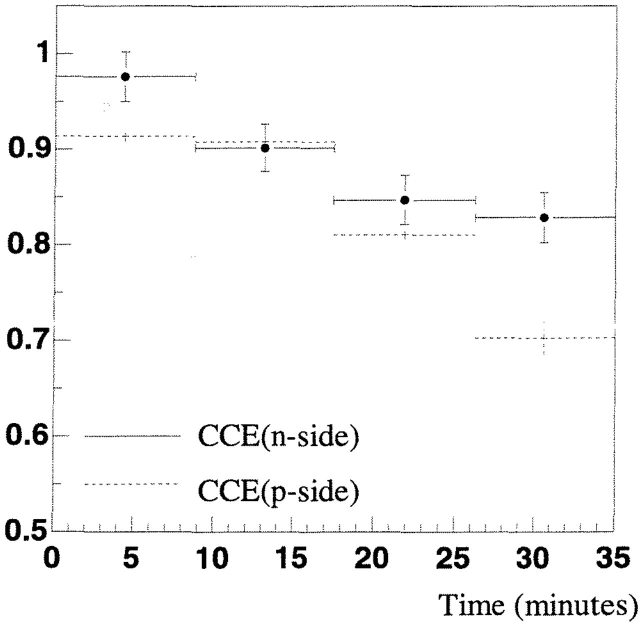

Figure 4-20: CCE of the most irradiated region as a function of time (runs 564 and 565).

4.4.4 Reverse bias operation with charge injection

During the runs 569, 570, 578 and 579, at the lowest bias voltage of around 10 V, a significant forward current developed as measured in the bias line of the irradiated detector (see Table 4-3). After the beam test, this forward current was reproduced and investigated in the laboratory.

The DELPHI module contained 16 channels, randomly distributed over the detector, with a DC connection between the readout line and the implant on the *n*-side of the plaquette closest to the ceramic (see Figure 4-21). These defected readout lines had been disconnected from the chip before the test beam, and were thus at the potential of the bias voltage of this plaquette, which has been always kept at 60 V throughout the test beam. Due to the daisy-chained configuration, these strips were also connected to the *p*-side readout lines of the irradiated plaquette. During the test beam, in between runs 560 and 569, a DC connection between the *p*-implants and their readout lines for these 16 channels developed on the irradiated plaquette. As a result, these *p*-implants were not at ground potential anymore, but at a potential lower than 60 V, depending on the current flowing in the channel and the resistivity of the node. When the bias voltage of the irradiated plaquette was below 20 V, the defected 16 channels were forward biased.

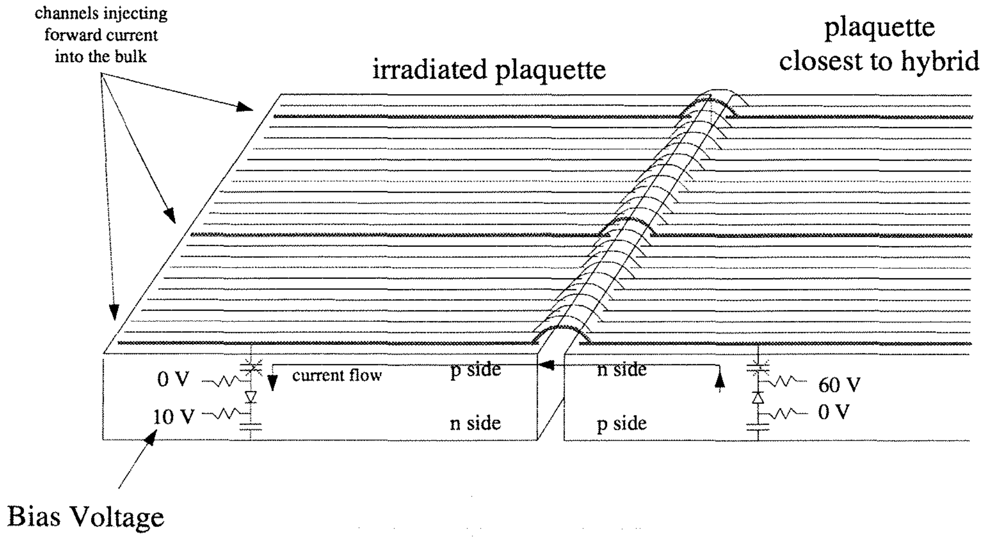

Figure 4-21: Schematic of the charge injection mechanism due to bad channels in the daisy-chained plaquettes.

The remarkable result is that the CCE for these four runs show no significant dependence on temperature or time. Furthermore, the CCE values for the *p*-side are above 75% also for temperatures above 140 K. This could be due to the fact that the accidentally injected forward current (~1 μA) caused a space charge compensation, which lowered the necessary depletion voltage. This phenomenon can be considered as the analogous of the light illumination for single diodes. However, there is no explanation for the discrepancy between the CCE of the *n*- and *p*-side.

4.4.5 Position resolution results

For the study of the position resolution we selected a data sample where the CCE was stable in time (runs 590-597). The residual distributions between the track extrapolation and the cluster in the DELPHI detector were fitted with a Gaussian function. For this study, and thanks to the available large statistics, we divided the detector in 16 equally populated areas with different CCE.

Figure 4-22 shows the spatial resolution as measured on the *p*-side (left) and *n*-side (right) of these 16 areas as a function of the measured CCE. The precision on the track extrapolation at the position of the DELPHI detectors was 16.9 ± 0.4 μm in both transverse coordinates. The resolution of the reference detector has been measured to be ~5 μm on the *p*-side and ~19 μm on the *n*-side, as expected from the strip pitch.

Concerning the irradiated detector, the resolution on the *n*-side was ~12 μm, while one would expect around 9 μm for a 42 μm strip pitch. This value does not depend on the CCE. This result is in agreement with the fact that the detector depletes from the *n*-side.

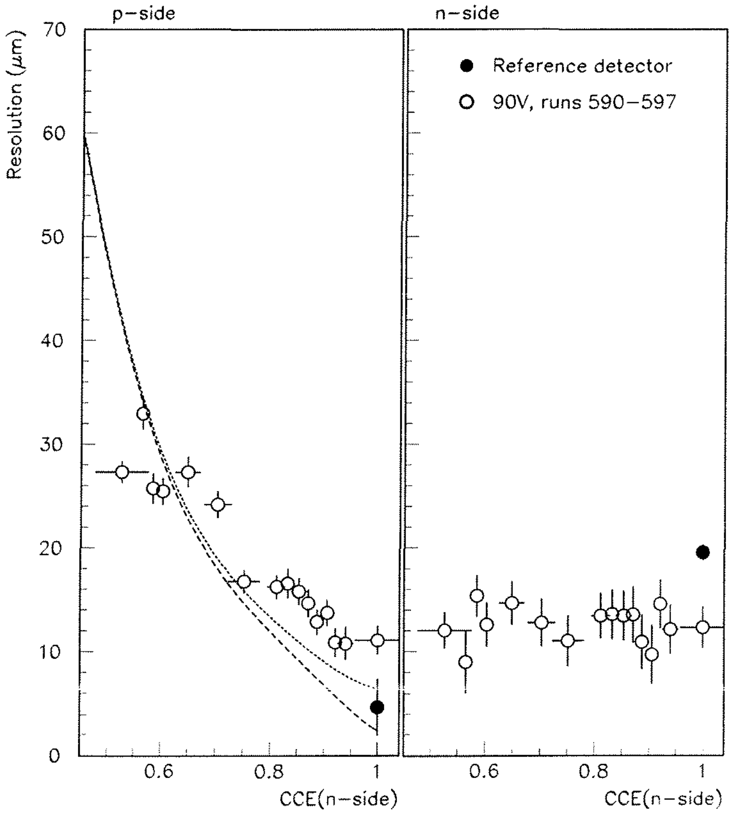

Figure 4-22: Position resolution for the p-side (left) and the n-side (right), as a function of CCE. Note that the pitch of the n-side of the reference detector is twice as large as that of the irradiated detector.

The resolution on the *p*-side of the irradiated detector depends strongly on the CCE. The dashed line in the plot is the prediction from the cluster shape model. As it can be seen from the figure, the model describes quantitatively quite well the dependence of the resolution on the CCE, except when the detector is fully depleted. This is because the simulation does not attempt to model the electric field lines, and assumes all tracks to be perpendicular to the surface of the detector. As a result it overestimates the resolution for fully depleted detectors. The dotted curve tries to take this problem into account adding a 6 μm smearing.

Figure 4-23 shows the resolution as a function of the CCE for different bias voltages. In the case of the special runs with charge injection, the resolution on the *p*-side does not depend on the CCE and it is, in fact, not in agreement with the model.

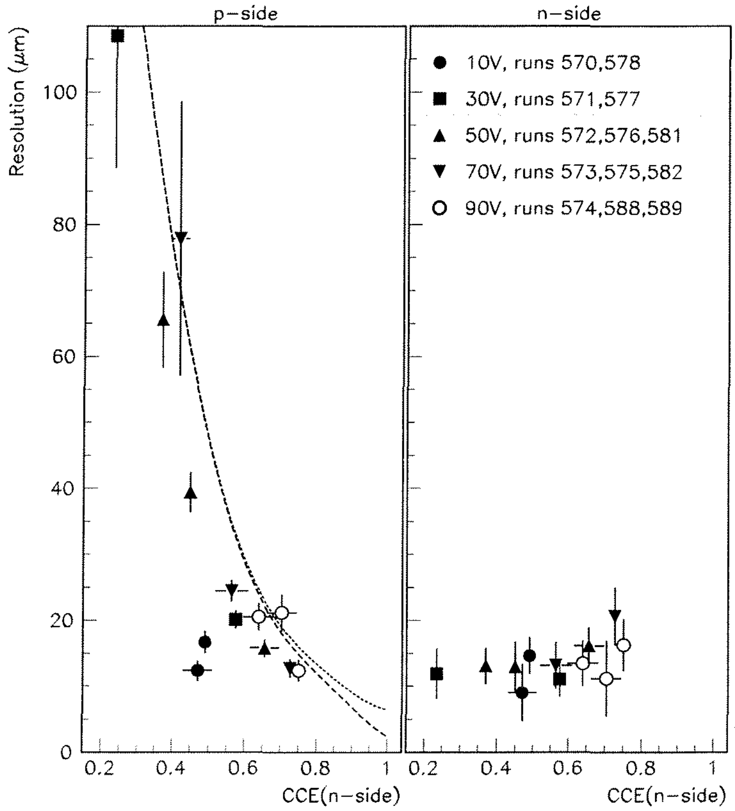

Figure 4-23: Position resolution in the most irradiated region for the p-side (left) and the n-side (right), as a function of CCE for different bias voltages.

References

[1] The Large Hadron Collider project: http://wwwlhc01.cern.ch/

[2] V.G. Palmieri, K. Borer, S Janos, C. Da Viá and L. Casagrande, Nucl. Instr. and Meth. in Phys. Res. A 413 (1998) 475

[3] Z. Li and H.W. Kraner, IEEE Trans. on Nucl. Sci. NS 38 (1991) 244

[4] L. Beattie et al., Nucl. Instr. and Meth. in Phys. Res. A 412 (1998) 238

[5] ATLAS Technical Proposal, CERN-LHCC/97-39, vol. II, p. 421

CMS Technical Proposal, CERN-LHCC/94-38, p. 39

[6] ATLAS Internal Note INDET-NO-203, 1998

[7] A. Ruzin et al., *Radiation hardness of Si detectors processed on various oxygen enriched wafers*, Rose Meeting, CERN-LEB 99-8

[8] D. Meier et al. (RD42 collaboration), “Development of CVD Diamond Radiation Detectors”, 5th Symp. On Diamond Materials, Proc. Electrochem. Soc., Paris 1997

[9] B. Dezillie et al., IEEE Trans. on Nucl. Sci. NS 46 (1999) 221

[10] V. Eremin et al., Sov. Phys. & Techn. of Semiconductors 8 (1974) 1157

[11] K. Zdansky et al., J. Appl. Phys. 79 (1996) 3611

[12] B.K. Jones et al., Nucl. Instr. and Meth. in Phys. Res. A 395 (1997) 81

[13] G. Lutz, Nucl. Instr. and Meth. in Phys. Res. A 377 (1996) 234

[14] A. Chilingarov and T. Sloan, Nucl. Instr. and Meth. in Phys. Res. A 399 (1997) 35

[15] V. Chabaud et al., Nucl. Instr. and Meth. in Phys. Res. A 368 (1995) 314

Chapter 5

Radiation hardness of readout electronics

Radiation tolerance of integrated circuits is a primary concern in future high-energy physics experiments. In particular, pixel detectors are often placed as close as possible to the interaction point of the experiment and hence require high radiation tolerance. As the area taken by the readout electronics defines the pixel size, a high device density is necessary. Although radiation hard technologies exist, they do not always provide adequate device density. This was the main motivation to investigate the radiation tolerance of standard sub-micron technologies.

Radiation effects can be classified in total-dose ionising radiation damage, single-event errors, and displacement damage. The later case is not of interest for this work, because it is a concern primarily only for minority carriers (e.g. bipolar) and opto-electronic devices, while it is relatively unimportant for MOS transistors, which is the technology chosen for the pixel detectors this thesis is concerned with.

5.1 Radiation damage in MOS devices

The structure of an n-channel and p-channel MOS (metal-oxide-semiconductor) transistor is shown in Figure 5-1. The n-channel transistor is formed with two heavily doped n+ regions diffused into a lighter doped p-type substrate. The two n+ regions are called *source* and *drain*. At the surface between the source and drain lies a *gate* electrode that is separated from the silicon bulk by a thin dielectric material (silicon dioxide). The p-channel device is realised in a similar way, with source and drain diffused in an n-well this time.

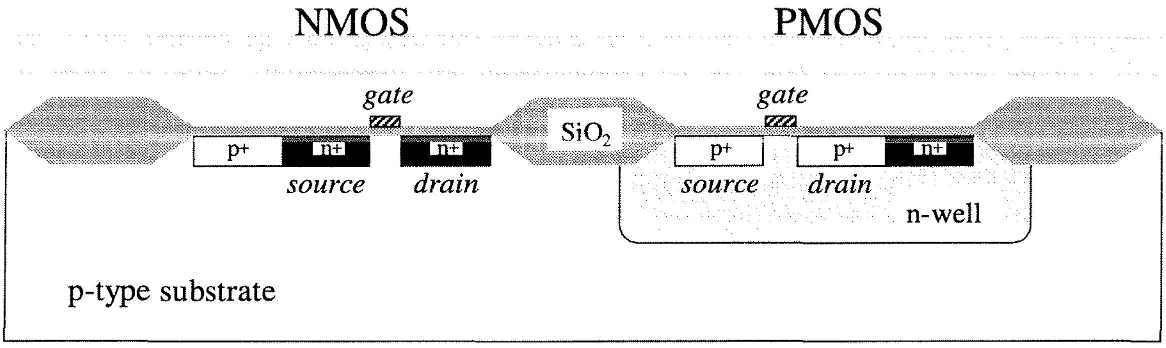

Figure 5-1: Schematic of the CMOS technology.

Let us briefly recall the operation of the MOS transistor, using as example the NMOS case. When a positive potential is applied to the gate with respect to the source, positive charge accumulates on the gate and negative charge in the substrate under the gate. When the gate voltage reaches a value called *threshold voltage* (V_T), the substrate underneath the gate becomes inverted, i.e. it changes from p-type to an n-type semiconductor.

Consequently, an n-channel exists between the source and drain that allows carriers to flow.

When high-energy ionising radiation traverses a MOS transistor, electron-hole pairs are uniformly generated throughout the oxide. The generated carriers induce build-up of charge, which can lead to device degradation. The mechanisms by which the degradation occurs are depicted in Figure 5-2, representing a MOS band diagram for a positively applied gate bias.

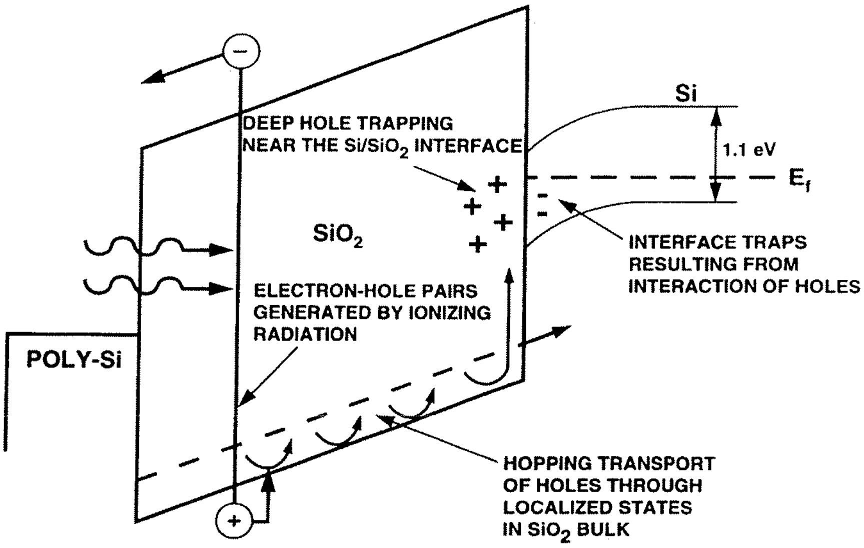

Figure 5-2: Illustration of radiation-induced charge generation in MOS devices. Here is depicted the band diagram when a positive gate bias is applied [1].

If an electric field exists across the oxide of a MOS transistor, once generated, electrons in the conduction band and holes in the valence band will immediately begin to travel in opposite directions [1]. Normally, electrons are extremely mobile and are swept out of the silicon dioxide in picoseconds. However, some fraction of electrons will recombine with holes before they can leave the oxide. The amount of initial recombination depends on the electric field across the oxide and on the energy and type of incident radiation. In general, strongly ionising particles form dense columns of charge where the recombination rate is high compared to the case of the relatively isolated charge pairs, generated by weakly ionising particles. Figure 5-3 shows the holes yield as a function of the applied electric field for different type of radiation.

When a hole moves through the SiO$_2$, its own charge causes a distortion of the local potential field of the lattice, which tends to trap the hole. As a hole travels, the distortion follows the hole. This increases the effective mass and decreases the mobility of holes. Hole transport is thus dispersive and highly dependent on temperature and oxide thickness. In presence of moderate electric field, holes are basically immobile at low temperature, while at room temperature they move out of the oxide in milliseconds [2].

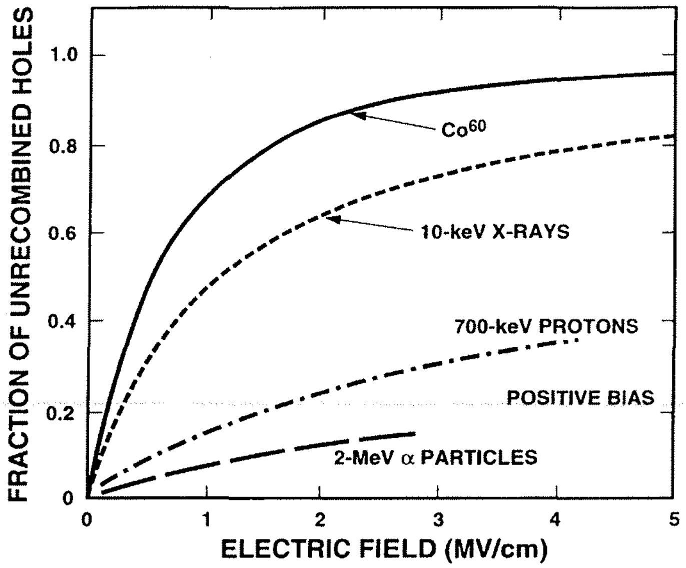

Figure 5-3: Charge yield as a function of the applied electric field for different type of radiation [1].

As the holes approach the interface, some fraction will be trapped, forming a positive *oxide-trap* charge. A large concentration of oxide-trap charge can cause the increase of leakage current in the integrated circuit. Furthermore, hydrogen ions are likely to be released as holes hop through the oxide or as they are trapped near the Si/SiO_2 interface. The hydrogen ions can drift to the interface where they may react to form *interface traps*. A large concentration of interface-trap charge can decrease the mobility of the carriers and increase the threshold voltage of n-channel transistors. In the following sub-sections some details of oxide-trap and interface-trap charge build-up will be given.

5.1.1 Oxide traps

Close to the Si/SiO_2 interface, there are a large number of oxide vacancies (due to the out-diffusion of oxygen in the oxide and lattice mismatch at the surface), which can act as trapping centres. As holes approach the interface, some fraction of them will become trapped. The positive charge associated with the trapped holes causes a negative threshold-voltage shift, for both n- and p-channel transistors.

Immediately after oxide-trap charge is created it begins to be neutralised (annealing), due to two mechanisms: (1) the tunnelling of electrons from the silicon bulk into oxide traps, and (2) the thermal emission of electrons from the oxide valence band into oxide traps. The tunnelling is independent of the temperature, but varies exponentially with the distance of the trap from the Si/SiO_2 interface. On the contrary, trap neutralisation by thermal emission depends exponentially on the temperature and the trap energy, but it is independent of the position of the trap. Annealing is normally faster for higher applied gate bias. What has been also observed [3] is that the neutralisation is reversible. In fact, if the gate bias is inverted after annealing, some fraction of the oxide traps becomes active again.

5.1.2 Interface traps

In addition to oxide traps, radiation induces also interface traps at the Si/SiO2 interface. Because of their location at the interface, applying an external bias can easily change the charge of an interface trap. In a p-channel transistor, interface traps are mainly in the lower region of the band gap (i.e. they are donor traps). Therefore they are predominantly positive, causing a negative threshold-voltage shift. Conversely, in the case of an n-channel transistor, since the traps are mainly acceptors and therefore negative, they cause a positive threshold-voltage shift. Because oxide-trap charge is always positive for p- and n-channel transistors, oxide-trap charge and interface-trap charge compensate each other for n-channel transistors, and add together for p-channel transistors.

Several models have been proposed, which try to explain the properties of interface-trap charge build-up. The model, which better agrees with the available experimental results, is the one of Shaneyfelt et al. [4]. According to this model, for positive bias during irradiation, holes travel towards the Si/SiO_2 interface, where they can be trapped. The energy released is sufficient to break Si-H bonds. The hydrogen ions, which transport to the interface, interact breaking more Si-H bonds to form H_2 and interface traps.

The build-up of interface-traps occurs on a much slower time scale than oxide traps. Unlike oxide traps, interface-trap charge does not anneal at room temperature. These properties make interface-trap charge effects more important for low dose-rate applications. There is an *early* build-up, which takes place seconds to hours after a pulse of ionising radiation [5]. This long time is due to the time it takes for the hydrogen ions to drift to the Si/SiO2 interface. Of course, little or insignificant build-up of interface traps occurs while applying a negative bias, which moves the ions away from the Si/SiO2 interface.

The rate at which interface traps build up depends on the temperature and on the applied field. At low temperatures (< 150 K), the build-up is significantly retarded [6]. For low dose-rate applications, the temperature during irradiation can have a large impact on the number of radiation-induced interface traps. On the contrary, the dependence on the temperature is negligible with a gate bias of zero volts. This bias can lead to a large imbalance in the threshold voltage for ON and OFF transistors.

A second build-up of interface traps can occur a long time after irradiation (> 1 month) and can be quite significant. This *latent* build-up can increase the interface-trap charge density to levels as much as four times higher than the *early* charge density. Two possible mechanisms for the latent build-up have been proposed [7]. The first is direct conversion of oxide traps into interface traps, due to electron tunnelling from the silicon bulk into oxide-traps. As the electron anneal the oxide trap, a hydrogen ion can be released and form an interface trap. A second possible mechanism is due to the release of hydrogen atoms during irradiation in an adjacent structure and the diffusion of the atoms to the Si/SiO_2 interface.

5.1.3 Device properties

The total threshold-voltage shift for a transistor is the sum of threshold-voltage shifts due to oxide-trap and interface-trap charge:

$$\Delta V_{th} = \Delta V_{ot} + \Delta V_{it} \tag{5-1}$$

ΔV_{ot} and ΔV_{it} can be determined from

$$\Delta V_{ot,it} = -\frac{1}{C_{ox} \cdot t_{ox}} \cdot \int_0^{t_{ox}} \rho_{ot,it}(x) \cdot x \cdot dx \tag{5-2}$$

where $\rho_{ot,it}(x)$ is the charge distribution of the radiation-induced traps. For positive charge, the threshold-voltage shift is negative and viceversa. Thus, for devices where the oxide-trap charge dominates, the threshold-voltage shift will be predominantly negative.

At high dose rates and short times, little annealing of oxide traps will occur and ΔV_{ot} can be large and negative, while interface-trap charge will have had insufficient time to build up and ΔV_{it} is small. Thus, for either n- or p-channel transistors the threshold-voltage shift can be large and negative.

At moderate dose rates, some neutralisation of oxide-trap charge will take place and some build-up of interface traps will also occur. Thus, for this case, both ΔV_{ot} and ΔV_{it} can be large. For an n-channel transistor, ΔV_{ot} and ΔV_{it} tend to compensate each other.

For the long times associated with low dose-rate irradiation, a large fraction of the oxide-trap charge will be neutralised during irradiation. Thus, ΔV_{ot} is normally small. In contrast, interface traps are saturated. This results in a positive increase in the threshold voltage in n-channel transistors and a decrease in carrier mobility, which tend to reduce the current drive of a transistor and can lead to timing related failures.

5.1.4 Gate and field oxides

The general trend in commercial MOS devices is towards ultra-thin oxides. In fact, the amount of interface and oxide traps decreases with a quadratic dependence on the oxide thickness t_{ox}. For thickness less than 20 nm there is evidence that the amount of radiation induced traps decreases with even a faster dependence on the oxide thickness.

The basic mechanism of radiation effects in ultra thin oxides is different from those of moderately thick oxides. We have mentioned the neutralisation of oxide-trap charge by electron tunnelling. If the oxide thickness is small enough, all the oxide traps are close enough to the interface and become neutralised. Irradiation measurements on MOS capacitors [8,9] have shown a significant decrease of the radiation induced trapped oxide charge and interface states for oxides thinner than about 10 nm. Gate oxides in present day sub-micron CMOS technologies are in this range. Recent measurements on transistors implemented in these technologies confirm the significant reduction in radiation induced transistor parameter shifts [10].

In commercial technologies there is the problem of the field oxides, which are much thicker than gate oxides (typically 200 nm to 1000 nm). A cross-section of a typical commercial field oxide is shown in Figure 5-4. If the radiation induced oxide charge in a field oxide is large enough excessive leakage current can flow from the source to the drain of the transistors and between transistors. Since the oxide trap charge is always positive, this problem occurs only for n-channel devices. The field-oxide leakage current is present also when the gate voltage is zero volts thus preventing the transistor from being completely switched off. This will greatly add to the static supply leakage current of an integrated circuit, increasing the overall power consumption.

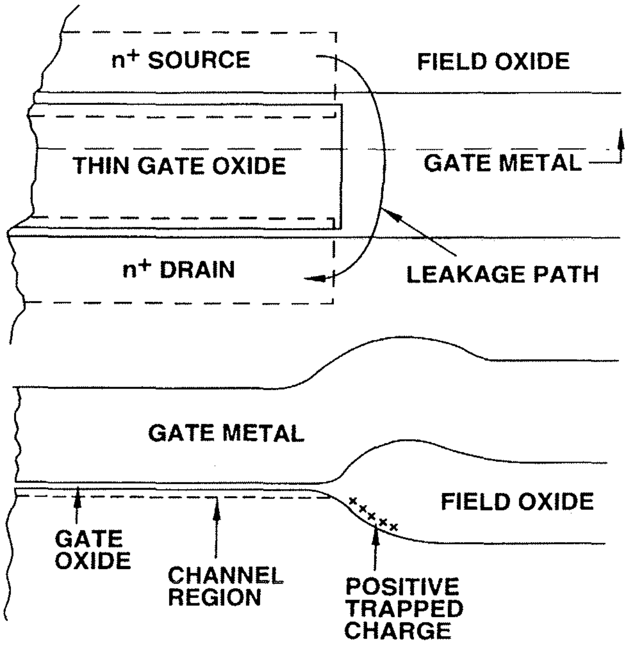

Figure 5-4: Cross section of a parasitic field oxide transistor showing the primary leakage current paths.

Source-to-drain leakage can be avoided by using closed gate structures. Inter-transistor leakage is eliminated by implementing systematically p^+ guard rings around n^+ diffusion regions. The effectiveness of this layout approach has been extensively proven for transistors in many technologies [10] and is further discussed in Section 5.3. Although some penalty has to be paid in terms of component density, it is still possible to achieve much higher densities in deep sub-micron technology than is possible using radiation hard technologies.

Having established that individual transistors can be radiation tolerant, it remained to prove that it was possible to design a full circuit using such layout techniques. This was achieved in a test chip implemented in a commercial 0.5 μm CMOS technology (t_{ox} = 10 nm). The results of this test chip are discussed in Section 5.4. Although the chip was radiation tolerant up to ~1 Mrad, the density penalty of the special layout techniques proved to be too large. Therefore, a new test chip was developed, following the same approach, in a 0.25 μm CMOS technology (t_{ox} = 5 nm), which is intrinsically denser and more radiation hard. Section 5.5 reports on the performance of this test chip and its radiation tolerance.

In the contest of this work, we have also tested the radiation tolerance of the LHC1 readout chip, which is discussed in Section 5.2. Even if it was not expected to be radiation hard, the final dose it could stand was of interest to understand whether it was possible to have an early physics run using such a detector. This test also represents a reference point to show the improvements achieved with the two following prototype chips.

5.2 Irradiation of the LHC1 pixel readout chip

The LHC1 readout chip has been extensively described in Chapter 3. It is worth reminding that the chip has been produced in a commercial 1 μm CMOS technology. The chip was continuously irradiated under bias with a collimated ^{90}Sr beta source (370 MBq).

The source was placed at 12 mm from the chip. At this distance, a dose rate of 2.2 krad per hour has been measured with a thermo-luminescent foil. The error on the measurement has been estimated to be of the order of 10%. Since the source was very close to the chip, only the part directly exposed to the exit of the collimator was irradiated. We have positioned the source in such a way that less than half of the chip was irradiated, up to a dose of ~100 krad.

During the irradiation, we have continuously monitored the five bias currents (I_{th}, I_{bias}, I_{comp}, I_{dl} and I_{dla}) and the analog power supply of the chip (the digital one could not be monitored because of the PCB design). Moreover, we performed periodically the following tests to check the status of the chip:

- measurement of the number of noisy pixels;
- injection of a test pulse to detect dead or inefficient pixels;
- delay and threshold scan to check variation of basic operating parameters;
- reading and writing of known patterns in the test, mask and delay registers, to detect errors in the digital part of the circuitry.

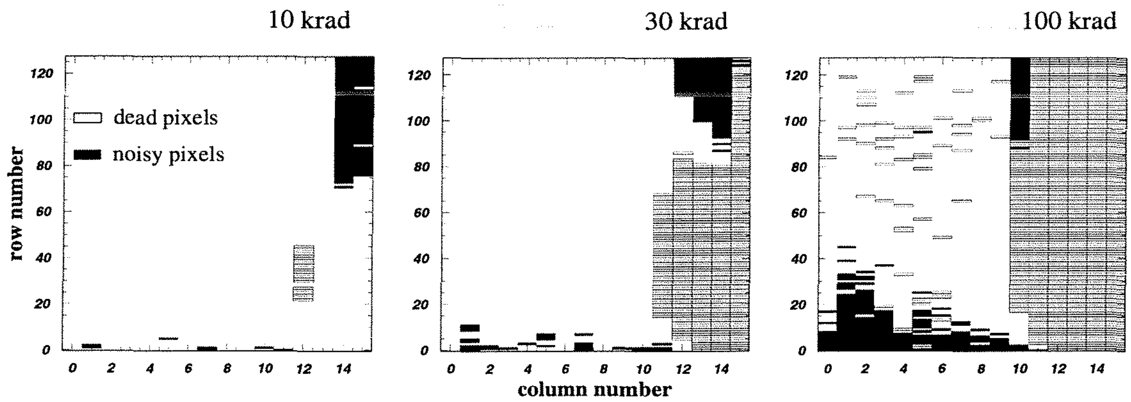

Figure 5-5: These plots represent the chip status after different doses. Each box corresponds to a bad pixel. The black boxes are the noisy pixels; the white boxes are the dead ones. The source was positioned in such a way that only the right part of the chip was irradiated.

All bias currents remained unchanged till the end of the test. Figure 5-5 illustrates the evolution of the status of the chip through different doses. It is clear that already after 10 krad there are about 150 bad pixels among dead and noisy channels. After 30 krad errors in the mask and test registers started to appear. The main consequences were that some pixels were masked even if no mask map is loaded, and at the same time those pixels could not be pulsed. No errors have ever been observed in the delay adjust registers.

Figure 5-6 shows the delay (left) and the threshold (right) scan at different doses. Apart from the decreased efficiency due to the bad pixels, there is a clear a shift of the best operating point of the chip.

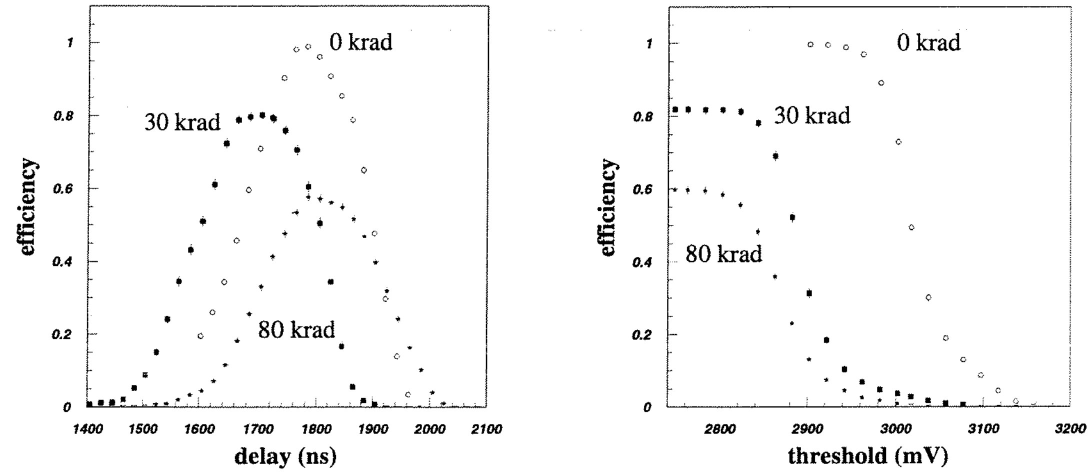

Figure 5-6: Delay (left) and threshold (right) scan for all pixels at different doses.

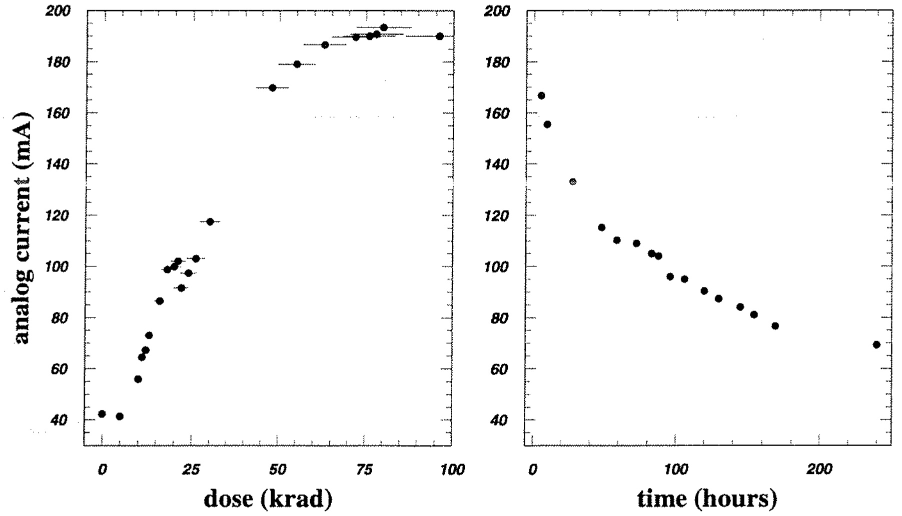

Figure 5-7: Analog power supply current during irradiation (left) and annealing (right).

Figure 5-7 (left) shows the current of the analog power supply as a function of the accumulated dose. A saturation effect is observed after ~70 krad. In Figure 5-7 (right), one can see how the power consumption decreases due to annealing (at room temperature) after the irradiation is stopped.

These results clearly show that the LHC1 pixel readout chip, manufactured in commercial 1 μm CMOS technology, undergo a substantial degradation of its performances at relatively low doses of beta-radiation (around 10 krad). This degradation was mainly expressed in sharp increase of power consumption and rising amount of noisy and non-responding pixels.

5.3 Enclosed layout approach on single transistor

As discussed in Section 5.1, radiation induces accumulation of positive charge in the silicon oxide. This positive charge can lead to the formation of an inversion layer in the p-type substrate (or p-well in the case an n-type substrate is used). In the case of NMOS transistors, this leads to source-to-drain leakage and inter-transistor leakage between neighbouring n+ implants. Source-to-drain leakage can be avoided by forcing all source-to-drain current to run underneath gate oxide by using a closed gate. This is illustrated in Figure 5-8, where (a) is a top view and (b) is a cross-section along the line AA'. The two NMOS transistors shown in the figure are drawn in closed geometry, and any current between their sources and drains has to flow underneath the gate. In this way there is no current path possible underneath the field oxide.

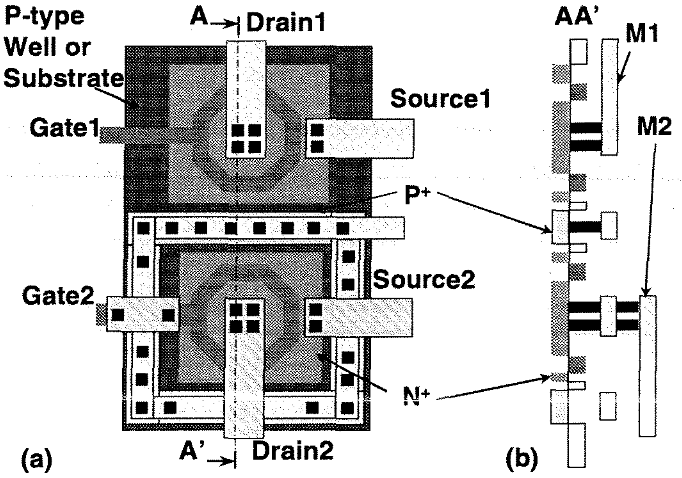

Figure 5-8: Transistors laid out in enclosed geometry to prevent transistor leakage. The implementation of p+ guard ring prevents leakage between the two transistors. (a) top view; (b) cross-section along the line AA'.

Inter-transistor leakage (from one n+ diffusion to the next) is also caused by the formation of an inversion layer in the p-type substrate underneath the field oxide. This can be avoided implementing an uninterrupted p+ guard-ring, which separates the n+ implants. This is again illustrated in Figure 5-8, where the two NMOS transistors shown in the figure are isolated from each other by completely enclosing one of them by a p+ guard-ring. The p+ guard-ring ensures a doping level such that the positive charge generated in the oxide is no longer sufficient to invert the silicon at the Si-SiO_2 interface.

It is worth mentioning that this type of precautions is not required for PMOS transistors. In this case, the positive charge accumulated in the oxide can not lead to the formation of any inversion layer in the n-well (or n-substrate).

X-ray irradiation tests were performed on individual transistors to verify the effectiveness of these layout techniques. The X-ray energy was 10 keV, the dose rate was 4 krad/min, and the devices were biased in worst case condition during the room temperature irradiation. The measurements were carried out immediately after the irradiation.

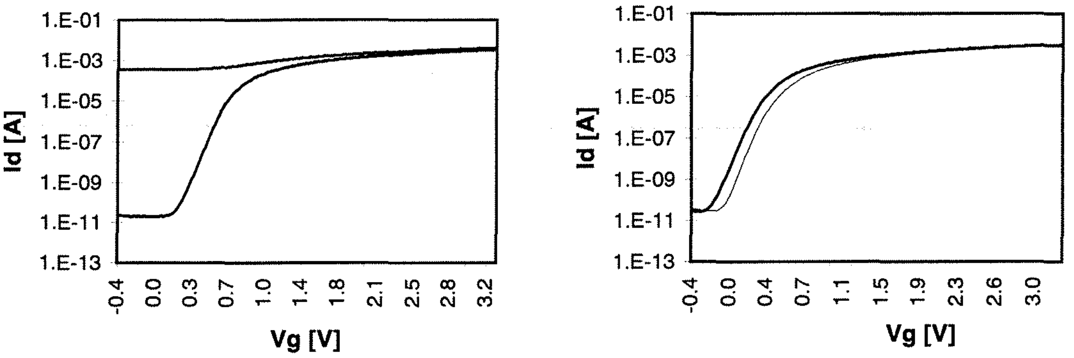

Figure 5-9: Id versus gate voltage before (lower curve) and after (upper curve) irradiation for: (left) a traditionally laid out transistor, showing a prohibitive increase of the leakage current after 40 krad, and (right) an enclosed transistor, which shows a negligible increase of the leakage even after 2 Mrad.

Figure 5-9 shows the major difference in behaviour between a standard and an enclosed transistor in a 0.5 μm technology (gate oxide thickness ~10 nm) after a 2 Mrad exposure. The standard transistor shows unacceptable leakage, and it was verified in a separate measurement that this leakage is already present after only ~40 krad. The enclosed device remains acceptable up to 2 Mrad and only shows a slight change in the threshold slope.

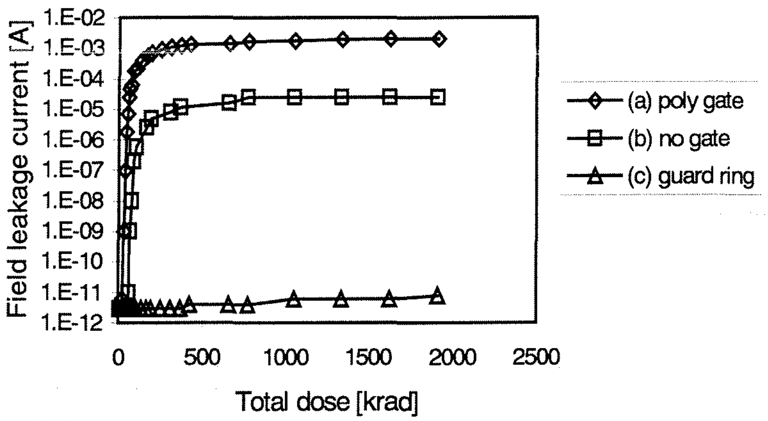

Figure 5-10: Comparison of the field leakage for different cases: (a) field covered with polysilicon gate but no guard-ring, (b) without gate nor guard-ring, and (c) with guard-ring only. The guard-ring completely eliminates this leakage.

Figure 5-10 compares the field leakage (leakage between two n+ diffusions, one biased, the other connected to ground) for three different cases: (a) n+ diffusions separated by field oxide covered with polysilicon; (b) n+ diffusions separated by field oxide not covered with polysilicon; (c) n+ diffusions separated by field oxide, interrupted by a p+ guard-ring. In the case of (a) and (b) leakage starts after 70 krad and 30 krad, respectively, while in case (c) no leakage is observed even after 2 Mrad.

Single event upset (SEU) has not been investigated.

5.4 The Alice1Test prototype readout chip

Th Alice1Test prototype pixel readout chip has been developed in a commercial 0.5 μm CMOS technology. Its radiation tolerance was enhanced by designing all NMOS transistors in enclosed geometry and introducing guard-rings wherever necessary (see previous section). The circuit is a matrix of 65 by 2 identical pixel cells each measuring 50 μm x 420 μm. A block diagram of the pixel cell is shown in Figure 5-11.

Each cell comprises an input structure (160 μm long) to simulate a single detector element, a preamplifier, a shaper, a comparator with a variable threshold, and a data flip-flop. The circuit can work both with positive and negative input charges. The preamplifier feedback contains a detector leakage compensation circuit, i.e. a low frequency feedback, which adjusts itself to the leakage current coming from the detector. In order to minimise the noise contribution of large detector leakage currents, the shaping time of the shaper was reduced to 23 ns. The shaper output current is presented to a current comparator. Details about the circuit design can be found in reference [11].

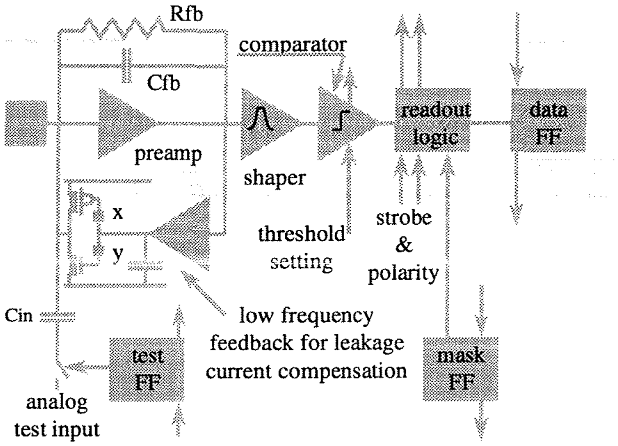

Figure 5-11: Block diagram of the pixel cell. The rectangles labelled 'x' and 'y' in the detector leakage current compensation circuitry are voltage level shifters. They prevent the NMOS and PMOS transistors, which absorb the (detector) leakage, from simultaneously conducting current.

The content of the test flip-flop determines whether or not an analog input signal is applied to the preamplifier input across an injection capacitance. Changing the test flip-flop pattern allows addressing one or several pixels simultaneously in an arbitrary way during testing. A mask flip-flop allows disabling a noisy or completely non-functional pixel. If the comparator output changes polarity when the strobe or trigger signal is high, a “one” is written into the data flip-flop. During readout the data flip-flops of pixels in one column are configured as a shift register for sequential readout. Every cell contains about 200 transistors, the total chip about 25000 in a 10 mm^2 area.

5.4.1 Measurement results prior to irradiation

The injection capacitance could not be calibrated, but only estimated from data on layer to layer capacitance provided by the vendor. All numbers given in absolute electron charge are based on this estimate.

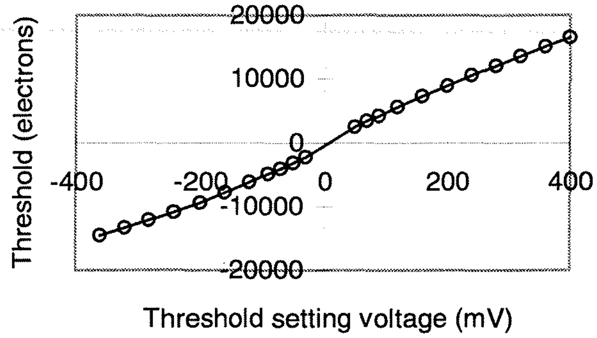

Figure 5-12: Pixel threshold as a function of threshold setting voltage. For thresholds lower than 1500 electrons the noise becomes prohibitive.

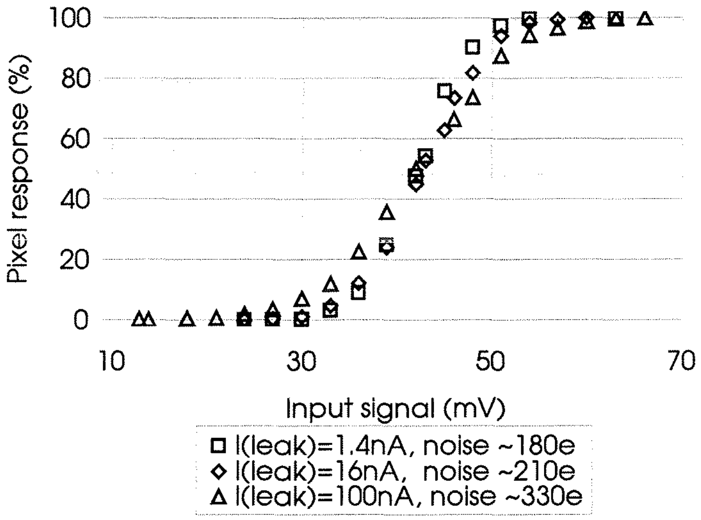

Figure 5-13: Response of one pixel in percent of input signal versus signal amplitude. The threshold practically does not change with increasing leakage current, while the noise increases as expected.

Figure 5-12 shows how the threshold setting voltage can change the average (over all 130 cells) pixel threshold. Figure 5-13 shows how the response of one cell varies for an increasing input charge. The 50 % transition point corresponds to the pixel threshold, and the slope of the curve is a measure of the noise. The threshold did not vary by more than 1% for leakage currents varying from – 200 nA to + 200 nA. The average noise is about 200 electrons rms at low detector leakage current. The input structure adds about 100 fF to the pre-amplifier input to simulate the detector capacitance.

5.4.2 Irradiation measurements

The radiation tolerance of the chip was measured for different irradiation sources. Here we report on the results obtained with X-rays and with minimum ionising particles (in the NA50 experiment). These results show that the circuit performance started to degrade only after a total dose of 600 krad to 1.7 Mrad, depending on the type of radiation.

X-rays

The X-ray irradiation was carried out under the same conditions as in section 5.3. Figure 5-14 left shows the evolution of the average pixel comparator threshold and its rms dispersion with dose. The chip started to degrade significantly only after 600 krad. The large oscillatory changes at low dose are due to significant annealing effects immediately after irradiation (despite the efforts to minimise the measurement time). Figure 5-14 right shows that the analog power consumption remains unchanged and that the digital power consumption decreases. The latter can be explained by the radiation induced transistor threshold shifts. This indicates on a full circuit scale that enclosed NMOS devices and guard rings prevent radiation-induced leakage.

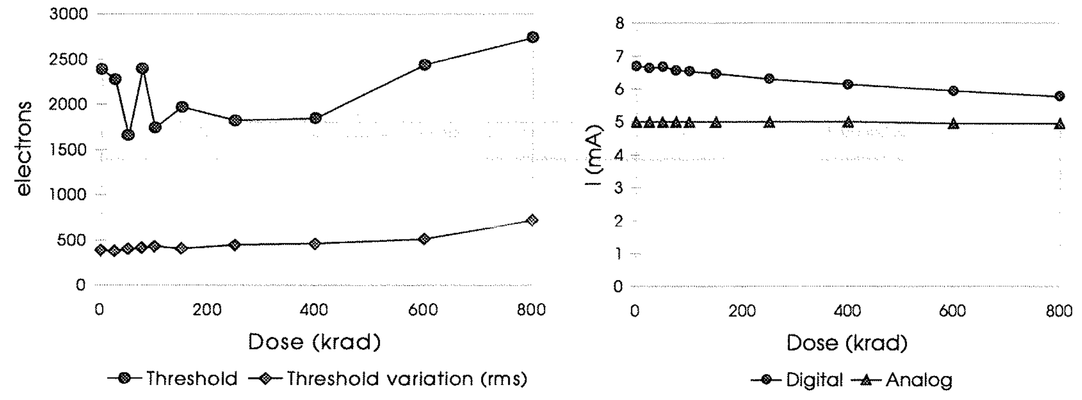

Figure 5-14: Left: evolution of the average comparator threshold and its variation (left) and of the supply currents to the chip with increasing X-ray dose. Significant degradation sets in at about 600 krad.

High energy particle irradiation (electrons)

A chip was placed in the NA50 experiment right behind the target, but slightly offset with respect to the particle beam. This resulted in an irradiation of the chip by mainly electrons with energy of 1 MeV or above. The dose was both calculated by a GEANT [12] simulation and measured using alanine dosimeters placed in proximity of the circuit.

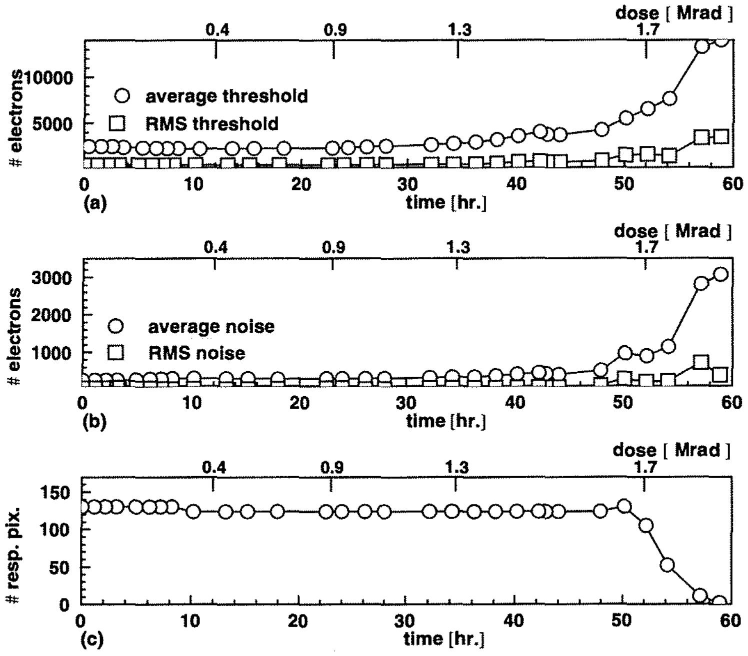

Figure 5-15: Irradiation in the NA50 beam line. Evolution of average and spread of (a) pixel threshold and (b) noise, and (c) number of pixels responding to an input signal below 20'000 electrons as a function of irradiation dose. After 52 hours, corresponding to about 1.7 Mrad, the chip starts to degrade significantly.

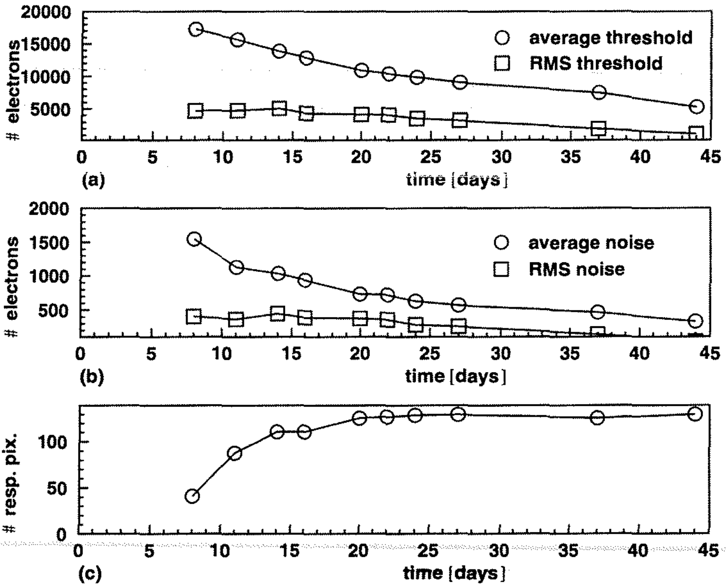

Figure 5-16: Annealing under bias after irradiation. The data points are explained in the previous figure caption. The last week of annealing was carried out at 100 °C.

Figure 5-15 shows the average and rms spread of the threshold (top) and noise (middle), as well as the number of pixels responding below 20'000 electrons (bottom). The drop in number of responding pixels from 130 to 126 and the rise back to 130 is an artefact due to a timing problem in the experimental set-up. The drop to zero after 55 hours is real. The degradation after 1.7 Mrad is evident. Some recovery can be observed immediately after 43 hours due to annealing when the beam was off for a couple of hours. The irradiation was continued up to 2.6 Mrad well beyond the point when no pixels were responding.

Figure 5-16 shows the annealing under bias. After one week at room temperature some pixels started to respond again. After a month at room temperature the average threshold has come down again to about 7500 electrons, and the average noise to about 500 electrons. The last week of annealing was carried out at 100°C and caused the threshold to drop to about 5000 electrons.

These results show how the use of NMOS devices in enclosed geometry and guard rings brought the total ionising dose tolerance of the Alice1Test chip (in standard 0.5 μm CMOS) up to about 0.6 to 1.7 Mrad (depending on the radiation source). These are much higher values than the ones tolerated by its predecessor LHC1, implemented without enclosed transistors and guard rings, which typically shows excessive leakage and power consumption after about 30 krad. The failure mechanism in the Alice1Test chip is no longer the leakage, but the radiation induced transistor V_T shifts [11].

5.5 The Alice2Test prototype readout chip

A prototype pixel readout chip has been developed in a commercial 0.25 μm CMOS process. The chip, named Alice2Test, is a matrix of two columns of 65 identical cells. Each readout cell comprises a preamplifier, a shaper filter, a discriminator, a delay line and readout logic, according to a block diagram similar to the one shown for the Alice1Test prototype (Figure 5-11). The circuit can operate with both positive and negative input charges. As this prototype was not intended for bump-bonding to a detector, an input structure has been added to each cell to simulate detector capacitance, capacitive coupling between pixels, and detector leakage current.

The comparator has a 3-bit threshold fine-adjust. In this chip, it is controlled by a 3-bit bus directly linked to the outside. In future versions the fine adjust will be controlled by flip-flops implemented in the pixel cell. The delay element consists of an 8-bit counter and some control logic. A flag tells the delay control logic which polarity of the comparator output corresponds to a logic one, depending on whether one collects positive or negative input charge. If the comparator fires, the counter in the delay is started. The counter can be pre-set with an arbitrary value, and the carry of the most significant bit is used to generate the end of count signal. If the end of count signal is in coincidence with the externally applied trigger a "one" is written into the data flip-flop.

The content of the test flip-flop determines whether or not an analog input signal is applied to the preamplifier input across an injection capacitance. A mask flip-flop allows the disabling of a noisy or non-functional pixel.

5.5.1 Electrical measurements prior to irradiation

The chip has been characterised electrically prior to irradiation using the analog test input and is found to be fully functional. The injection capacitance could not be calibrated, but only estimated from data on layer to layer capacitance provided by the vendor. All numbers given in electrons are based on this estimate.

The threshold can be adjusted linearly using an external bias voltage from –20'000 e$^-$ to +20'000 e$^-$. The minimum threshold is ~1 500 e$^-$, and is determined by cross talk between the analog and digital parts of the circuit. At this threshold setting the average over all 130 cells is about 1'500 e$^-$ and the spread is 160 e$^-$ rms. The pixel noise is ~220 e$^-$ rms.

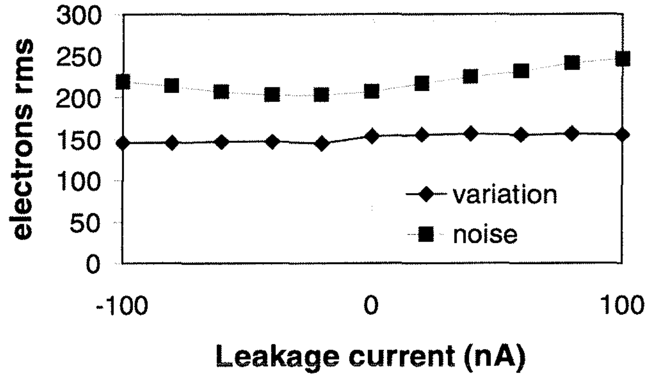

Figure 5-17: Average and spread of pixel noise as a function of the leakage current.

The sensitivity of the circuit behaviour to detector leakage current was measured (see Figure 5-17). There was no change in average threshold for leakage currents of ± 100 nA per pixel. Threshold variation was unchanged and noise degraded by less than 20%.

Pixel detectors normally have a larger capacitance between neighbouring elements than to ground. The input structure has the option of connecting neighbouring pixels together using a 30 fF capacitor or connecting the input node to ground using a 60 fF capacitor. In order to verify the sensitivity of the circuit to capacitive cross-coupling, neighbouring pixels were connected together, the average threshold of the array was set to 1'500 e$^-$ and a pixel was stimulated whilst its neighbour was observed. On average it was necessary to inject 29'000 e$^-$ in one pixel in order to produce a false hit in the neighbour. The measurement was repeated without the coupling capacitors and this time 30'500 e- were necessary for the neighbour to react. This indicates that the front-end is rather insensitive to capacitive cross coupling and that probably much of what was measured was due to parasitic effects in the electrical injection or coupling through power supplies.

As a verification of the threshold adjust circuit the thresholds of all pixels were measured for every value of the 3-bit adjust. Figure 5-18 shows the distribution of the thresholds for (a) minimum added threshold, (b) maximum added threshold and (c) tuned threshold. On this chip the tuning reduced the threshold variation from ~160 e$^-$ rms to ~25 e$^-$ rms. Further refinement of the tuning algorithm may lead to even smaller values of threshold variation.

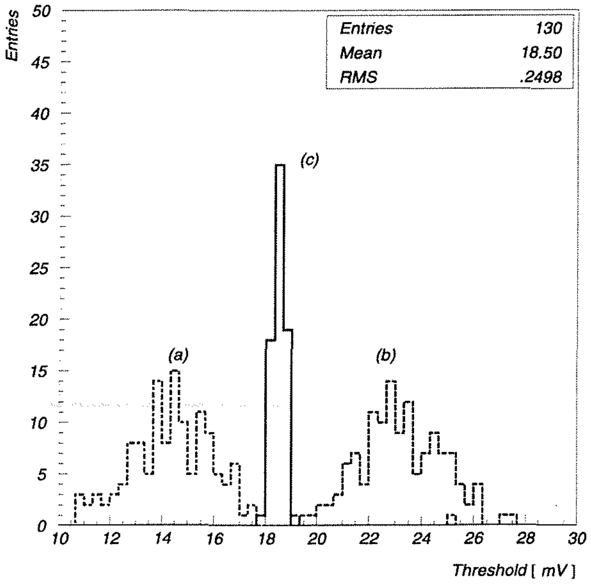

Figure 5-18: Threshold distribution before, (a) minimum and (b) maximum added adjust, and (c) after the threshold adjust.

5.5.2 Irradiation measurements

As a first measurement of the radiation tolerance of the chip, X-ray irradiations were carried out using the same machine used for the previous prototype (see Section 5.4.2). Figure 5-19 shows the evolution of the power supply currents with increasing X-ray dose. The absence of any increase in power consumption with total dose confirms on a full circuit scale that enclosed NMOS devices and guard rings prevent radiation-induced leakage.

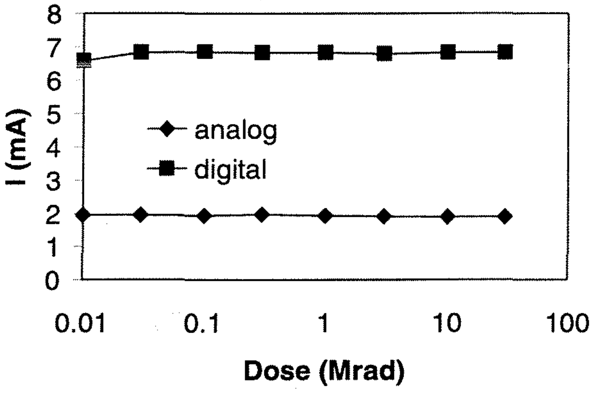

Figure 5-19: Analog and digital power supply currents as a function of the dose. No degradation is visible up to ~30 Mrad.

Figure 5-20 shows the evolution of the average pixel threshold, the threshold variation and pixel noise for the same irradiation. For this particular chip a minor bias adjustment was necessary after 30Mrad to prevent premature signal clipping in the preamplifier. Apart from this all other biases were kept constant. These results illustrate that the chip remains fully functional up to 30 Mrad. After 24 hours under bias at room temperature the parameters were unchanged. Following a subsequent anneal for one week at 100°C the average threshold remained the same, the threshold variation degraded slightly to 190 e$^-$ rms, and the pixel noise returned to 230 e$^-$ rms. Further annealing under bias at room temperature did not affect the circuit parameters.

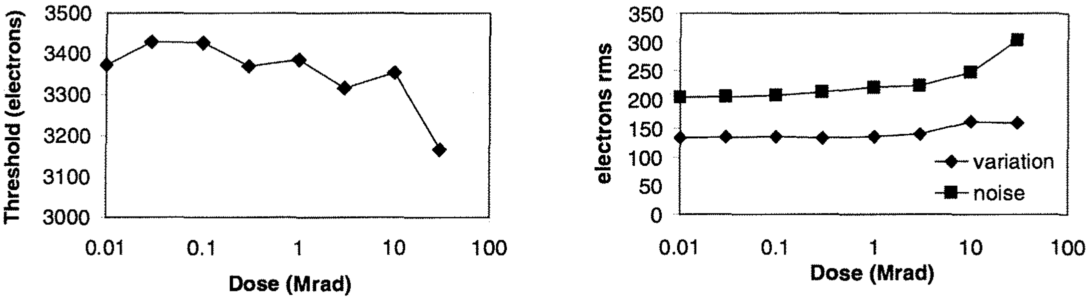

Figure 5-20: (Left) average pixel threshold and (right) average and spread of pixel noise as a function of the dose. No significant degradation is visible after 30 Mrad.

A further test was made with high-energy protons in the NA50 beam line. Figure 5-21 shows a photograph of the chip. The white box indicates the (roughly square) 2×2 mm^2 area where the high intensity beam of 450 GeV/*c* protons was focused. The total dose accumulated by (the irradiated part of) the chip, over a 12-hour period, was 9 x 10^{14} protons/cm^2.

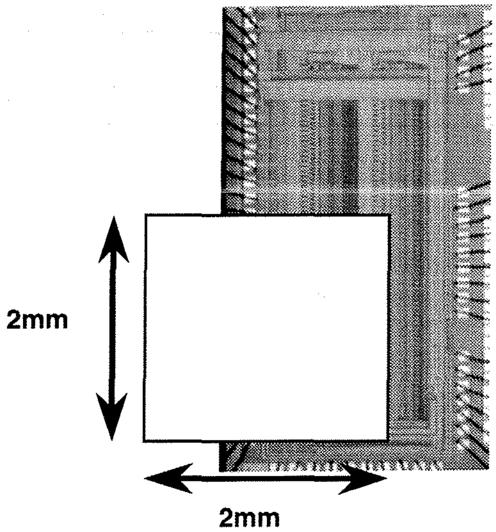

Figure 5-21 A photograph of the chip with the approximate shape and position of the proton beam indicated.

The chip was kept under bias the whole time and read out between spills of the accelerator. During irradiation, the threshold of the hit pixels was reduced and the noise increased to ~1000 electrons rms at the end of the irradiation period. During room temperature annealing, the threshold recovered and even increased slightly, whilst the noise returned to its pre-irradiation value. The pixels outside the target region remained unchanged throughout the test. In addition, there was no increase in power consumption.

In summary, the chip was fully operational after a total dose of 30 Mrad, applied uniformly using an X-ray source and after a very non-uniform exposure to high-energy protons with a total fluence equivalent to 9 x 10^{14} protons/cm^2. This demonstrates that it is possible to make radiation tolerant mixed-mode circuits in a commercial 0.25 μm CMOS process. Although the layout techniques required for radiation tolerance imply some loss in component density, there are still considerable space savings compared with radiation hard technologies. In addition, the cost of using commercial technology should be considerably less than for the specialised radiation hard vendors.

References

[1] F.B. McLean and T.R. Oldham, “Basic mechanisms of radiation effects in electronic material and devices”, Harry Diamond Laboratories Technical Report, HDL-TR-2129, 1987

[2] H.E. Boesch et al, IEEE Trans. Nucl. Sci. NS-25 (1978) 1012

[3] A.J. Lelis et al., IEEE Trans. Nucl. Sci. NS-35 (1988) 1186

[4] M.R. Shaneyfelt et al., IEEE Trans. Nucl. Sci. NS-39 (1992) 2244

[5] J.R. Schwank et al., IEEE Trans. Nucl. Sci. NS-33 (1986) 1178

[6] N.S. Saks et al., IEEE Trans. Nucl. Sci. NS-35 (1988) 1234

[7] J.R. Schwank et al., IEEE Trans. Nucl. Sci. NS-39 (1992) 1953

[8] N. S. Saks, M.G. Ancona, J.A. Modolo, IEEE Trans. Nucl. Sci. NS-31 (1984).

[9] N. S. Saks, M.G. Ancona, J.A. Modolo, IEEE Trans. Nucl. Sci., NS-33 (1986).

[10] F. Faccio et al., "A quarter micron CMOS technology for the radiation environment of LHC," 6th International Conference on Advanced Technology and Particle Physics, Villa Olmo, Como, Italy. October 5-9, 1998, submitted to Nucl. Instr. and Meth A.

[11] W. Snoeys et al., "Layout techniques to enhance the radiation tolerance of standard CMOS technologies demonstrated on a pixel detector readout chip", 8th European Symposium on Semiconductor Detectors, Schloss Elmau, June 14-17, 1998. Nucl. Instr. and Meth. A, in press.

[12] GEANT Detector Description and Simulation tool, CERN Program Library Long Writep W5013

Chapter 6

The NA6i experiment: set-up and physics performance

6.1 Detector concept

The new experiment (hereafter called NA6i), whose preparation is the subject of this thesis, will mainly consist of two detector components: the muon spectrometer presently used in the NA50 experiment and a new silicon vertex telescope, to be placed in the target region inside a dipole magnet. Its several planes of silicon pixel detectors will cover the angular acceptance of the dimuon spectrometer. We also intend to use a cryogenic microstrip beam detector, named *beam-scope*, placed upstream of the target. This detector will measure the transverse coordinates of the incoming Pb ions with a precision of ~20 μm. The experiment is completed by a zero degree calorimeter inherited from NA50, which will measure the centrality of the heavy ion collisions.

The new silicon vertex spectrometer, although small in size (~20 cm long, to be compared with the ~20 m long muon spectrometer), will significantly improve the physics capability of the experiment. For each dimuon event reconstructed in the muon spectrometer, we will also reconstruct in the vertex region all the charged particles produced in the same collision in the angular window of the muon spectrometer. Using a track matching procedure, based on the comparison of angles and momenta measured before and after the absorber, we can select and identify among all the tracks the two muons that gave the trigger.

The vertex spectrometer provides a more precise measurement of the muon angles, because the tracks are measured before they enter the hadron absorber, where they suffer multiple scattering. This greatly improves the mass resolution, especially for low momentum muons and thus low mass resonances. Furthermore, if the muon reconstructed in the dimuon spectrometer comes from π or K decay, the corresponding track in the vertex spectrometer usually does not satisfy the matching criteria. This allows a direct rejection of a significant fraction of the combinatorial background. Finally, extrapolating the tracks to the interaction point, we will be able to measure the track *offset*, defined as the distance in the transverse plane between the extrapolated muon track and the interaction point.

The improvements brought by the new vertex spectrometer give the possibility to perform precise measurements, which will help to clarify some important questions left open by recent results. Firstly, thanks to the improved mass resolution and signal-to-background ratio, it is possible for the first time in heavy ion collisions to study separately the ρ and the ω. The precise study of the low mass muon pairs with good statistics and S/B, in a wide range of transverse momentum, should clarify the origin of the excess observed by the CERES experiment (see Section 1.5.3). Moreover, the offset measurement allows to distinguish prompt from decay muons. In particular, it will be possible to determine if the excess observed by NA38, Helios-3 and NA50 in the intermediate mass region (see Section 1.5.2) is due to prompt dimuons or to open charm decays.

6.2 Experimental set-up

We can distinguish two separate phases in the physics programme of NA6i: (a) the low mass dimuons and (b) the open charm physics. In principle, one could run the two programmes at the same time, but it is better to slightly optimise the set-up according to the measurement to be performed. The low mass muon pairs have a fairly large production cross-section, which does not impose special requirements in terms of beam intensity and detector efficiencies. Conversely, the open charm study, characterised by a much lower cross section, requires collecting a large number of interactions, together with good detection and reconstruction efficiency. The main differences are thus in the beam intensity, in the target thickness, and in the hadron absorber configuration. The pixel telescope remains basically unchanged, except that the low mass phase does not require redundancy in the number of pixel planes.

The muon spectrometer has been described in Section 2.2.3. The absorber configuration and the strength of the magnetic field play an important role in defining the dimuon acceptance, trigger rate and background rejection. For the low mass dimuon physics program we plan to collect data with a current of 3'000 A in the toroidal magnet and with 20 cm of iron at the end of the muon filter. For the charm production study the set-up will be optimised by increasing the current in the toroidal magnet to 4'000 A and by including 80 cm of iron in the muon filter. With this configuration the low mass dimuons are suppressed and a significant fraction of combinatorial background is rejected. This will allow increasing the beam intensity thereby improving the effective luminosity, while keeping the same trigger rate.

6.2.1 Beam and target

For the low mass muon pairs study, we will run at a beam intensity of ~10^7 ions/burst, and 4.5 mm of Pb as target (~10% λ_{int}). The target will be segmented in three sub-targets of 1.5 mm each, to reduce the contamination of events with secondary interactions. We do not need a special detector to recognise in which sub-target the interaction took place, as in the case of NA50. This is because the interaction point is determined to within ~100 μm in the beam axis as the common extrapolation of the tracks reconstructed in the pixel telescope.

In the case of the charm runs, the beam intensity will be ~5×10^7 ions/burst and the target will have a thickness of ~10% λ_{int}, resulting in the maximum interaction rate allowed by both the pixel chip and the beam-scope. At higher event rate, pile-up events would start to occur at non-negligible rates.

Before the normal data taking period, special *alignment runs* are needed to align the pixel planes among themselves and relative to the muon spectrometer. Since straight and clean tracks (low multiplicity) are required, the alignment runs are taken without field in the vertex spectrometer, and using a (secondary) proton beam.

6.2.2 The beam-scope

In order to measure the transverse coordinates of each incoming lead ion, we will insert a *beam-scope* in the beam axis, upstream of the target. This measurement will provide a strict constraint in the determination of the interaction point, inside the target, relative to which the offset of the muon tracks will be determined. The final determination of the interaction point is indeed done by tracking the (hundreds of) charged particles reconstructed in the pixel telescope. The beam-scope information provides very important constraints in the fitting procedure, improving its reliability and reducing the computing time.

The requirements imposed on this detector are very demanding in terms of radiation hardness, readout speed and spatial resolution. We need to measure the line of incidence of each incoming Pb ion, at a rate of around 10^7 ions per second, and with a spatial resolution of around 20 μm in both transverse coordinates. The beam-scope is composed by two stations of silicon microstrip detectors, installed in a vacuum tube and cooled by liquid nitrogen.

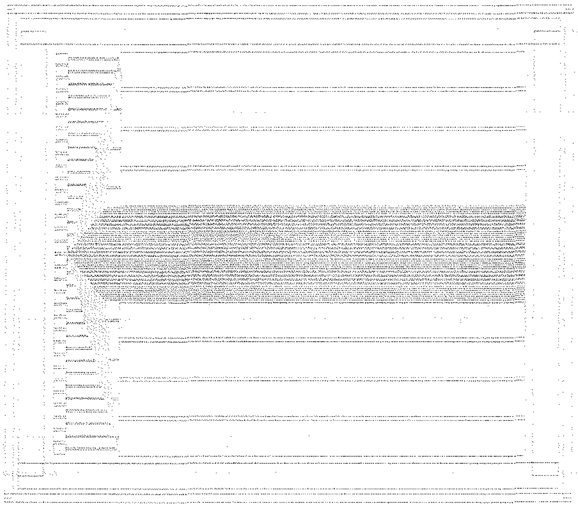

Figure 6-1: Beam-scope microstrip plane. The large strips on the side are used to align the beam.

The two stations are placed on the beam axis at 10 cm and 30 cm upstream of the target. Each station is composed by a x and a y plane of single-sided silicon microstrips. The design of one such plane is shown in Figure 6-1. Each plane has 32 strips, 10 mm long, of which the 24 in the middle have 50 μm pitch. The 4 strips on both sides of the plane have 500 μm pitch. These large strips are used to steer the beam into the centre of the detector, and are read out once per burst. Each of the 24 narrow strips is connected to a fast current amplifier, which preserves the intrinsic timing of the signal (about 5 ns full width, as measured in the November 1998 test run described in Section 7.3). The output of the amplifier goes to a (CAMAC) discriminator, whit remote threshold setting, and then to a fast digital pipeline for signal processing. The microstrip output is sampled every 1.5 ns. In the pipeline are stored the hits of the last 3 μs. The zero suppressed data are transferred via ECL bus into a memory. It takes about 100 μs to read out the 50 to 200 words of 16 bit's coming out of the beam-scope. Each data word, corresponding to one hit, contains the strip number and the time with respect to the trigger. The counting losses of the readout system will be negligible up to 5×10^7 Pb ions per 4.8 s spill.

6.2.3 The pixel vertex spectrometer

The main component of the new experimental set-up is the vertex spectrometer, made of several planes of silicon pixel detectors, placed upstream of the dimuon spectrometer currently used in the NA50 experiment. We will use the Alice1 pixel chip, developed in the framework of the ALICE experiment.

The silicon pixel telescope is placed inside an existing dipole magnet (named TC8), of overall length 55 cm and 8 cm horizontal gap. The horizontal 1.67 T field extends over a region of 25 cm along the beam axis. The first 60 cm long Al_2O_3 section of the hadron absorber starts at 26 cm from the target, still inside the magnet.

The layout of the telescope is depicted in Figure 6-2. In the layout used to simulate the physics performance presented in this thesis, we have considered 4 stations, each composed of 2 pixel planes, placed at 8, 10, 15, and 22 cm from the target. Half of them are *Y* planes, which have the rectangular pixels oriented in such a way as to measure the y coordinate with high accuracy, $\sigma_y \approx 15$ μm, and thereby achieve optimal momentum resolution. In order to reach good accuracy in the extrapolation to the vertex also in x, the planes 2 and 4 are *X* planes, while the last two are *U* and *V* planes, tilted relative to the vertical position, in the x-y plane, by an angle of around 30°. A total number of 86 chips are enough to complete the 8 planes of the pixel telescope, covering the angular acceptance of the dimuon spectrometer (between 40 and 120 mrad). Each plane introduces a thickness of 1.1% X_0 in the path of the particles it measures.

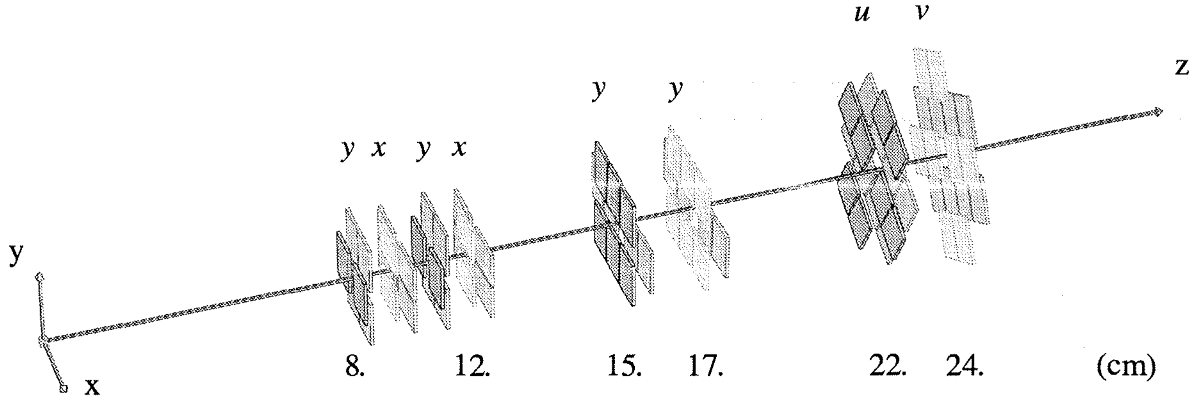

Figure 6-2: Schematic view of the vertex pixel telescope layout.

The Alice1 pixel detector

The Alice1 pixel readout chip will be manufactured in 0.25 μm CMOS technology, adopting the gate enclosed design techniques, which have been described in Section 5.3. This technology has been proven successful both in terms of component density and performance, in particular concerning the radiation tolerance, by the measurements performed on the prototype chip Alice2Test (see Section 5.5). The Alice1 chip has a total sensitive area of 12.8 × 9.6 mm^2, segmented into 256 × 32 pixels of 50 × 300 μm^2. Many of the building blocks used in the design are similar to those used in the prototype chip, but a number of changes and additional features have been introduced.

Contrary to all previous designs, the detection and the readout phases are not separated in time, requiring the implementation of a differential front-end amplifier. This approach is in fact much more suited to cope with the cross talk induced by the digital activity on the chip with respect to a single-ended front-end. The penalty incurred is an increase in the power consumption, 30 μW, more than half of the total analog power consumption. The peaking time is 25 ns and it takes less than 200 ns for the pulse to return to zero. The front-end can compensate up to ~100 nA of detector leakage current. The compensation is individual in each pixel. This feature is essential to cope with the extremely inhomogeneous irradiation present in fixed target geometry. Unlike the prototypes, only positive input charges are accepted. The input of the pre-amplifier is always connected to an injection capacitance, which can be used for calibrating and testing every cell.

The discriminator threshold can be adjusted individually thanks to a 3-bit's register stored locally in each cell. The output is connected to a synchronisation circuit, which produces a pulse with half a clock cycle duration, which goes to the delay line. A masking flip-flop allows suppression of noisy cells. The short pulse is also connected to two circuits, each of which sends a pulse to the bottom of the column. The first pulse is OR-ed with the outputs of the other columns, generating a Fast-OR signal. The second pulse is added to the pulses from the other columns and a Fast-multiplicity signal is thus generated.

The cell delay circuitry consists of two registers. A counter at the bottom of the chip counts continuously to N and then down to zero again. N is set such that 2·N is the number of clock cycles corresponding to the trigger latency time (if the required delay does not correspond to an even number of clock cycles, the strobe must be delayed by one extra cycle before being sent to the chip). The clock frequency can go up to 40 MHz Since the counter has 8 bit's, the maximum latency time is 512 clock cycles, i.e. 12.8 μs. When a pixel is hit, the short pulse at the discriminator output latches the counter value in both delay registers. This value is then compared with the counter content at each clock cycle. Each register has its own logic, which identifies the second true comparison and produces a coincidence pulse at the end of the delay line. The use of two registers allows delaying up to two hits in the same pixel during the trigger latency time. If a pixel has a hit in coincidence with the strobe, a logic one is latched in a 4-bit FIFO, so that up to four hits can be stored before being read out.

In the case of the LHC1, common power supplies provided the bias currents to all the chips on the same array. In this way it was not possible to correct the non-uniformity in the behaviour of the different chips due to the random chip-to-chip variations. In the Alice1 chip the analog biasing is implemented using DAC's (digital to analog converters) integrated on the periphery of the chip. Moreover, because the number of detector parameters has considerably increased with respect to the previous system, a powerful architecture for tests and controls based on the JTAG protocol [1] has been implemented in the Alice1 chip. The description of the JTAG specifications and its application in the Alice1 chip is beyond the scope of this thesis.

Layout requirements

The measurement of D meson production relies on the identification of muon tracks that do not point to the interaction vertex. In order to select an event sample dominated by muon pairs from semileptonic D decays, we must be able to measure the track offset with a resolution of at least 50 μm (for comparison, the $c\tau$ is 317 μm for D^+ and D^-, 124 μm for D^0 and $\overline{D}^0$).

Figure 6-3 shows how the offset resolution in both transverse coordinates depends on the distance between the first pixel plane and the target (keeping the other planes in their nominal positions). As expected, the offset resolution improves when the first plane is placed closer to the target, but even at 10 cm it would lead to a reasonable selection of $D\overline{D}$ events, using both y and x offset information.

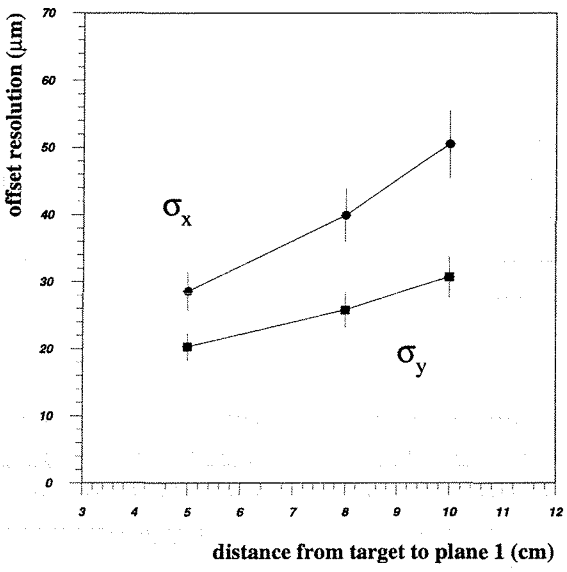

Figure 6-3: Offset resolution as a function of the distance from the target of the first pixel planes. The other planes are always kept at their nominal positions.

Figure 6-4 left shows the dependence of the occupancy (determined as the number of pixels hit over the total number of pixels in the plane) on the radial distance r from the beam axis, for three different z positions (5, 8 and 20 cm from the target). The calculation has been done using a Gaussian rapidity distribution, with $\sigma = 1.5$, and for two values of charged particle multiplicity, corresponding to average and head-on Pb-Pb collisions of 158 GeV per incident nucleon (rapidity density at mid-rapidity of 120 and 450 charged particles, respectively). The observed $1/r^2$ dependence is expected because the rapidity distribution is almost flat in the acceptance window of the detector.

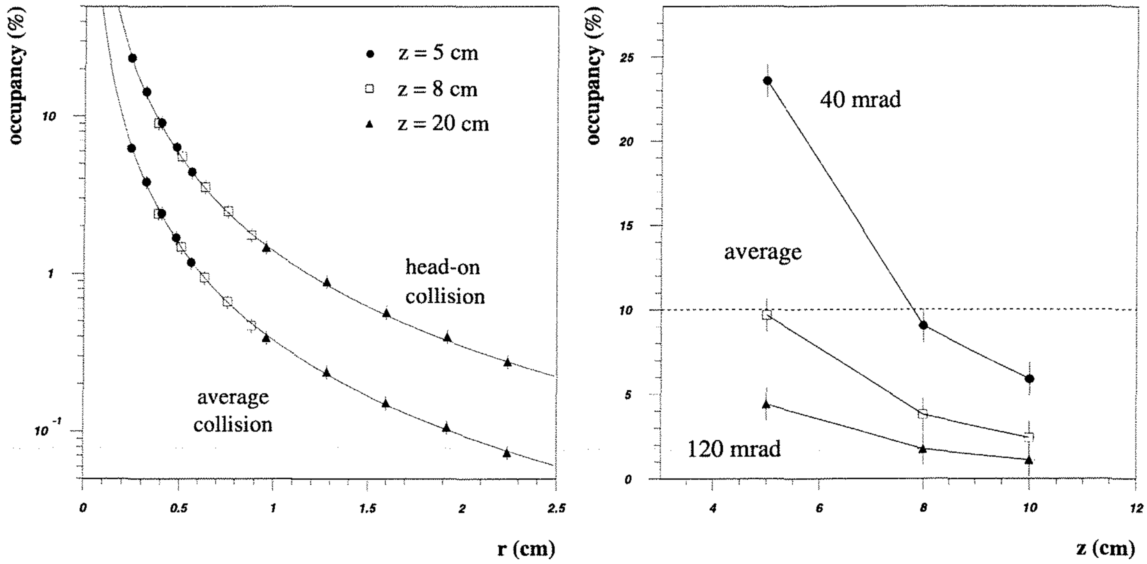

Figure 6-4: Occupancy as a function of the distance from the beam axis (left) of the distance from the target (right).

Figure 6-4 right shows the occupancy in the pixel planes for head-on Pb-Pb collisions, within the angular acceptance of the dimuon spectrometer versus the distance from the target. From these results we are confident that placing the first plane at 8 cm from the target the occupancy in the pixel planes is always below 10%, even for the most central collisions and in the area closer to the beam axis. This ensures that the track reconstruction in the vertex spectrometer can be performed with good efficiency over the full geometrical acceptance.

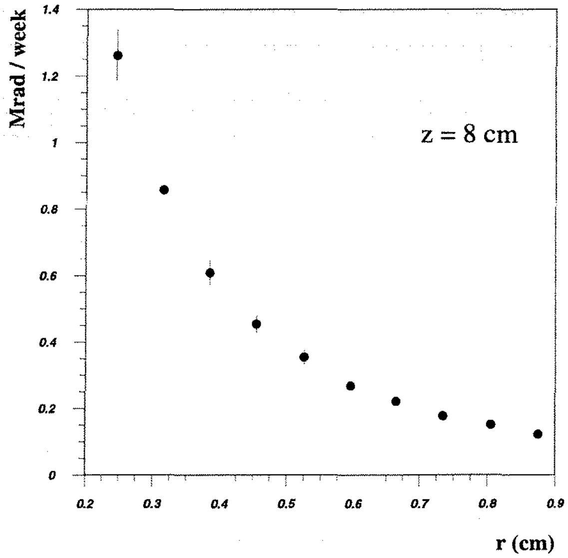

Figure 6-5: Expected radiation dose at the first pixel plane as a function of the distance from the beam axis.

In order not to have any material in the beam axis, which would result in an undesirable target, the pixel chips of the first plane are placed at a distance of 1 mm from the beam axis. This implies that the active detector area starts at 2 mm from the beam axis, limiting the geometrical acceptance for dimuon events, in the first plane, to around 80%.

We have computed the integrated radiation dose accumulated in the pixel planes, assuming the following running conditions: a beam intensity of 5×10^7 Pb ions per burst; a target thickness of 10% λ_{int}; and a running efficiency of 80%. Figure 6-5 shows the dose affecting the first plane (the most irradiated one) as a function of the radial distance from the beam axis. In the most exposed regions, which receive about 10 times more radiation than the outer areas, the radiation dose should be around 1 Mrad per running week.

The technology in which the Alice1 chip will be manufactured has already been shown to tolerate at least 30 Mrad (see Section 5.5). Furthermore, the chip will be able to cope with inhomogeneous radiation doses thanks to the individual compensation of the leakage current. For these reasons, we do not anticipate any problems from radiation damage in the readout electronics.

We have also performed a GEANT [2] simulation to estimate the background from delta rays and secondary particles produced in the magnet material. The results show that most of the delta-rays are swept away by the dipole field and do not reach the detectors, while the contribution from secondaries is negligible, increasing by less than 5% the number of hits in the last pixel plane.

6.3 Physics Performance

We have simulated the physics performance of the experiment, using the detector set-up described in the previous section. The soft particles were generated according to thermal distributions, while for hard processes we have used the PYTHIA event generator [3], using the MRS A parameterisation [4] of the parton distribution functions. The muons and hadrons are then tracked through the experimental set-up, taking into account multiple scattering and energy loss.

The event reconstruction procedure can be divided in several steps, which are summarised in the following. The first step is the reconstruction of the muon tracks in the dimuon spectrometer, which is performed using a modified version of the standard NA50 reconstruction software package, to take in account the presence of the dipole field in the vertex region.

After the clusterization of the hits in the pixel planes, the reconstruction of all the tracks in the vertex spectrometer is done taking into account the information from the beam-scope (x and y coordinates of the interaction vertex, within ~20 μm precision). This allows rejecting a large fraction of spurious tracks (random combinations of hits in the pixel planes) and to reduce the computing time needed for pattern recognition by about a factor 10.

Using the reconstructed tracks, the interaction vertex is fitted using the weighted gaussians sum method, suppressing the *outlier tracks* (tracks which do not converge to the interaction point). Already at this stage most of the muon tracks originated from π and

K decays are suppressed. In fact, many of the muons coming from hadrons which decay within the vertex spectrometer correspond to tracks not pointing to the vertex and are therefore rejected during this reconstruction step.

Among all the tracks reconstructed in the vertex telescope, the candidates to match the muons measured in the dimuon spectrometer are selected. The selection criterion is based on the comparison of the angles and momenta of the tracks as measured in the two spectrometers. A *matching* χ^2 is defined as the weighted square of the differences of the curvature (inversely proportional to the momentum) and of the slopes in the *x-z* and *y-z* planes. The tracks with minimum χ^2 are selected.

The matching procedure depends on whether we want to select prompt or charm decays muon tracks. In the case of the prompt dimuon analysis, the matching is done on the sample of tracks that point to the vertex. When looking for charm decays, the matching procedure is performed for the tracks, which have a minimum offset from the origin.

Among the candidate tracks, together with the real muons we may also have a certain number of hadrons, causing fake matches. This happens when the near by hadrons match the selection criteria as well as the real muon track. Figure 6-6 left shows the matching χ^2 distributions for correct and fake matches.

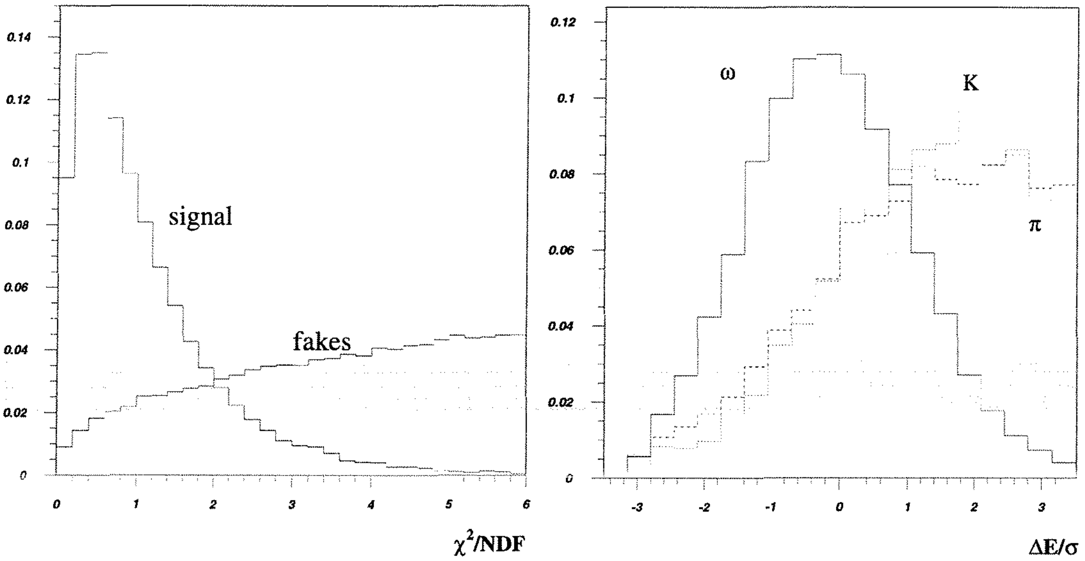

Figure 6-6: The left plot shows the matching chi2 distribution for true and fake matches. On the right, ΔE distribution for muon from ω, π and K decays.

In the next step the matching candidates are fitted again, this time with the curvature constrained to the value measured in the muon spectrometer, since its momentum resolution is better than the one of the silicon vertex telescope. This step allows rejecting some of the fake candidates and improves the precision of the offset measurement in the *y* coordinate, (leading to the values visible in Figure 6-3).

If the tracks reconstructed in the dimuon spectrometer are decay muons from π or K mesons that decayed after the pixel telescope, the vertex spectrometer measures the energy of the parent meson, which is of course always somewhat higher than the energy of the muon. Therefore, a cut on the weighted difference between the energies measured by the two spectrometers, ΔE, provides a further rejection of combinatorial background. Figure 6-6 right shows the simulated ΔE normalised distribution for muons due to ω, π and K decays.

The final mass spectrum contains a certain amount of fake matches, which are then subtracted together with the combinatorial background. The level of fakes contamination can be controlled choosing the cuts to be applied in the matching procedure and depends on the desired relative error on the signal (taking into account the dominating contribution of combinatorial background due to π and K decays).

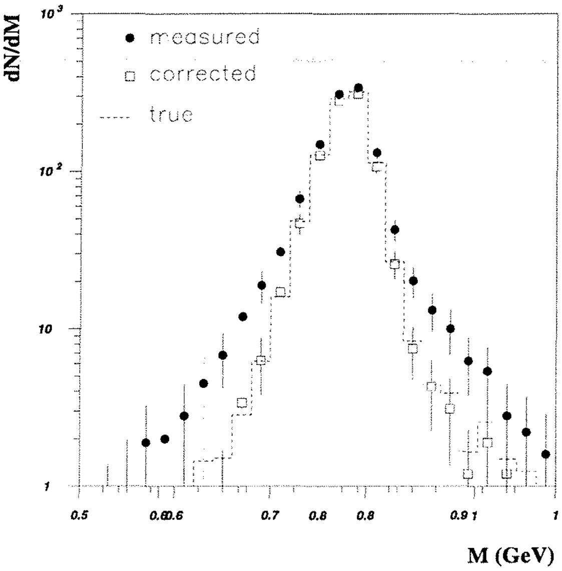

Figure 6-7: Mixed event technique demonstrated on muon pairs from ω decays.

The mixed events technique is used to subtract both the combinatorial background and the fake dimuons. The combinatorial background spectrum in the measured opposite-sign event sample is determined building a sample of opposite-sign muon pairs composed of muons from different like-sign events. In order to subtract the fake matches, we build a sample of fake dimuons by matching the tracks reconstructed in the muon spectrometer to tracks in the vertex spectrometer, which belong to a different interaction. This sample is then normalised and subtracted from the measured mass spectrum. An example of how the fakes subtraction works is shown in Figure 6-7, obtained by only generating ω mesons. Besides the event samples before and after subtraction of the fake combinations, the figure also includes the generated distribution, as a reference.

Since the low mass dilepton enhancement observed by the CERES experiment is concentrated at low p_T, we have evaluated our capability to study low p_T dimuon production. Figure 6-8 left shows the acceptances for M = 500 MeV, ω and φ dimuons, as a function of the dimuon transverse momentum. The parameters that have the biggest influence on the acceptance are the field intensity of the toroidal magnet, the field in the vertex spectrometer and the hadron absorber configuration. A nice advantage on having a dipole field in the target region is that the low p_T muons are bent into the acceptance of the muon spectrometer. This effect can be seen in the p_T distributions of accepted ω dimuons shown in Figure 6-8 right, calculated for a current of 3000 A in the toroidal magnet and including 20 cm of iron in the muon filter.

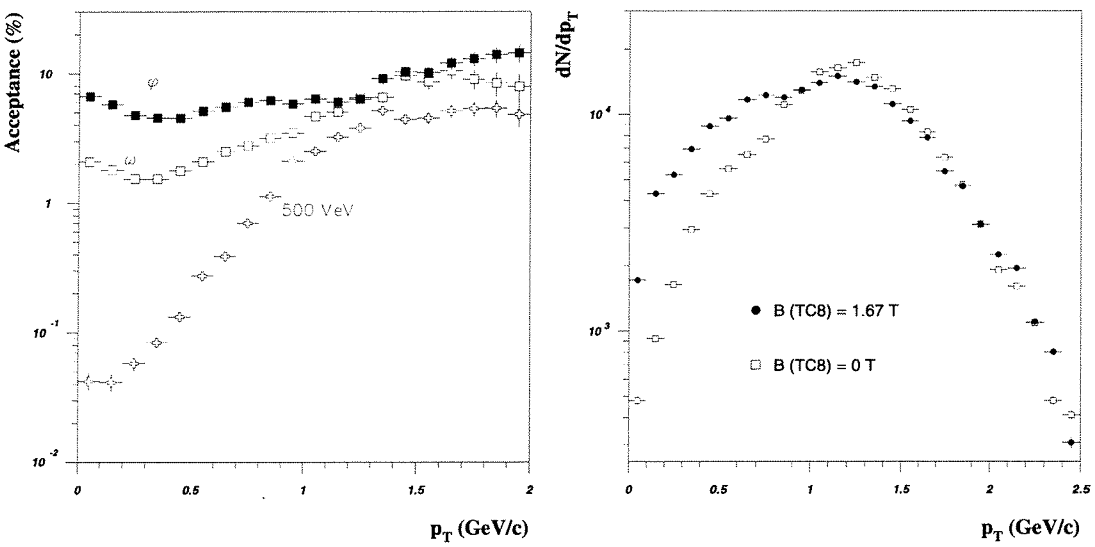

Figure 6-8: The left plot shows the acceptance as a function of the dimuon p_T. On the right, p_T distribution of accepted ω with and without field in the pixel magnet.

6.3.1 Low mass dimuon physics

In this section we discuss the results of the physics performance simulation related to the study of the low mass dimuons. In this case only the tracks pointing to the interaction vertex are selected. Since most of π and K decay muons have a significant offset from the interaction vertex, the combinatorial background rejection is more efficient than in the case of the open charm study. The reduced sample of matching candidates also results in a smaller contamination from fake matches.

Since we are looking for prompt dimuons, the pairs of matched tracks are fitted with constrained curvatures and the additional requirement of a common vertex point in the proximity of the interaction vertex, which improves the mass resolution.

Figure 6-9 shows the mass resolution for the matched dimuons, as a function of the dimuon mass. For comparison, we also show the mass resolution obtained if we only use the information provided by the muon spectrometer.

The dimuon signal mass spectrum obtained with the proposed detector layout, after subtracting the combinatorial background and fake matches, is plotted on the right side of Figure 6-10. The background distribution (including the fakes) is also shown. For comparison, the left side of this figure shows the corresponding spectra if the tracking information of the pixel spectrometer is not used. The normalisation corresponds to one week of data taking, at 10^7 ions/burst, with a target thickness of 10% λ_{int} and a beam efficiency of 75%. We can clearly see the strong improvement in terms of mass resolution and signal to background ratio.

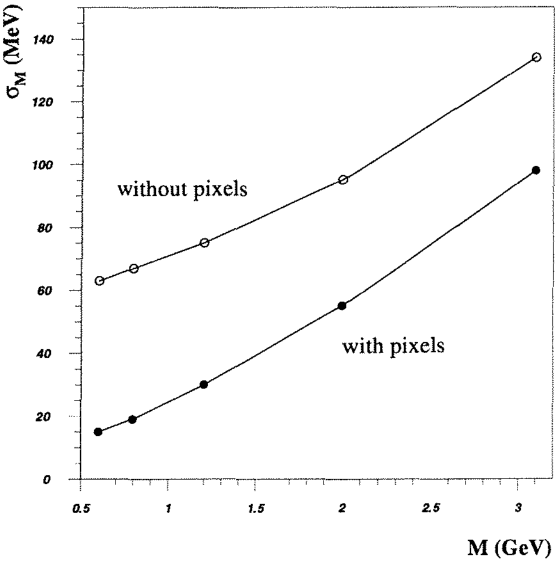

Figure 6-9: Mass resolution as a function of the dimuon mass with and without pixel vertex spectrometer.

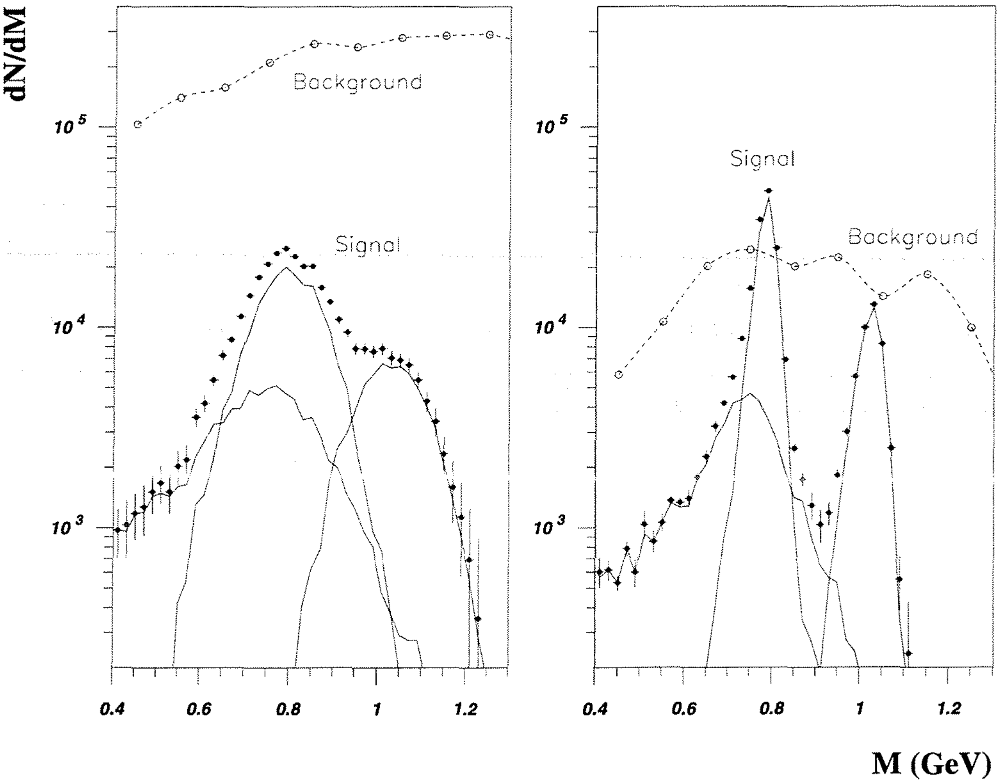

Figure 6-10: Simulated dimuon mass spectrum for NA50 (left) and NA6i (right). The number of event has been normalised to one week of data taking in the conditions described in the text.

From these results it is clear that we will be able to distinguish the ω peak from the broad ρ resonance. With the matching cuts tuned in our simulation, 65% of the dimuon events produced in average Pb-Pb collisions are reconstructed and correctly matched, while suppressing the background by a factor of 12. In these conditions we can collect at least ~200'000 ρ, ω and φ events per week, covering down to zero p_T.

The expected signal to background ratio is around 0.7 in the mass region 650–850 MeV, considering the combinatorial meson decays and the fake matches. Of course, if the Pb-Pb signal is enhanced by a factor 2-3, as suggested by the measurements of the CERES collaboration, our signal to background ratio will become correspondingly better.

6.3.2 Charm production

For the study of muon pairs from $D\overline{D}$ decays, the pattern recognition and matching procedures are slightly different from the analysis done to study low mass dimuon production. Basically, the final event sample must only contain muon pairs where both muon tracks miss the interaction vertex, by an appropriate offset.

We start by suppressing all the hits belonging to tracks pointing to the vertex and use the remaining points to fit the displaced vertex tracks. In this case, the rejection of combinatorial decay background is less efficient, since the muons from π and K decays also have significant offsets.

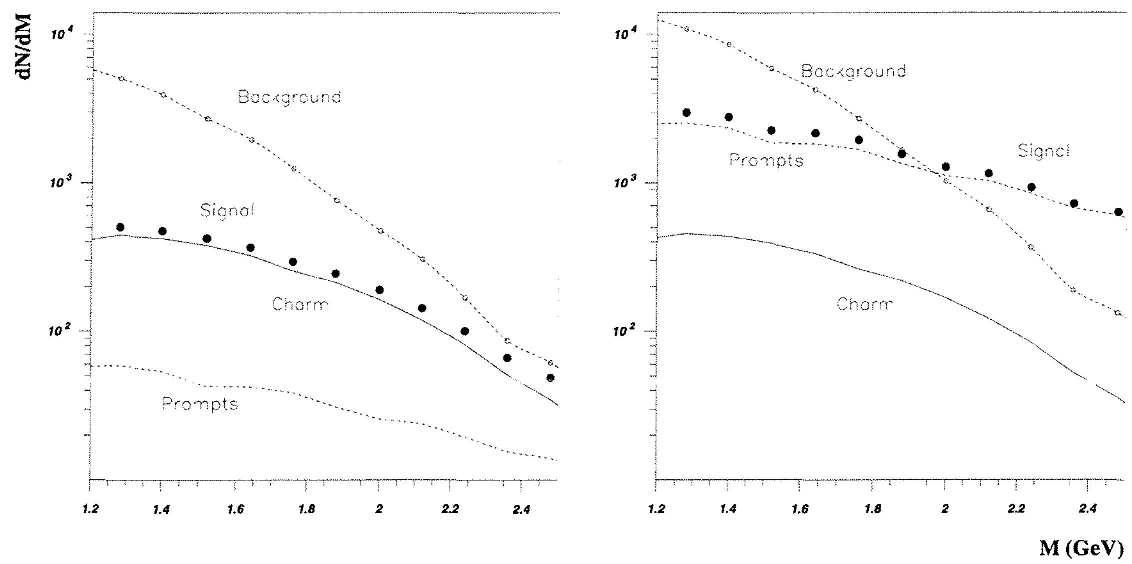

Figure 6-11: Dimuon mass spectrum for charm (left) and prompt (right) selection.

In the current analysis, we match only the tracks which have offsets between 110 and 800 μm. This cut rejects the vast majority of the prompt dimuons while retaining ~10% of the $D\overline{D}$ events.

Figure 6-11 shows the mass spectra for the open charm selection (left), with both muons in the quoted offset range, and the prompt dimuons (right), where both tracks have offsets less than 80 μm. The background spectrum, including the fake matches, is also shown.

These curves correspond to semi-central Pb-Pb collisions (around 200 charged particles per unit rapidity, at mid-rapidity). The corresponding signal to background ratio, in the mass range $1.2 < M < 2.5$ GeV, is 1:2 in the prompt event sample and 1:6 in the charm sample, for which the reconstruction and matching efficiency is around 10%.

For dimuon masses above 1.2 GeV and the open charm selection, 90% of the signal is due to muon pairs from charmed meson decays, while for the small offset selection, 90% of the signal comes from prompt dimuons. This procedure will allow us to distinguish which of these two dimuon sources is responsible for the enhanced production of intermediate mass dimuons observed by the NA38, Helios-3 and NA50 experiments.

References

[1] IEEE Standard Test Access Port and Boundary-Scan Architecture, IEEE Std 1149.1 (1990)

[2] GEANT Detector Description and Simulation tool, CERN Program Library Long Writep W5013

[3] T. Sjöstrand, Comp. Phys. Comm. 82 (1994) 74

[4] A.D. Martin, R.G. Roberts and W.J. Stirling, Phys. Rev D 51 (1995) 4756

Chapter 7

The test pixel vertex spectrometer for NA6i

We have built a test pixel vertex spectrometer aimed at verifying the new detector concept on which the NA6i experiment is based, namely the combination of a vertex and a muon spectrometer to study dimuon production in heavy-ion collisions. In particular, we wanted to check that indeed the track matching procedure, which allow us to select and identify the two muons that triggered the muon spectrometer among all the secondaries in the vertex region, is feasible also in high multiplicity Pb-Pb interactions. Another important purpose was to verify the results of the physics performance simulation.

The test pixel telescope was assembled using the available Ω3/LHC1 pixel detector, which has been described in Chapter 3. This detector already fits the requirements of the project in terms of spatial resolution, granularity and timing, but it could not stand the expected radiation load. The vertex spectrometer was tested in the NA50 experimental area with proton and Pb beams. Although these tests were done in short beam time periods, with a limited geometrical coverage, and with far from perfect reconstruction efficiency, we could still collect useful data with both beams.

In the first part of this chapter, I will describe the different steps of the construction of the test pixel spectrometer. The results of the two beam tests will be then presented, after having illustrated the corresponding running conditions.

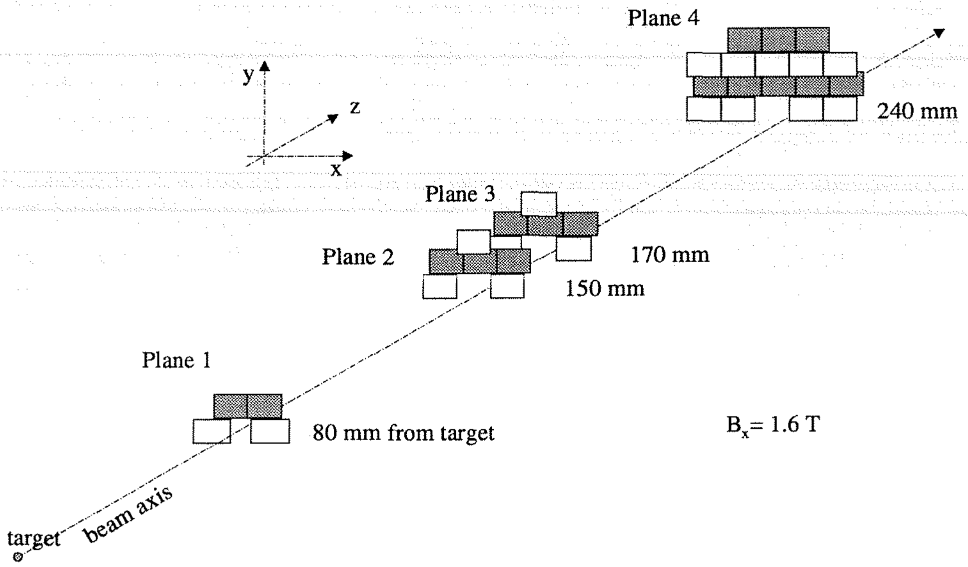

Figure 7-1: Layout of the test pixel telescope used in April 1998. Each box represents one Ω3/LHC1 pixel chip.

7.1 Assembling the test pixel telescope

The test pixel telescope we built was indeed a *half telescope*. The pixel detectors covered in fact only half of the acceptance of the muon spectrometer, corresponding to its 3 top sextants. In the following, we will describe the telescope as built for the test with proton beam. In the case of Pb beam, a few modifications were introduced, which will be discussed in Section 7.3. For the proton test, we have used a total of 33 Ω3/LHC1 pixel chips according to the layout illustrated in Figure 7-1. The pixel planes were placed inside the same dipole magnet (TC8) we intend to use in the real experiment.

7.1.1 Assembly

Prior to the construction of our test pixel spectrometer, a complete system in terms of assembly and readout had been developed for the use of the Ω3/LHC1 pixel detector in the WA97 experiment. We decided to base the test telescope on this existing system (described in Section 3.6), introducing minor modifications, which were mainly required by the different geometry of our set-up.

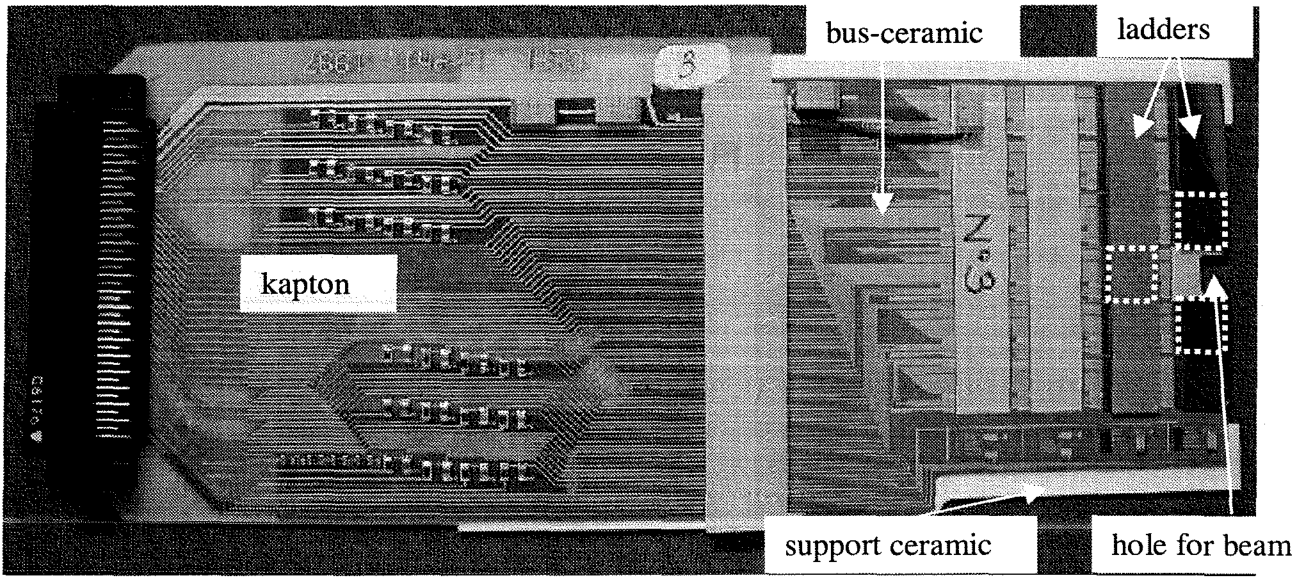

Figure 7-2: Half-plane (of plane 2) assembled for the test pixel telescope. Only the three chips marked with a box were actually connected to the readout bus.

The chips of planes from 2 to 4 were mounted on *bus-ceramics* of the type described in Section 3.6.3. Since they would not fit inside the 8 cm gap of the TC8 magnet, we had to cut out the area with the test pads (see Figure 7-2 compared to Figure 3-13). Furthermore, a half-square piece was cut out of the ceramic edges closest to the beam axis in order to avoid undesirable interactions of the beam particles in the support material. In order to prevent the creation of short circuits between the different layers of the ceramic during the cutting procedure, the design of the ceramic was changed so that the continuos ground and power layers would not be present were a cut was foreseen. Thus there was no reduction in the ceramic production yield (~90%).

The kapton cable was designed as wide as the bus ceramic and as short as possible to make it fit inside the magnet. As in the case of WA97, the kapton and the bus ceramic were mounted on a common *support-ceramic* (see Figure 7-2). This support was shaped in such a way that no extra material would be present in the acceptance window. Moreover, the support was a bit larger than the bus ceramic on the two sides. These small *wings* allowed the planes to be inserted inside the mechanical frame without damaging the much more delicate bus ceramic.

In order to cover efficiently the dimuon angular acceptance, the first plane located at 8 mm from the target could not be realised using the same assembly as for the other planes. Given the small amount of pixel chips present and therefore of bus lines, a much simpler technology could be used, based on 4-layers *printed circuit boards* (PCB). The two arrays of this plane consisted of two single-chip detectors (first array) and a 2-chip ladder (second array), mounted on a 1 mm thick PCB. The two PCB's had slightly different designs. In the case of the first array, a 2.5 mm radius hole in between the two single-chip detectors was made to let the beam pass through. The second array, was designed such that a 2-chip ladder would fit on it. The PCB thickness just underneath the chips was reduced, in both cases, to 0.3 mm, in order to decrease the amount of material seen by the particles in the acceptance, the dimuon mass resolution suffering more from the multiple scattering in the first plane of the telescope.

Pixel detectors were available as single chips or 6-chip ladders (see Section 3.6.2). Due to the limited extension of the area to be covered, we nowhere needed a full 6-chip ladder. Instead of producing sensor designs differing from WA97, we decided either to mount a full ladder and to wire bond only the chips in the acceptance window, or to cut the ladders into smaller pieces with 2, 3, 4, or 5 chips. This approach had the advantage that we could make use of ladders not used by WA97, for which the bump bonding had failed for some but not all the chips.

We investigated two different techniques for ladders cutting: by laser and by diamond saw. The laser cut was investigated at the Yerevan Physics Institute (Armenia). A ~20 μm wide laser beam was shone on the back of the sensor in between two readout chips. The laser cut was very precise and preserved the functionality of all chips. Unfortunately, since the laser was melting the silicon, the sensor leakage current of the cut pieces increased from a typical value of 1 μA to a few hundreds of microamperes. The second technique consisted in indenting the outer face of the sensor by a shallow cut using a diamond saw, and then bending the ladder in such a way that it would break starting from the previously realised cut. The cut line apparently followed the silicon lattice structure, resulting also very precise, except where the diamond saw operated. Since in this case the leakage current increased only by about a factor 10 or less, we decided to adopt the diamond saw technique.

A single readout card could read up to 24 pixel chips, which is the maximum number of chips that could be connected on one array. In our case, the number of chips per array was very small: 2 or 3 for the first 6 half planes, 8 and 9 for the last two. We therefore decided to connect chips from different arrays to the same readout card. The motherboards (see Section 3.6.3) could anyway not be connected directly to the kapton cable as done in WA97, for the lack of space inside the magnet. A 90 cm long flat cable was connected the kaptons (or the PCB's, in the case of the first plane) to the motherboards placed just outside of the magnet. The cable was made in such a way that it connected the two arrays of the same plane to a single motherboard, so that the readout card would see them as a single array. This was achieved by only modifying the readout enable lines.

It would have been possible to join on the same motherboard the first 6 arrays, i.e. 16 chips, but it was considered not convenient because all the chips of the first 3 planes would have had the same bias parameters. During the run, these parameters had to be changed, in particular to recover the problems introduced by radiation. For instance, the leakage current compensation must be increased with the dose, and as a consequence the pixel threshold and the amplifier gain must be changed accordingly. Therefore, we only connected together arrays where roughly the same dose was foreseen during the run.

The flat cable introduced an impedance mismatch, which caused small perturbations in the signals. Since only digital signals were transferred between the readout card and the pixel chips while taking data, these perturbations did not cause any problem. In the case of the tests in the lab, for which the analog test pulse was used extensively, for instance to measure and set the pixel threshold, the arrays were tested separately. The flat cable was only used when two arrays were connected together for the final check and for the common delay adjustment.

7.1.2 Detector selection and array assembling

In all the characterisation steps of the detectors, and in the preparation before their use in the experiment, the pixels are individually studied using the test input, together with the test and mask flip-flops present in each cell. The first tests are performed on individual pixel chips when they are still on the production wafers (using an automatic probe station), before they are bump bonded to the sensor. The purpose of these tests is to check the chip functionality and to measure their best operating point, given by the 5 bias currents (I_{th}, I_{bias}, I_{comp}, I_{dl}, and I_{dla}) described in Section 3.6.1.

The test, mask and delay flip-flops of all the pixels in a column are arranged as shift registers. Pre-determined patterns were written into these registers and read back to check possible digital faults. The analog circuitry was tested applying a voltage step to the input capacitance of the pixels, and looking to the response at the end of the readout chain. The distributions of the bias currents that gave the best operating point of each chip on the wafer were determined. Since all the chips of an array have in common these bias currents, it is highly preferred that they have close operating points, to ensure a homogeneous detector response and efficiency along the plane. Therefore only the chips with all bias currents within 1 standard deviation of the wafer distribution were selected to be sent for bump bonding.

The same series of tests was repeated (using again a probe station) on the detectors after they had been bump bonded, and before the mounting on the bus-ceramic. The purpose was to verify that no chip was accidentally damaged during the bonding procedure and to check the quality of the bonding itself, investigating the detector response when illuminated with a radioactive source (^{90}Sr). We repeated the tests once more after the ladder cutting. Examples of results of these tests are shown in Figure 7-3.

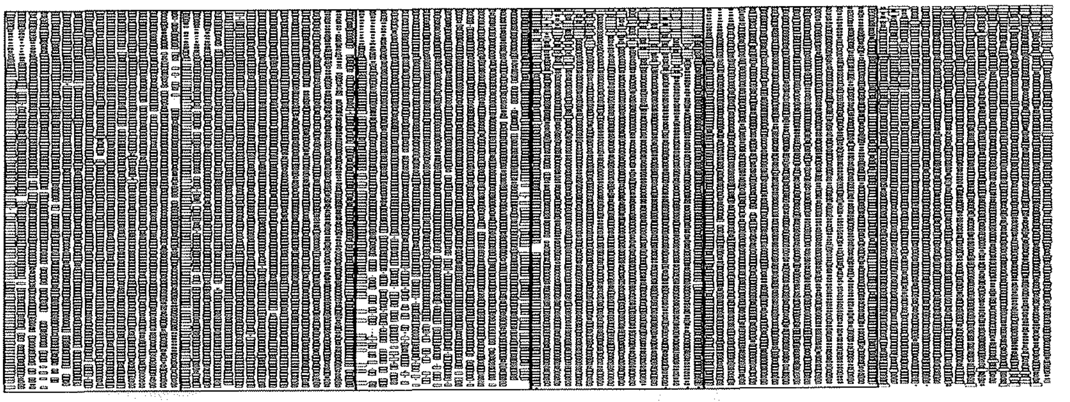

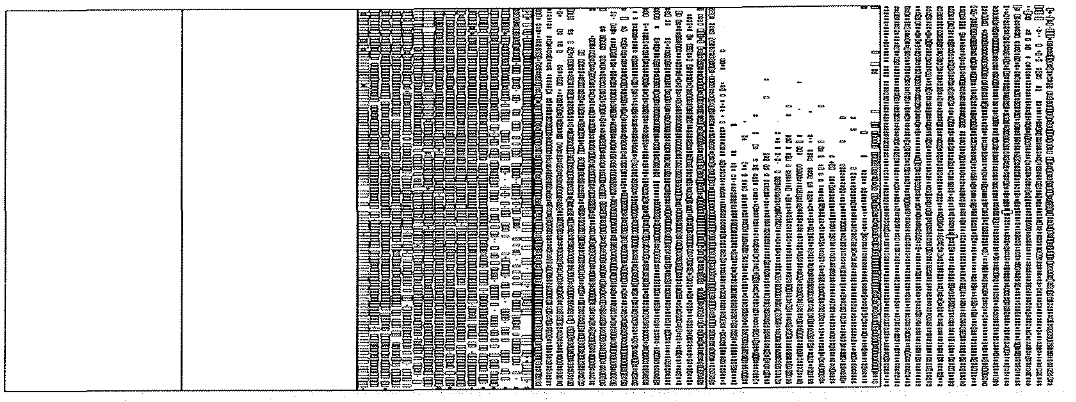

Figure 7-3: Response to a radioactive source of two ladders after bump bonding. The tests were performed on a probe station. The top ladder was selected and used by WA97. The bump bonding for the bottom detector completely failed for the first two chips. Faulty bumps are also visible in the other chips.

The assembling procedure is as follows (see Figure 7-4). First the kapton, on which the passive components and the connector have been soldered, and the bus ceramic are glued on the support ceramic. At the same time, the detector bias voltage de-coupling capacitors and a few other components are glued on the bus-ceramic (on which it is not possible to solder). Afterwards, the pixel chips are glued on the bus ceramic by conductive glue, which polymerises after a few hours at ~80°C. Finally, the wire bonding is performed, both from the pixel chips to the bus lines and from the bus/ceramic to the kapton.

In the case of a PCB, the procedure is much simpler. In fact, after the passive components and the connector have been soldered on the PCB, the pixel chips are glued on the PCB, and finally wire bonded. Normally it takes less than a day to assemble a PCB with two pixel chips, while 2 to 3 days are necessary for a ceramic-type array.

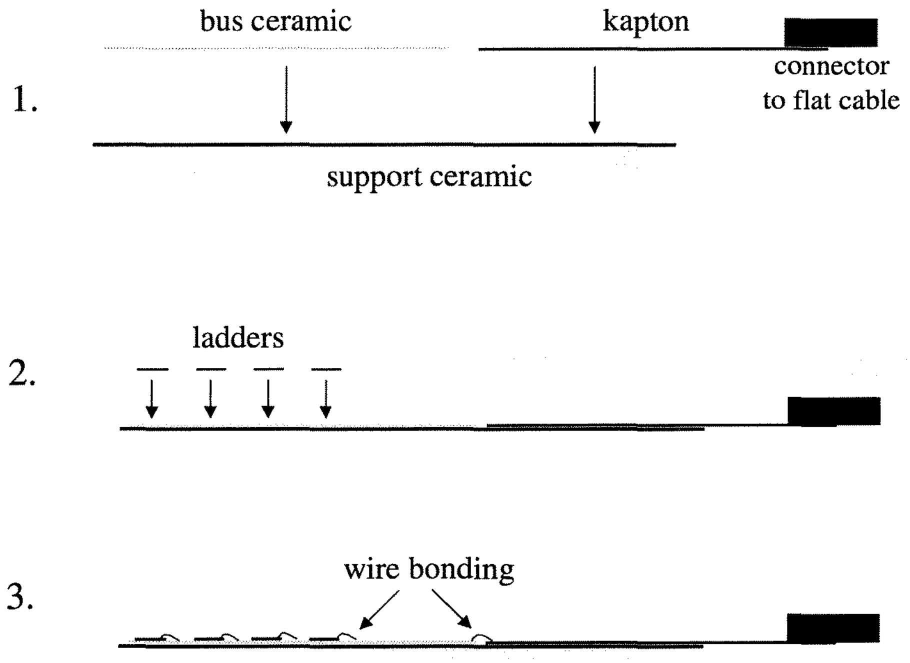

Figure 7-4: Assembling procedure.

7.1.3 Testing and setting-up of the pixel planes

Once an array was assembled, a more extensive series of measurements could be carried out in the lab. The aim was to prepare the pixel planes in such a way that they could have the best possible performance during the data taking. The first step consisted in doing again all the series of tests required to check the functionality of the chips. This time, the purpose is not only to verify that there were no accidental damages during assembling, but also to check the wire bonding connections, both from the chips to the bus-ceramic and from the bus-ceramic to the kapton. Our experience was that each array had to come back at least once to the workshop to be repaired for a problem created during the assembling.

After having checked the functionality of all the chips on the array, a scan of the bias currents I_{th}, I_{bias}, and I_{comp} was performed to find the lowest pixel threshold common to the whole array, resulting in an acceptable number of noisy pixels (~1% of the channels, randomly distributed on the array). We also tried to make the threshold as uniform as possible along the array. This was indeed a quite long step. For each setting of the bias currents, the test pulse was sent to only one row of pixels at a time, in order not to produce any perturbation in the pixel response. In view of the expected increase of the sensor leakage current due to radiation, we looked for the setting with the lowest possible value of I_{comp}, in order to have the possibility of increasing it over a wider range during data taking.

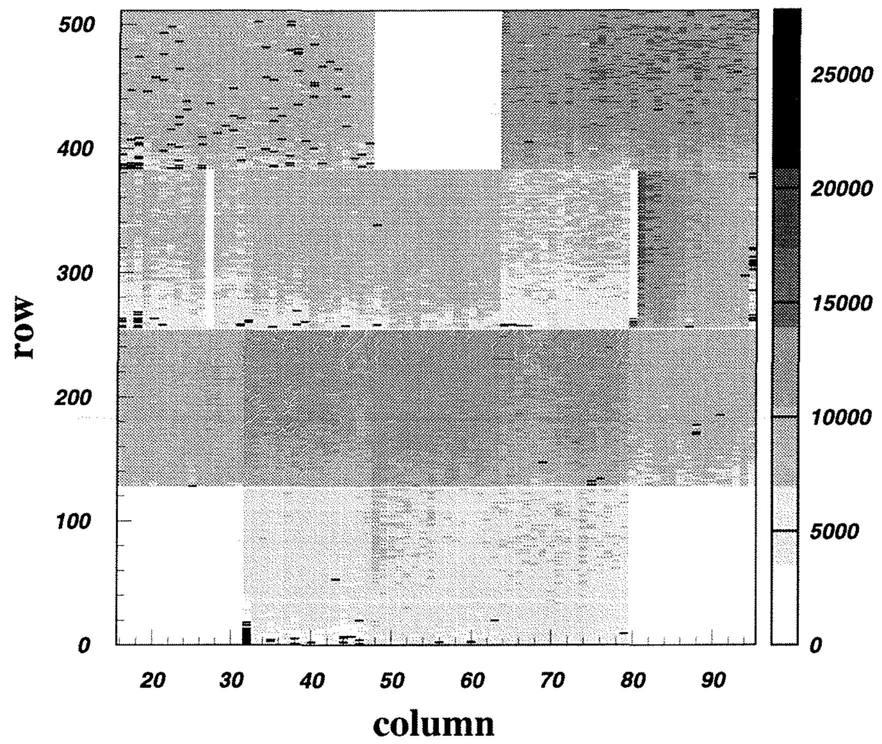

Figure 7-5: Threshold scan of plane 4 (shown up-side down with respect to Figure 7-1). No detector is present on the beam axis, nor at the two farthest corners. The histrogram is grey coded, with each box representing a pixel and the grey scale indicating its threshold in electrons. Noisy pixels were masked, and are shown in black.

Due to the limited budget available to build the test vertex spectrometer, we shared the pixel detector production with the WA97 and NA57 experiments. As a consequence, it was not always possible for us to assemble arrays with readout chips coming from the same production wafer. The result was that the pixel threshold could not be always made as uniform as wanted, especially for the arrays with many chips. This is illustrated, for example, in Figure 7-5, which shows the measured pixel threshold in electrons for the best possible setting of plane 4. The average threshold varies from ~6000 e^- (bottom ladder), to 8000÷11000 e^- (second and third ladder from top), and 13000 e^- (2 chips at the top right corner).

After having found the best possible threshold setting, the response of the detectors to a radioactive source was again verified. Figure 7-6 shows the response of plane 4 to a ^{90}Sr source after assembling. Only a small fraction of the channels of the second ladder from the top were functional after assembling, although they were good when tested on the probe station. This was most probably due to the heating up cycles needed for gluing that may have stressed bumps of poor quality, impossible to detect at prior stages. This problem was also observed in WA97, where some ladders showed problems of bump bonding after assembling which had not been seen on the probe station.

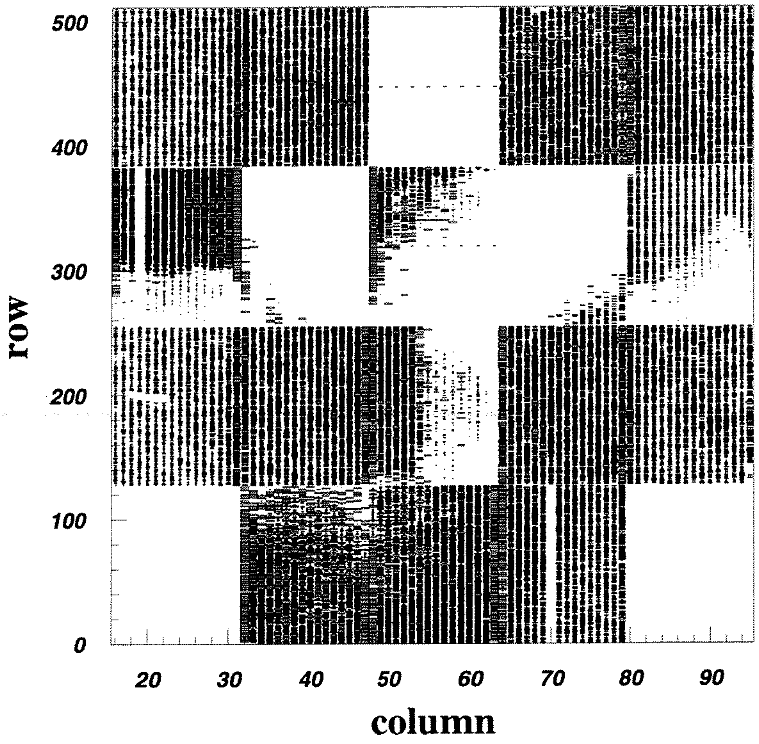

Figure 7-6: Source response of plane 4. The histogram is box coded, with each box representing a pixel. The size of the box is proportional to the number of hits recorded in that pixel.

The last step in setting-up the arrays is the adjustment of the individual pixel delay. First, the delay distribution of the response to the test pulse of all pixels was measured in the case of full added delay (the 3 bit's of the delay registers set to '111') and no added delay ('000'). As an example, the measured distributions of the second array of plane 1 are shown in Figure 7-7. In general, an efficient delay adjust can only be achieved when these two distributions overlap for a few percent of the channels. If they overlap too much, or if they are completely separated, the value of I_{dla} and therefore the amount of delay per adjust bit should be varied and the distribution measured again until this condition is fulfilled.

Once the best value of I_{dla} is found, the pixel delay distribution is recorded also for all the other possible settings of the delay registers. For each pixel, the best individual delay adjust setting was determined as the bit setting for which its response to the test pulse had its delay closest to the global array delay.

Since we had two arrays (of the same plane) connected to the same motherboard and therefore with the same bias current settings, the threshold scan and the delay adjust procedures were performed twice. The first time they were performed independently for each array, and then they were repeated for all the chips in the plane. As it happened for the pixel threshold, we could not always adjust the delay in the best possible way, due to the fact that we assembled ladders from different production wafers. Nevertheless, since we run with low beam intensities, the pile-up was acceptable also for the minimum strobe width that we could apply (~160 ns for plane 1 and ~400 ns for planes 2 to 4).

In the case of plane 1, we did not perform the delay-adjust of the two arrays at the same time. A variable resistor was installed on the PCB of both arrays, allowing us to change the value of I_{dl} for each array independently, for the same applied setting value. We first found the best delay-adjust settings for the two arrays individually and afterwards we changed the resistor value so that the two delay distributions overlapped.

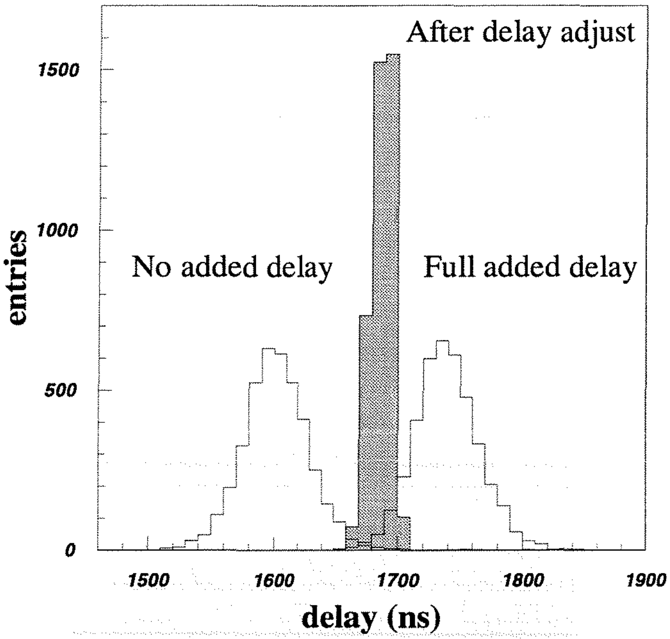

Figure 7-7: Delay scan of array 2 of plane 1. After the delay-adjust procedure all the pixel responses were contained in about 50 ns.

7.2 Test with proton beam

7.2.1 Experimental set-up and running conditions

In April 1998, we run the test vertex spectrometer equipped with 4 pixel planes (whose layout is depicted in Figure 7-1) in the 450 GeV primary CERN-SPS proton beam. The pixel planes were arranged in a mechanical frame, which was then mounted and self-aligned with a movable structure in the TC8 magnet, as shown in Figure 7-8. In order to make a fast transition from the "NA50 set-up" to the "pixel set-up", the magnet was put on a support (visible in Figure 7-9), whose feet were centred on special base points, ensuring 100 μm alignment with respect to the beam. The same support on which the pixel box was mounted, carried also the target and an anti-halo (AH) counter, which was also used as *safety system*. As soon as the AH counted above a certain alarm threshold, the beam was dumped. This system allowed us to prevent the beam from hitting the pixel detectors due to sudden problems in the beam optics.

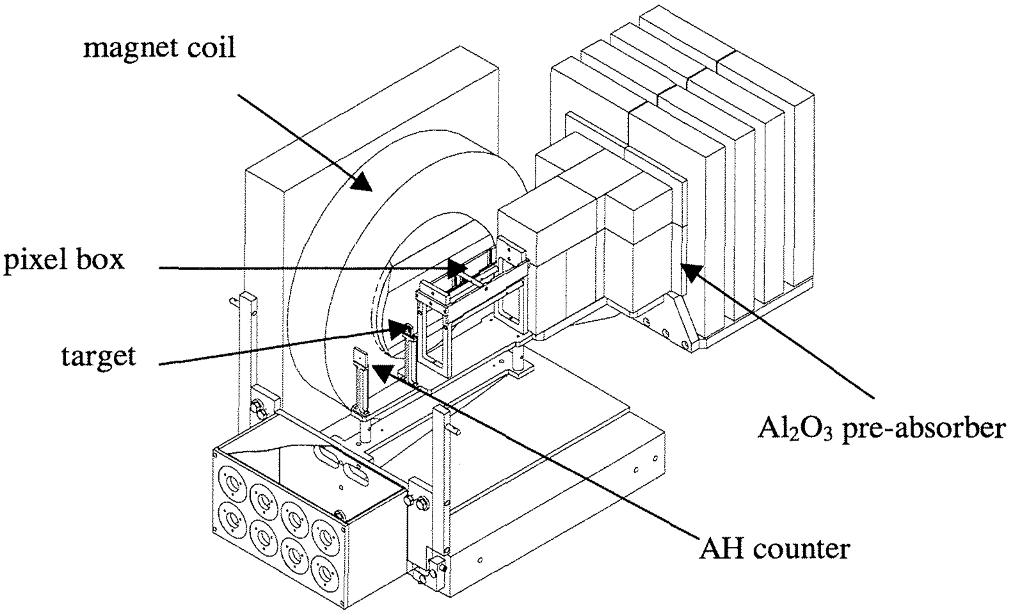

Figure 7-8: Drawing of the vertex magnet. The right coil has been cut out to show the inside.

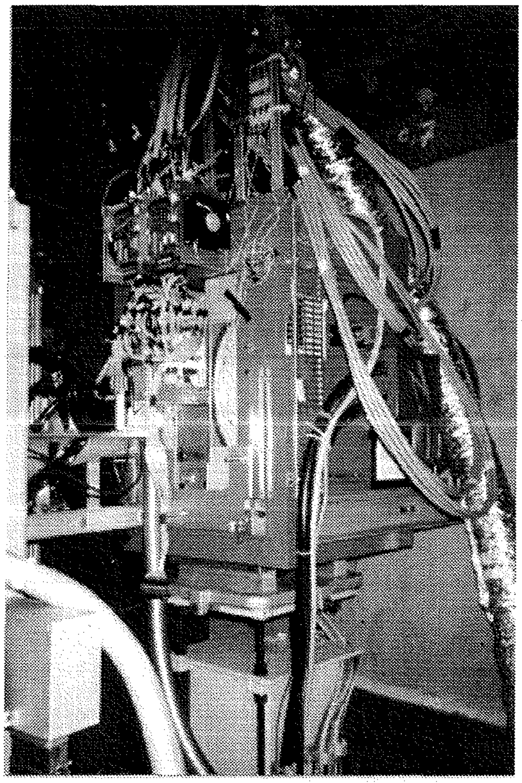

Figure 7-9: Photograph of the pixel magnet. One can see the motherboards (top-left), which are connected both to the flat cables coming from the pixel planes, and to the 40 m long cables, which depart towards the VME crate.

In order to increase the acceptance for low-mass dimuons, two changes were done in the configuration of the muon spectrometer relative to the normal running conditions of the NA50 experiment. The 80 cm of iron usually included in the muon filter were removed and the current in the toroidal magnet was decreased from 7000 A to 3000 A. Since only half of the acceptance of the spectrometer was covered by the pixel planes, corresponding to the three top sexants, the trigger scintillators in the bottom sextants were switched off.

The readout of the pixel planes was performed using a dedicated system independent of the main NA50 readout (see Figure 7-10). The pixel chips control (measurement of noisy pixels; loading of test, mask and delay registers; setting of pixel bias currents) was realised via a HP diskless processor embedded in the same VME crate where the pixel readout cards were placed. The VME processor was connected through *ethernet* to a HP workstation, which served as operative system boot server and provided the hard disk. The data were read out from the pixel cards by a VME unit, named *transputer*, normally used by NA50 experiment for the readout of the multiplicity detector. This unit was controlled by a SUN workstation, to which it was connected via a specially designed interface. The transputer was also connected to the NA50 readout system via a dedicated link.

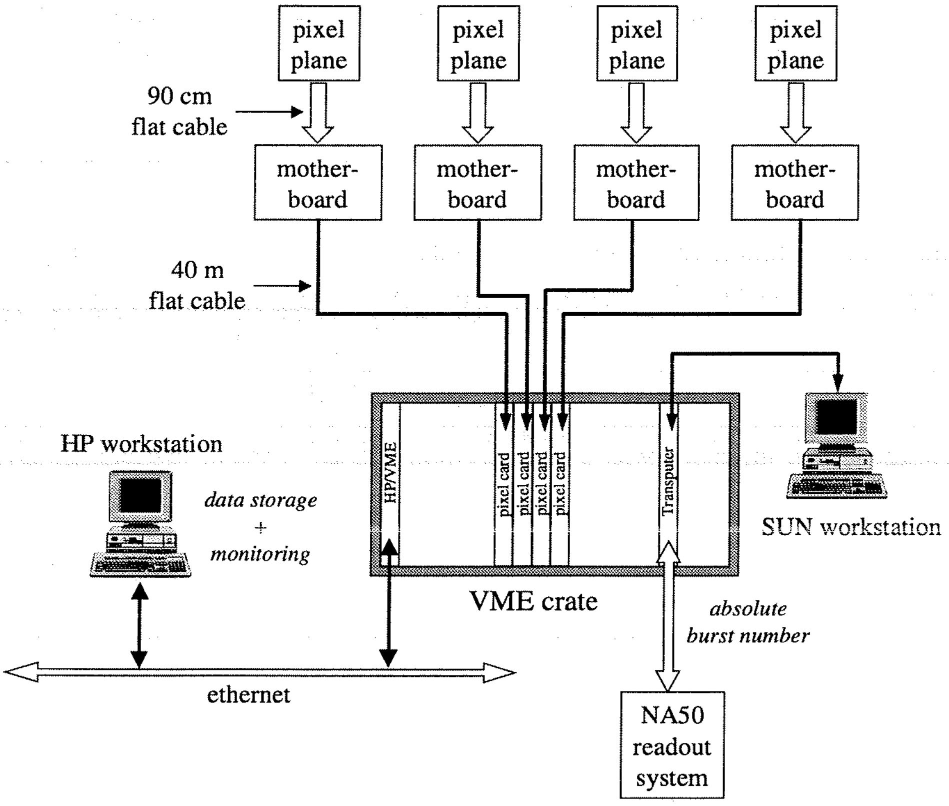

Figure 7-10: Sketch of the pixel readout and DAQ systems as for the proton test.

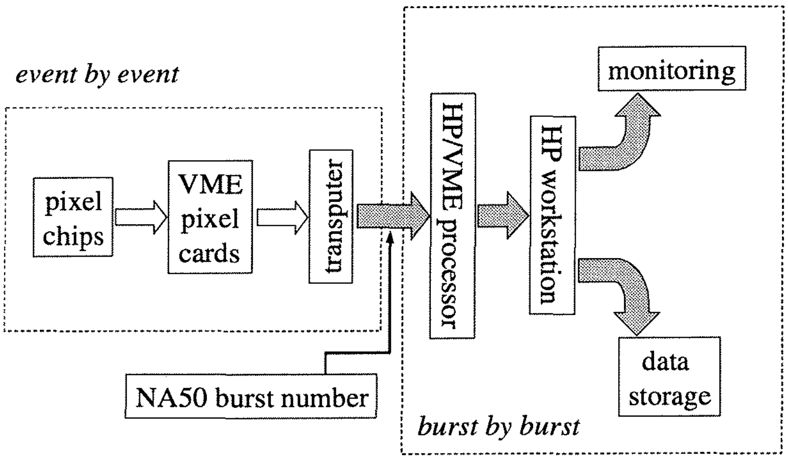

Figure 7-11: Block diagram of the pixel readout.

Figure 7-11 shows the block diagram of the pixel readout. The transputer read out the data from the pixel VME cards on an event by event basis, and stored them in its memory for the whole burst. The absolute burst number of the NA50 DAQ was added to the pixel data stream. After the end of the burst, the HP/VME processor read the data from the transputer. An asynchronous parallel process running on the HP workstation fetched the data from the HP/VME memory as soon as they were available. The data were then written on a local disk in runs of several bursts. Also, a file corresponding to a single burst was written and used by a parallel monitoring program. The readout system was limited by the transputer speed to ~300 triggers per burst.

The data from the muon spectrometer and other sub-detectors were written on a different data stream by the standard NA50 data acquisition system. The pixel data and the NA50 data were merged off-line using the absolute burst number present in both data streams. Less than 1% of the bursts had to be excluded from the data analysis because the number of triggers in those bursts was not the same in the two data files.

The average beam intensity was 5×10^7 protons per 2.5 s burst. We used a single 20 mm long, 12 mm diameter, beryllium target (about 5% of λ_{int}). This corresponded to a maximum event rate of one interaction every 500 ns. The strobe width was set to 400 ns, except for the first plane for which we set it to the minimum possible of 160 ns, to reduce pile-up hits. The trigger rate was around 10 to 50 triggers per burst. Special alignment runs have been taken with no field in the vertex magnet and a lower beam intensity (~10^7 protons per burst), in order to reduce the fraction of non-correlated hits in the pixel planes. For the alignment runs we triggered on single-muon events.

The pixel detectors were cooled by means of dry air blown from the bottom of the mechanical frame towards the planes via two ~2 cm diameter tubes. The temperature was monitored via three PT100 resistors glued directly on the back of a pixel chip of planes 1, 2 and 4. At the beginning of the run, with a power consumption of about 100 mW per pixel chip, the temperature was measured to be around 20°C. Both the power dissipation in the pixel chips and the bulk leakage current of the sensors increased during the run presumably due to radiation damage. The consequent increase in temperature, not balanced by the cooling system, induced in turn an increase of both leakage current and power consumption. Occasionally this loop generated an over-heating, named *runaway*, of the pixel chip, with the temperature reaching values as high as ~60°C. For the chips that did not have a temperature monitoring, the runaway was detected simply observing on the monitoring display a big fraction of pixels becoming suddenly noisy. Curing the problem consisted in switching off the affected chip(s) for a few minutes.

The efficiency of the pixel planes deteriorated during the run as the radiation dose increased. Since the radiation dose decreases as the inverse square of the radial distance from the beam axis, the radiation profile along the pixel planes was very inhomogeneous. In the case of the first plane, in the same pixel chip the dose differed by about a factor 10 between the chip edges. Moreover, the most irradiated zone of plane 1, which started at ~2.5 mm from the beam axis, suffered between a factor 3 to 7 more radiation than the most irradiated region of the other pixel planes.

After a few krad, the individual channel timing was lost. After ~10 krad, the chips started to suffer from the inhomogeneous irradiation. The high leakage current generated in the sensor could not be compensated over the area of each chip of plane 1. This resulted in dead regions at the edges of the chips whose shape followed the beam profile. It is worth mentioning that these results have been taken into account in the design of the Alice1 chip, where the leakage current compensation is individual per each pixel. After ~30 krad, more and more channels became inefficient.

The runaways became more frequent as the radiation dose increased and of course this was specially the case for the first pixel plane. Eventually the heat generated during the runaways deformed the thin PCB layer supporting the chips of plane 1. As a result, before the end of the run, the two pixel chips on the second array detached from the PCB, and stopped working.

7.2.2 Results

We first analysed the alignment runs. The alignment procedure consisted of the following steps: (1) internal alignment of pixel detectors, (2) alignment between the target and the pixel telescope, and (3) alignment of the pixel telescope with respect to the muon spectrometer. Since the pixel single-chip detectors and ladders are mounted with uncertified precision on the support, the internal alignment procedure was performed on each of them independently, rather than among the full arrays.

The alignment parameters were: x and y coordinates of the pixel detector (single-chip or ladder), its angle in the x-y plane, and the z coordinate of the array. Straight tracks were reconstructed in the pixel telescope allowing a large fitting χ^2. For each group of pixel detectors traversed by the same tracks, a sample of a few thousand reconstructed tracks was selected. These tracks were then fitted simultaneously trying to minimise the hit residuals in each detector, as well as the width of the residuals distribution. Minimisation was achieved varying the above mentioned parameters. The average precision of the final internal alignment was of the order of 1 to 5 μm in y (smaller pixel size) and 10 to 20 μm in x (larger pixel size).

The target centre was taken as the zero of the coordinate system. In order to obtain the relative alignment between the pixel telescope and the target, the whole telescope was translated along the three axis in such a way that the distribution of the track extrapolation to the interaction point was centred at zero. This is equivalent to require that the average track offset is zero. The alignment relative to the muon spectrometer was achieved varying the pixel detector angles in order to minimise the difference among the track angles as measured in the vertex and muon spectrometer.

The first step in the analysis of the dimuon data consisted in processing the muon spectrometer raw data. The muon tracks in the spectrometer chambers were reconstructed using a modified version of the standard NA50 software package, which takes into account the dipole field at the vertex and the different absorber configuration. Tracks passing through the iron of the magnet coils or not pointing to the target were rejected.

The pixel raw data were then processed and the final data files produced. In these files, the hit information in the pixel planes was only associated to events for which two muons were reconstructed in the dimuon spectrometer. All tracks in the vertex telescope were reconstructed, fitting the hits in the x coordinate by a straight line and the hits in the y coordinate by a parabola. Quality cuts were applied to reject tracks with large fitting χ^2 and/or large offset.

The following step was to search for the best candidates, among all the tracks reconstructed in the pixel spectrometer, to match the two tracks reconstructed in the muon spectrometer. It is worth reminding that the matching was based on the comparison of the angles ϕ_x and ϕ_y (slope in x and y respectively), and the curvature C of the tracks as measured in the vertex and muon spectrometers. Each candidate was thus associated to a matching χ^2_{match}, defined as the sum of weighted quadratic differences of these 3 track parameters. The best candidates were selected independently for the two muons as the tracks with the minimum χ^2_{match}. Finally, the best candidate tracks were fitted again in the pixel spectrometer, this time imposing a common vertex and constraining the momenta to the values measured in the muon spectrometer, which are more precise by a factor 2-3 than those measured by the vertex spectrometer.

The low detector efficiency due to radiation damage and to bump bonding problems resulted in the fact that most of the tracks in the vertex region had only three points along their trajectory, and a large fraction of them were lacking either the first or the last point. For those tracks, the momentum resolution was lower, corresponding to a lower matching efficiency.

Another problem that we encountered was the fact that many of the collected triggers were due to interactions that did not take place in the target. Short special runs without target were taken to study this problem. It was found that ~70% of the triggers were out-of-target interactions. A large fraction of the triggers had at least one muon coming from an interaction in the beam dump. This was due to the fact that we had a lighter absorber configuration with respect to the NA50 running conditions, where this problem is not so relevant. The shorter absorber was not able to fully contain the showers generated by interactions in the beam dump. Even if the average momentum of the muons generated at the end of the absorber was rather low, they were not swept out by the low magnetic field used in the muon spectrometer. Furthermore, since there were many hits in the first trigger hodoscope, the trigger logic could find a track pointing to the vertex, even if the real muon was actually coming from the beam dump.

From a sample of about 30'000 events with a muon pair reconstructed in the muon spectrometer, ~9000 corresponded to an event with an interaction in the target. Due to the low detector efficiency, only ~600 opposite-sign dimuon events were correctly reconstructed and matched. Figure 7-12 shows the corresponding mass spectrum before (left) and after (right) using the pixel spectrometer information to fit the tracks. The data points are compared to the superposition of two gaussians, representing the ω and ϕ resonances, and a Breit-Wigner, representing the ρ, with relative normalisation imposed from previous measurements (equal cross sections for the ρ and ω mesons and 20 times less ϕ's). Comparing the two figures, we clearly see a substantial improvement in mass resolution: the curves on the left have $\sigma(\omega)$=70 MeV and $\sigma(\phi)$=75 MeV while those on the right have $\sigma(\omega)$=23 MeV and $\sigma(\phi)$=26 MeV. These values are in good agreement with the expectations from the simulation.

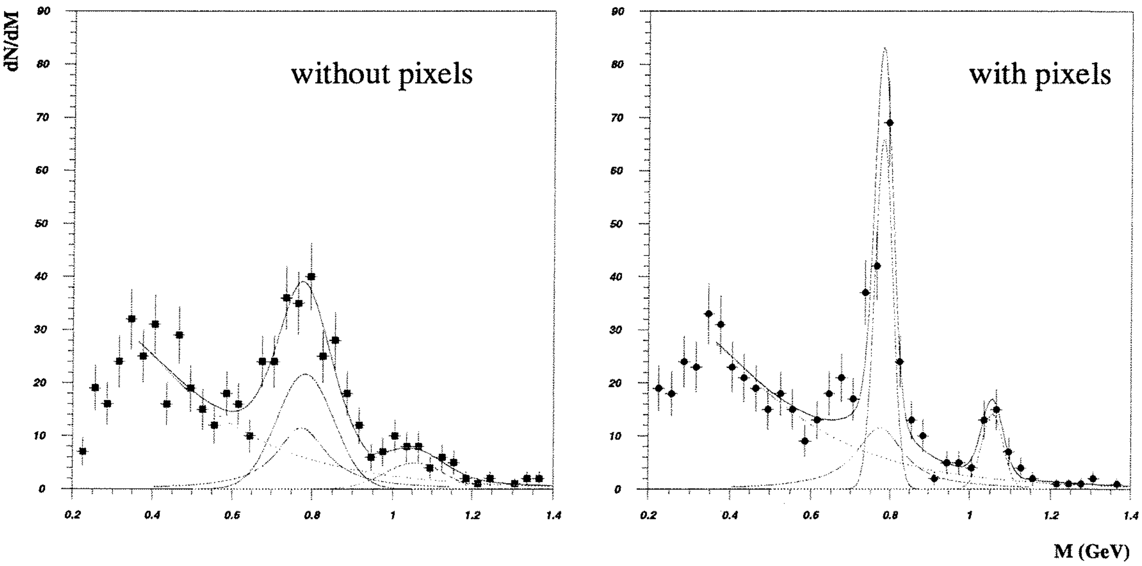

Figure 7-12: Results from the p-Be test. The improvement in mass resolution provided by the pixel vertex spectrometer can be clearly seen.

7.3 Test with lead beam

7.3.1 Experimental set-up

In November 1998 we had a 3-day test run, during which the CERN-SPS 158 A GeV Pb beam was sent on a segmented Pb target (three 1.5 mm thick sub-targets spaced by 12 mm). The average beam intensity was $\sim 5\times10^6$ Pb ions per burst of 4.5 s. The hadron absorber included 20 cm of Fe, while the vertex magnet was upgraded in order to run at 1.7 T. We used the same absorber configuration and magnet current that were used for the proton run. A new *interaction counter* (IC) was installed just after the target. This was a 3×3 cm^2 scintillator counter with a 7 mm diameter hole in the middle to let the beam pass through. It was used in the offline analysis to reject events were there was no interaction in the target. We also made use of the ZDC.

For the alignment, we used low multiplicity Pb-Pb events, but we also collected special runs using a secondary proton beam. Since this beam could not be focused as much as the primary beam, we replaced the 3 sub-targets by a large block (~10×10 cm^2) of Al_2O_3.

The pixel telescope layout was also upgraded from the 33 chips used for the proton test to 54 chips. In particular, we added more planes in order to introduce some redundancy, which would help in covering at least partly the inefficient detector areas. We replaced the first plane, which got destroyed by radiation in the previous test, and added an identical plane at 10 cm from the target. The plane 4 of the April test was moved to 22 cm from the target (now called plane 4') and in its previous place a new plane was installed. This is shown in Figure 7-13. Accidentally one of the 40 m long cables that connected a motherboard to the VME readout cards in the counting room broke just at the beginning of the run. This forced us to disconnect one plane, and we choosed the less efficient one, which was the plane 4'.

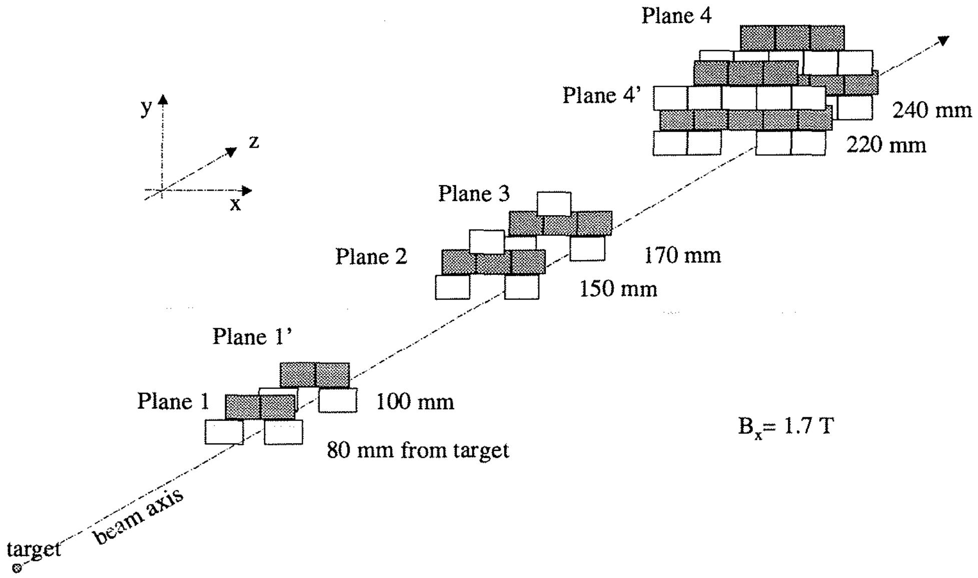

Figure 7-13: Layout of the test pixel telescope as for the Pb beam test.

The mechanical frame which holds the pixel planes was also modified to introduce a more efficient cooling. Contrary to the case of the proton test, the frame was closed on the bottom and on the top, except for apertures open in correspondence of the pixel planes. Dry and clean air coming via a ~5 cm diameter pipe connected to the base of the box was blown through the apertures. The air flow was forced to pass close to the detectors. We verified that the flow was enough to completely remove the heat coming from the TC8 magnet. On the other side, the number of chips, and therefore the power consumption, increased with respect to the previous test. The new cooling system allowed us to keep under control the number of chip runaways, but it was not enough to completely remove the problem.

The readout and DAQ systems developed for the proton run were not able to cope with the expected data volume of ~10 kbyte per event, and the required trigger rate of ~2000 triggers per burst. The transputer card was used only to get the absolute burst number (relevant for the off-line data merging), while the HP/VME processor was kept for the setting up of the pixel cards and the measurement of noisy channels. The readout of the pixel data was performed by a new fast RIO2/VME processor. In order to exploit better the processor speed, the pixel readout cards were modified by introducing the possibility of using the VME *block transfer mode*. The new readout system was able to acquire up to 5000 triggers per burst.

The pixel data were read out on an event by event basis. In principle, it could have been possible to use the block transfer mode to acquire the data burst by burst from the pixel card during the inter-burst period. Unfortunately, the memory present on the pixel card was not sufficient to store the data corresponding to an entire burst, and inserting a new larger memory would have required the design and production of new readout units.

The data storage and monitoring was performed again by the HP workstation. While we encountered no problem with the data transfer (via ethernet) and recording at the end of each burst, the monitoring program was far too slow to process the pixel information. Due to the absence of a real slow control system and to the slow monitoring, we could not react rapidly to switch off pixel planes when a runaway occurred. As a result, during the run the motherboard of plane 3 had a severe damage and was not functional anymore.

7.3.2 Results

Apart from the hardware problems mentioned in the previous section, which forced us to collect data with a reduced detector coverage, the overall efficiency of the pixel planes decreased during the run because of the accumulated dose that summed up to the one already received in the previous test.

Out of the ~200'000 events with opposite-sign muon pairs reconstructed in the muon spectrometer and originated by an interaction in the target, only around 4000 could be reconstructed and matched. The resulting mass spectrum after the subtraction of the (dominating) combinatorial background has no significance because of the lack of statistics. Nevertheless, we were able to achieve positive results on single muon track matching, which make us confident about the feasibility of our new detector concept.

We used the correlation between the interaction counter (IC) and the ZDC to reject events coming from interactions upstream of the target, corresponding to the smaller area at the bottom of Figure 7-14 left.

The alignment procedure and the track reconstruction in the muon spectrometer were the same as performed for the test with protons. The pattern recognition in the pixel spectrometer was improved in order to work in a reliable way also in the case of high multiplicity events. Due to the high occupancy, it could happen that the track finding algorithm found more than one track sharing the same hit in a pixel plane. From this sample of tracks, only the three with the best fitting χ^2 were selected as candidates for the matching.

The matching procedure was also very similar to the one described for the proton data. The only difference was that in the case of Pb-Pb events a more strict constraint on the dimuon vertex could be set. In fact, the interaction point was now determined with higher accuracy because we could use the dozens of tracks reconstructed in the vertex spectrometer.

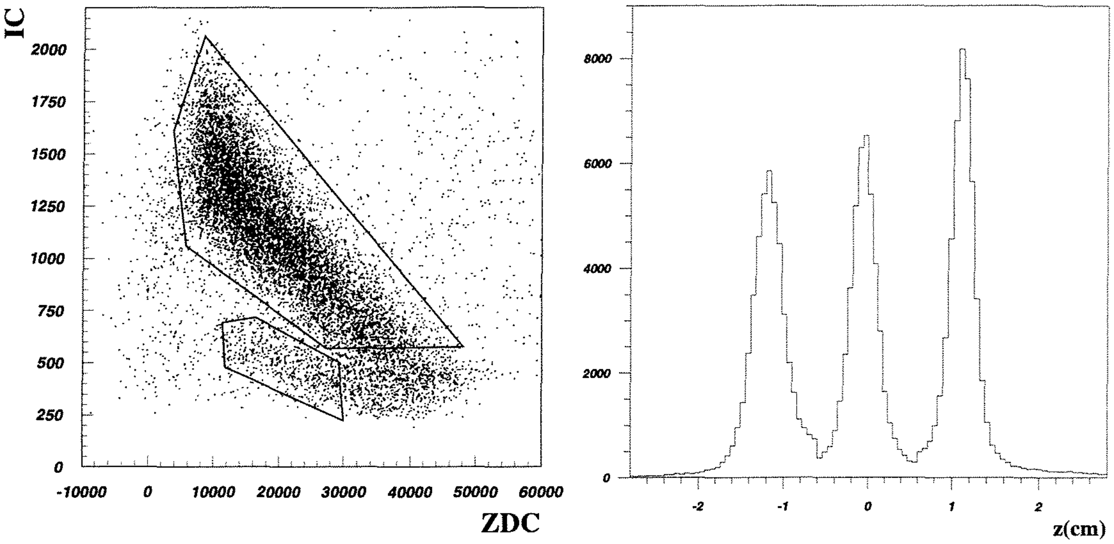

Figure 7-14: Left: correlation between the interaction counter IC and the ZDC. The large zone contains events with an interaction in the target. The small area contains interactions upstream of the target. Right: vertex distribution obtained extrapolating the tracks reconstructed in the pixel vertex spectrometer. The three sub-targets, nominally positioned at –1.2, 0, and +1.2 cm, are clearly identified.

Figure 7-14 right shows the vertex distribution reconstructed using the tracks in the pixel telescope. The three sub-targets are clearly distinguishable. We have simulated the expected performance of the test spectrometer, in terms of single muon track matching, taking into account the measured detector efficiencies. A comparison between the simulated (left plots) and the measured data (right plots) can be seen in Figure 7-15. The top row shows the difference between the slope in the y-z plane for the tracks measured in the vertex telescope and in the muon spectrometer. Similar results were obtained for the x-z plane. The middle plots illustrate the quality of the matching in terms of the track curvature.

The bottom plots compare the matching χ^2_{match} obtained in the simulated and in the measured data. Not only the shape of the distribution does not reveal any pathology in the matching procedure, but also the number of matched muons in the data is in agreement with the simulation results.

These results clearly indicate that the detector concept continues to be valid even in the rather demanding conditions of high multiplicity Pb-Pb collisions. In particular, we are now confident that the track matching procedure will work up to the most central Pb-Pb collisions, with efficiencies that can be realistically estimated by simulation.

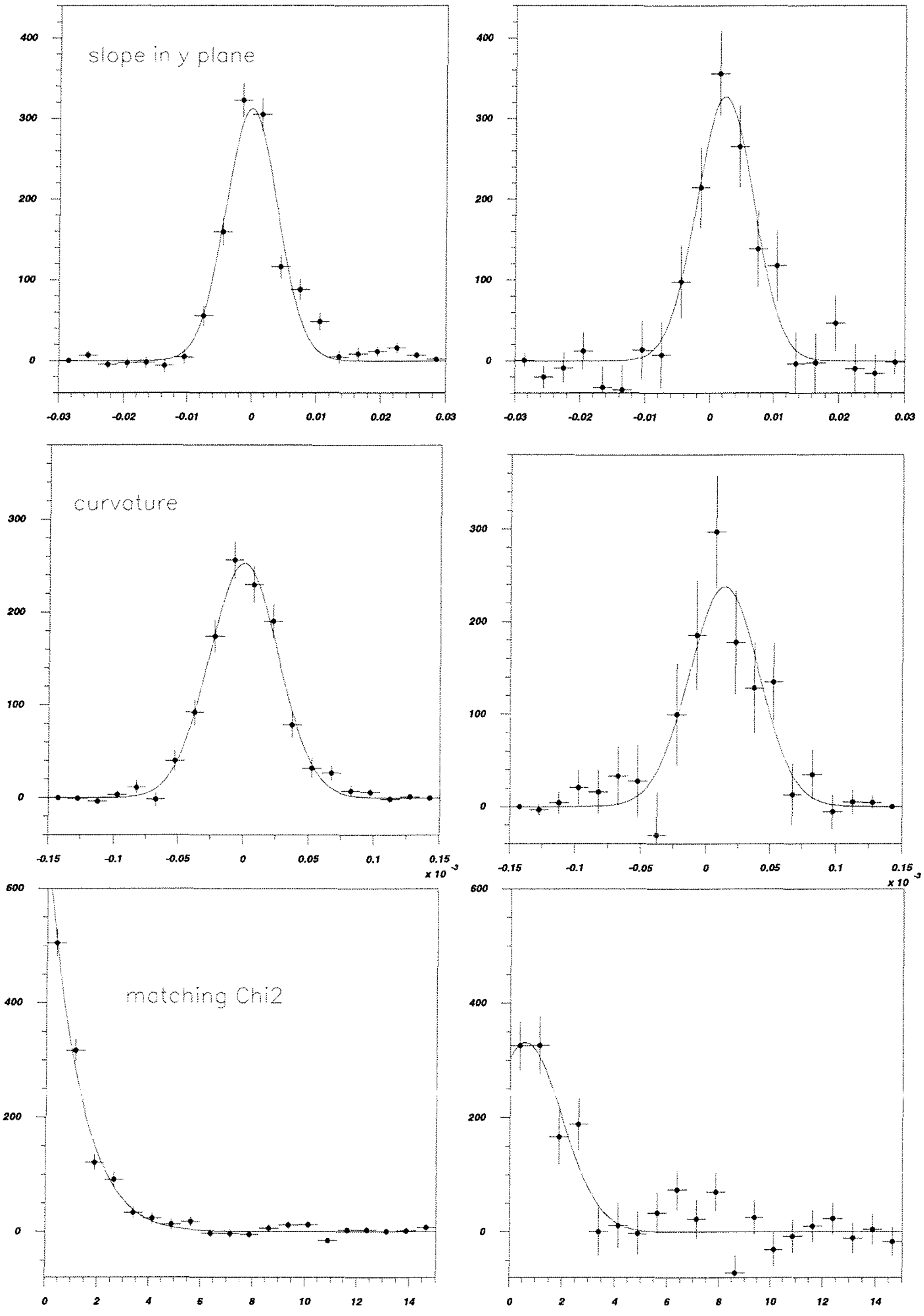

Figure 7-15: Comparison between the simulated (left) and measured (right) single muon matching parameters. The simulation takes into account the measured detector efficiencies.

We also tested a first version of the beam-scope detector. Four microstrip planes were installed inside a cryostat, which was placed in the NA50 Pb beam line. The operating temperature was ~130 K. The detector configuration and readout were the ones described in Section 6.2.2. We were able to detect and identify each incoming Pb ion even at the nominal intensity of ~5×10^7 ions/burst. Earlier, we had exposed to Pb beam a silicon pad detector (3×3 matrix, pad size 1.5×1.5 mm^2), cooled to ~80 K. The beam was centred on one of the pad. No degradation of the detector performance was observed after ~1 Grad. These preliminary results demonstrate that the beam-scope detector works as expected, while more data are needed to evaluate the ultimate radiation resistance.

Conclusions

We can summarize the results of this work as follows.

After the discovery of the *Lazarus effect*, we have carried out a systematic study on the performance of heavily irradiated silicon detectors operated at cryogenic temperatures. We have shown that the charge collection efficiency and position resolution of silicon detectors irradiated to fluences $> 10^{14}$ n/cm^2, and no longer functional at room temperature, are recovered if the operating temperature is below 130 K. These results open the way to the development of new tools for high-energy physics experiment (as for example a new Pb beam tagging detector).

We have shown that devices manufactured in commercial 0.25 μm CMOS technology and designed using a special transistor layout (enclosed geometry) are radiation hard up to very high doses (30 Mrad, $\sim 10^{15}$ mip/cm^2). This result was obtained on pixel prototype chips irradiated both by protons and X-rays.

Thanks to these developments, one can now envisage to upgrade the NA50 dimuon spectrometer, inserting a pixel vertex spectrometer in the target region, which can withstand the expected radiation dose. The pixel telescope will be based on the forthcoming Alice1 pixel chip, manufactured in 0.25 μm CMOS technology, and designed in enclosed transistor layout. While having been developed for the ALICE experiment, it has been found to be ideally suited for the special needs of our experiment.

We have evaluated by simulation that such an experiment would be able to collect in a few weeks of beam enough statistics to perform a precise measurement of low-mass dimuon production. In particular, with 20 MeV mass resolution at the mass of the ω, we would be able to separately study the production of ω and ρ mesons. The pointing accuracy of the vertex telescope would also allow to measure the offset of each muon track, at the interaction point, with a resolution better than 50 μm. This is good enough to select an event sample highly enriched by simultaneous semi-leptonic decays of charmed mesons. Thus we would also be able to clarify whether the excess production of dimuons with mass between 1.2 and 2.5 GeV, measured by the NA38, Helios-3 and NA50 experiments, is due to prompt dimuons (e.g. thermal dimuons) or to muon pairs due to charm decays.

The feasibility of this new detector concept in dimuon spectrometry has been demonstrated by the results obtained with a test pixel spectrometer. The two muons, which are measured and identified as such in the muon spectrometer, are recognized even among the many hundreds of particles produced in a head-on Pb-Pb collision, by track matching, i.e. comparing angles and momenta measured in the two spectrometers. The expected mass resolution of 20 MeV at the mass of the ω, has been confirmed with data collected in p-Be collisions.

And you can dream
So dream out loud
You know that your time is coming 'round
So don't let the bastards grind you down

Paul Hewson